AD_____

Award Number: W81XWH-07-1-0662

TITLE: Orthopaedic Implant Design and Manufacturing for Traumatic Injuries

PRINCIPAL INVESTIGATOR: Diane Wagner, Ph.D.

CONTRACTING ORGANIZATION: University of Notre Dame
Notre Dame, IN 45555

REPORT DATE: March 2012

TYPE OF REPORT: Final

PREPARED FOR: U.S. Army Medical Research and Materiel Command
Fort Detrick, Maryland 21702-5012

REPORT DOCUMENTATION PAGE

Form Approved
OMB No. 0704-0188

1. REPORT DATE *(DD-MM-YYYY)*	**2. REPORT TYPE**	**3. DATES COVERED** *(From - To)*
		1 SEP 2007 - 29 Feb 2012

4. TITLE AND SUBTITLE
Orthopaedic Implant Design and Manufacturing for Traumatic Injuries

5a. CONTRACT NUMBER

5b. GRANT NUMBER
W81XWH-07-1-0662

5c. PROGRAM ELEMENT NUMBER

6. AUTHOR(S)
Diane Wagner, Ph.D.

E-Mail: dwagner@nd.edu

5d. PROJECT NUMBER

5e. TASK NUMBER

5f. WORK UNIT NUMBER

7. PERFORMING ORGANIZATION NAME(S) AND ADDRESS(ES)
University of Notre Dame
Notre Dame, IN 45555

8. PERFORMING ORGANIZATION REPORT NUMBER

9. SPONSORING / MONITORING AGENCY NAME(S) AND ADDRESS(ES)
U.S. Army Medical Research and Materiel Command
Fort Detrick, Maryland 21702-5012

10. SPONSOR/MONITOR'S ACRONYM(S)

11. SPONSOR/MONITOR'S REPORT NUMBER(S)

12. DISTRIBUTION / AVAILABILITY STATEMENT
Approved for Public Release; Distribution Unlimited

13. SUPPLEMENTARY NOTES

14. ABSTRACT

The overall objective of this project wis to develop a three-dimensional woven material that provides a new surface for damaged areas of localized cartilage defects. We show that welded-woven materials have dramatically improved wear resistance and that their mechanical properties are more similar to cartilage than their unwelded counterparts. Additionally, we began experiments with short-duration, nontoxic crosslinking protocols that will improve the wear resistance of cartilage. If further studies are successful, they may lead to techniques that reduce cartilage wear against engineering materials, increasing the life of implants such as the one proposed here.

15. SUBJECT TERMS
woven materials, cartilage wear, AFM, polymer welding

16. SECURITY CLASSIFICATION OF:			**17. LIMITATION OF ABSTRACT**	**18. NUMBER OF PAGES**	**19a. NAME OF RESPONSIBLE PERSON**
a. REPORT	**b. ABSTRACT**	**c. THIS PAGE**			USAMRMC
U	U	U	UU	101	**19b. TELEPHONE NUMBER** *(include area code)*

Table of Contents

INTRODUCTION

The overall objective of this project is to develop a three-dimensional polymer woven implant that replaces damaged areas of localized cartilage defects. To accomplish this, we determined whether the woven materials have the proper mechanical and wear properties for the application.

Because deformations and relative displacements between adjacent fibers are unavoidable, durability considerations required us to consider abrasive wear resistance on a fiber level. An early method to rapidly screen for fiber abrasion resistance used an atomic force microscope (AFM) with specially fabricated diamond-tipped stainless steel probes. Fiber-fiber wear resistance was measured on custom-designed equipment. Abrasion resistance of the bulk woven materials was also evaluated in wear testers to demonstrate that the woven composites maintain a reasonably long life.

Another aspect of this project was to provide a manufacturing process that improves the mechanical properties of three-dimensional woven materials. It has been shown that increasing friction within a fabric delays failure and increases the tolerable impact load of the fabric [Duan et al., 2005]. Instead of increasing friction by changing materials or consolidating the composite with a new resin, our approach was to weld them. We demonstrated that the through-thickness compressive strength and wear resistance can be improved through this welding process.

Finally, cartilage damage was a concern; because the implant will only replace one cartilage surface, it will wear against native cartilage in the joint. We developed a quantifiable approach to assess cartilage damage and wear through chemical analysis of the fluid from the hydrating bath and through the surface damage via india ink staining. Because the cartilage wear against the woven materials was severe, we investigated collagen crosslinking as a technique to improve the wear resistance of cartilage.

BODY

Below, we describe the progress and research accomplishments associated with each task outlined in the approved Statement of Work.

Evaluate Fiber Materials for Wear-Resistance: Mechanical Characterization of Polymer Fibers

This section addresses the wear resistance of individual polymer fibers to provide insight to material and weave selection, and to evaluate quick screening approaches for new materials. In any cartilage replacement produced from three-dimensional woven materials, each loading cycle will result in micro abrasion between adjacent fibers, and surface fibers will encounter significant sliding against opposing surfaces. For that reason, one of the important selection parameters for such materials is abrasive wear resistance at a number of sliding length scales. Macro abrasion tests and micro scratch tests have been previously described and are relevant to cartilage replacement materials.

Atomic Force Microscopy

All indentation and scratch tests described here are performed in an atomic force microscope (AFM) so that a relevant length scale is used. Polyetheretherketone (PEEK)

hardness results can be seen in Fig. 1 and sample indentations can been seen in Fig. 2. The increase of hardness at shallow depths of cut is attributed to the well documented indentation size effect (ISE) recorded first by early manufacturing researchers and modeled by a power relationship by Meyer [1908] and McHargue [1997]. Results of these tests suggest that the apparent hardness of PEEK increases in a fluid environment. Although these differences might not be statistically different, the apparent difference could be due to buoyancy effect. When the nanoindentation probe is lowered toward the sample surface within a fluid, buoyant forces act upon the tip in addition to ones due to normal loading. Since the AFM performs indentations in load control, the actual load during indentation in a fluid is less than the desired load due to the contribution of buoyancy. Since less load is transmitted to the surface, shallower indents are made, and a significant over-estimate to the actual hardness of the material is obtained.

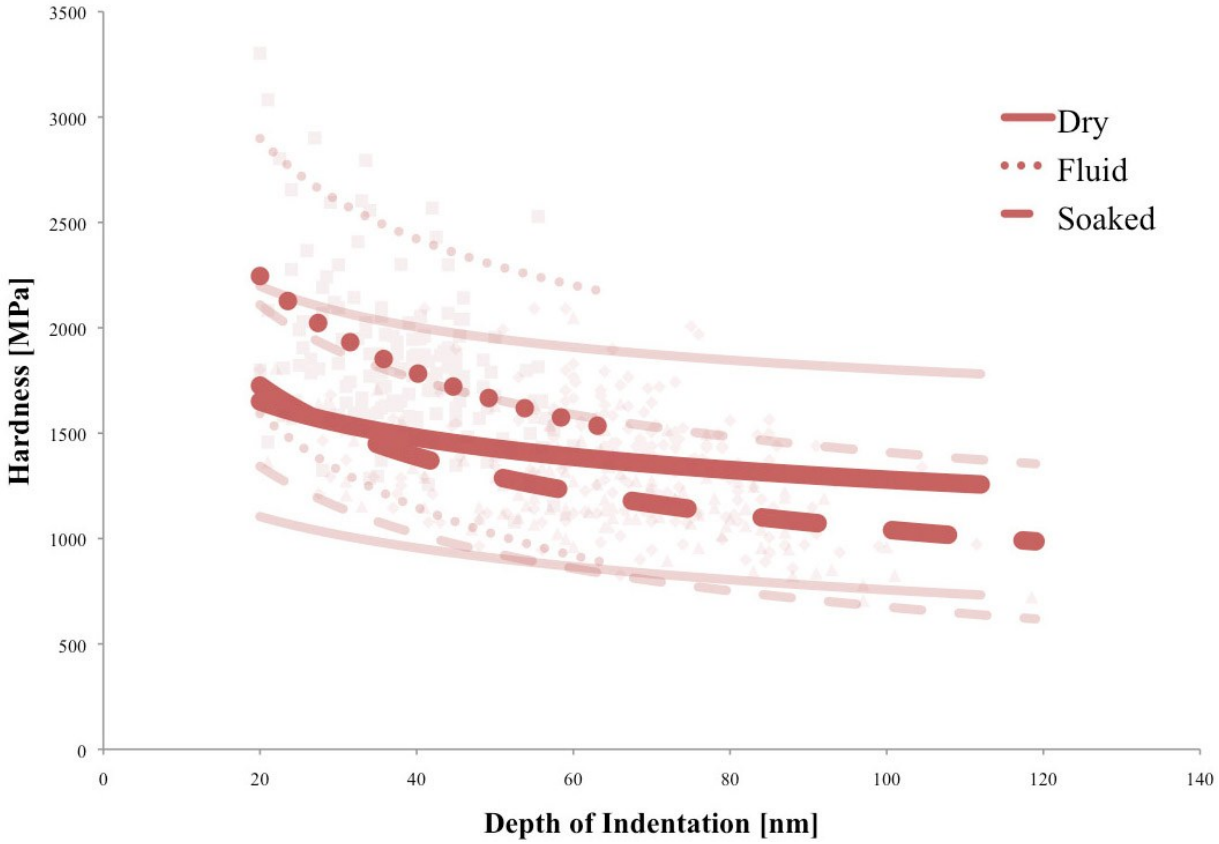

Figure 1: Indentation hardness of PEEK fiber evaluated in various environments.

Results of indentation tests performed on polyethylene terephthalate (PET) can be seen in Fig. 3 and sample indentations can be seen in Fig. 4. Surprisingly, these results indicate that PET exhibits no positive ISE; in fact, the material becomes softer at shallow depths of indentation. PET tested in a fluid environment appears harder possibly due to buoyancy effects

discussed previously. Soaking the material softens it and negates the buoyancy effects, thus providing similar hardness values between dry and soaked conditions.

Indentation results for polypropylene (PP) are shown in Fig. 5 with selected indentations seen in Fig. 6. Differences in hardness between environments are not statistically significant for PP, indicating that the material is not hygroscopic.

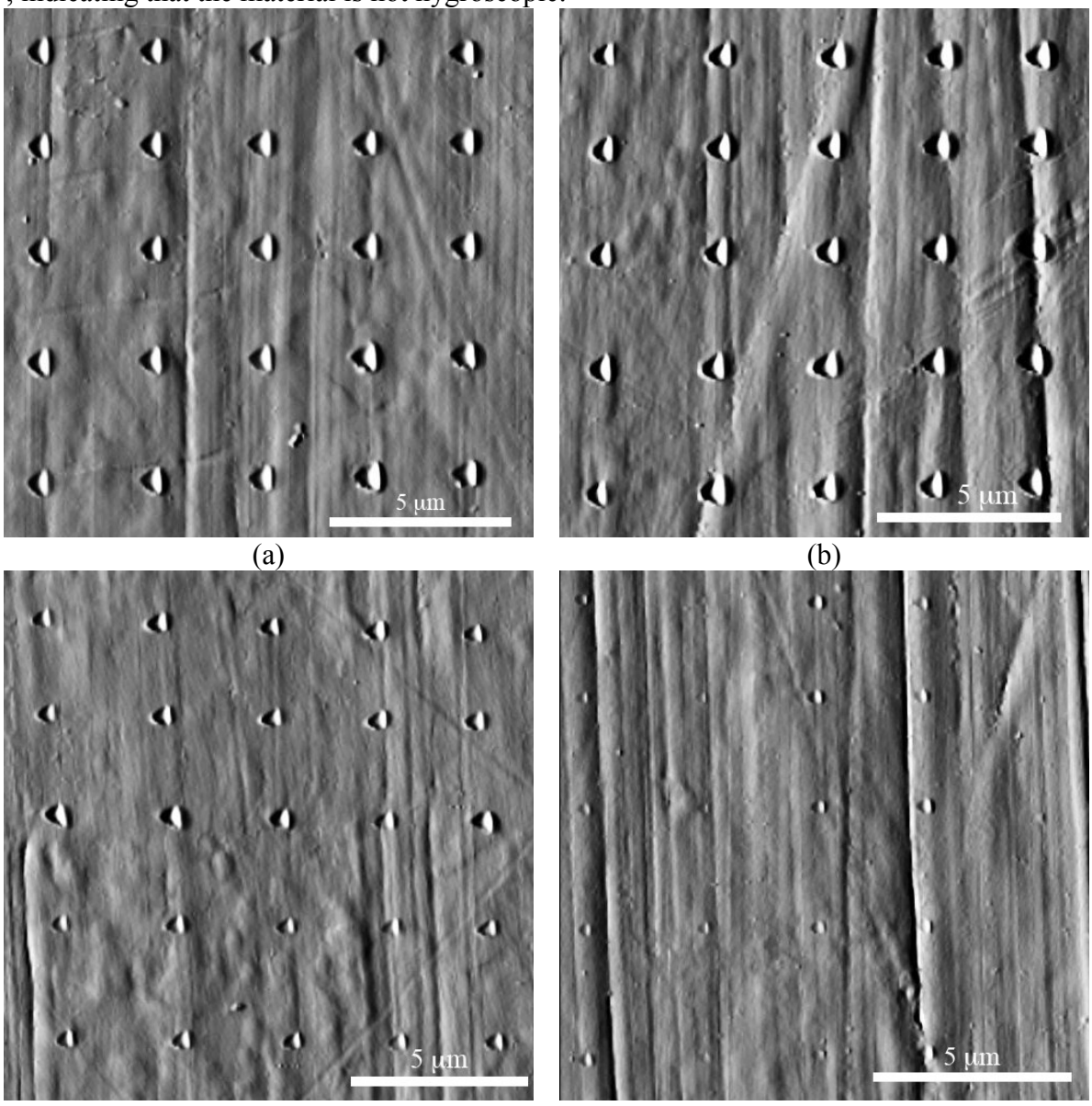

(a) (b)

(c) (d)

Figure 2: Selected indentations on dry PEEK fiber performed with normal loads of a) 372.5, b) 223.5, c) 149, and d) 74.5 nN.

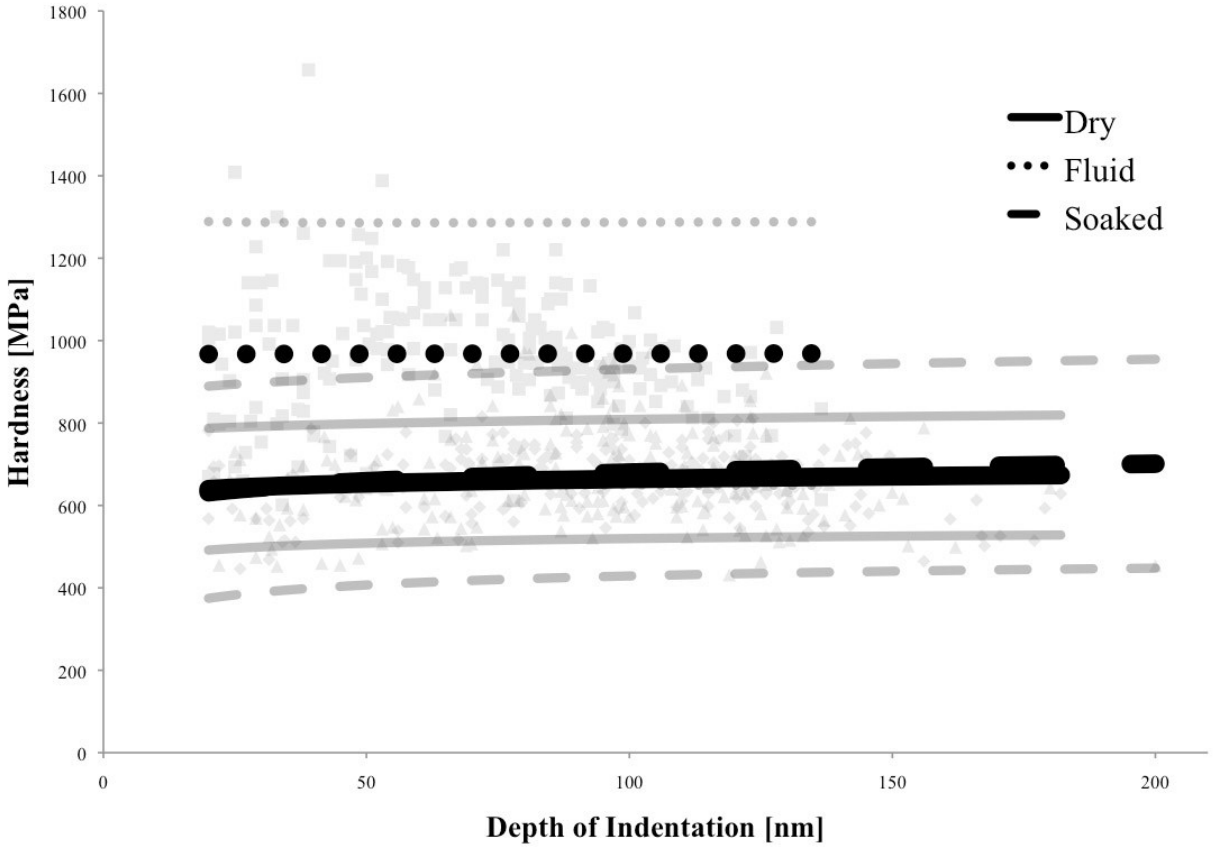

Figure 3: Scratch hardness of PET fiber evaluated in various environments.

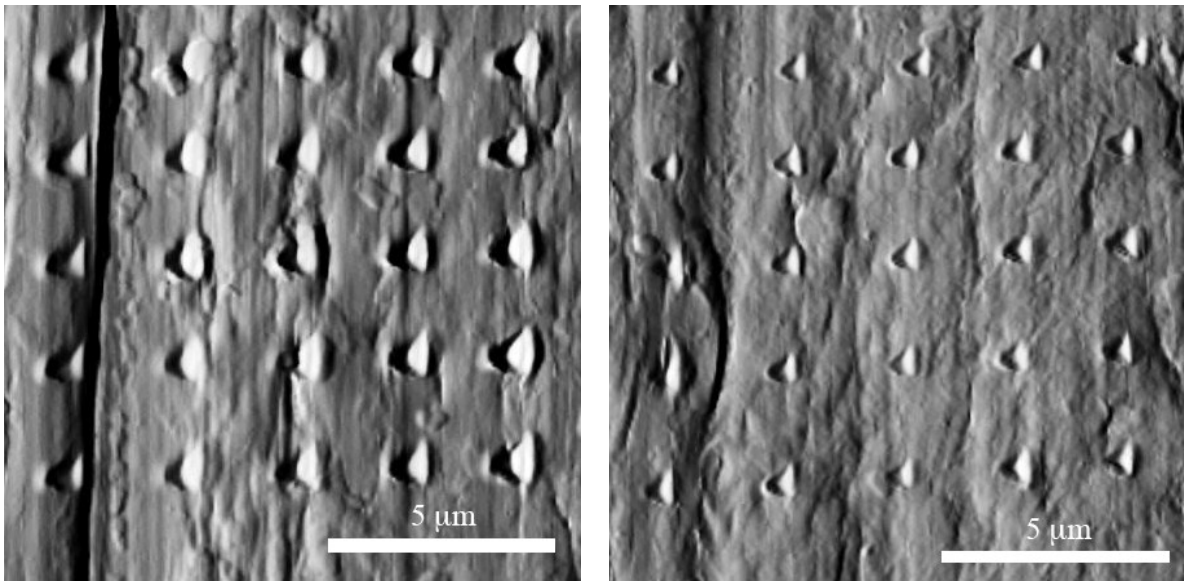

(a) (b)

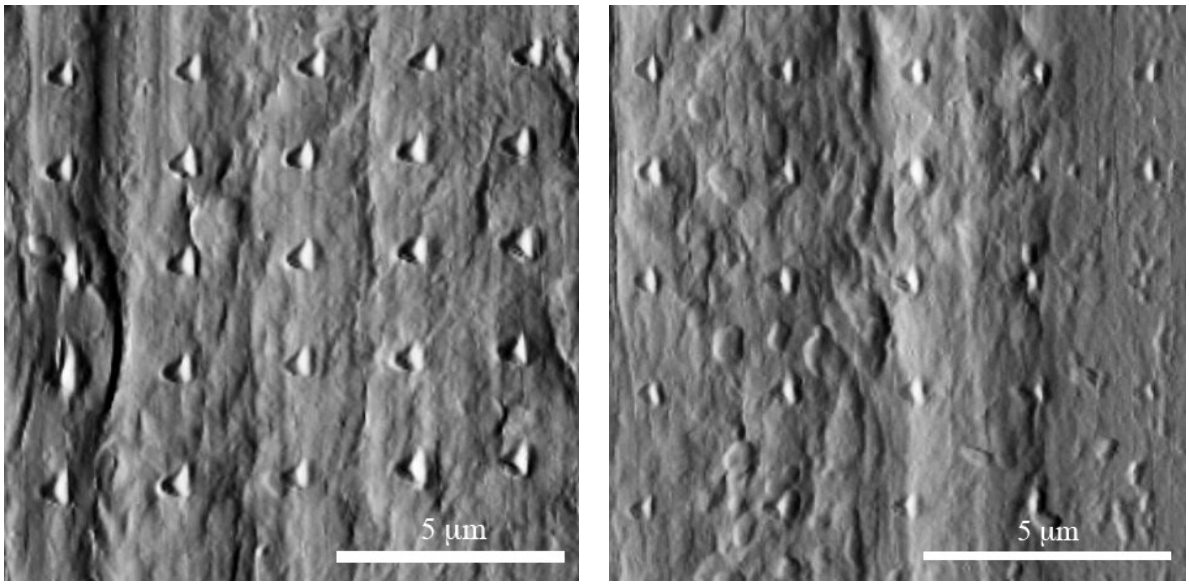

(c) (d)

Figure 4: Selected indentations on soaked PET fiber performed with normal loads of a) 372.5, b) 298; c) 149 and d) 74.5 nN.

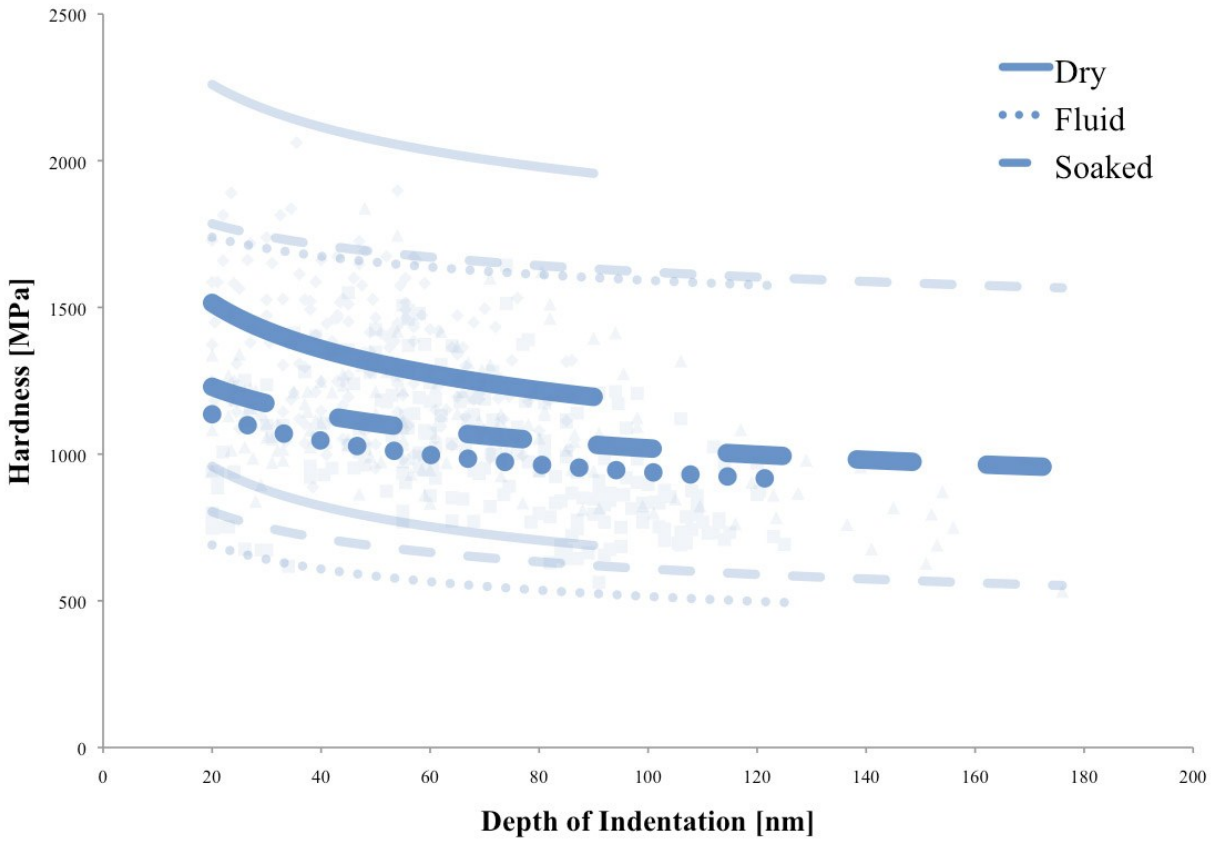

Figure 5: Scratch hardness of PP fiber evaluated in various environments.

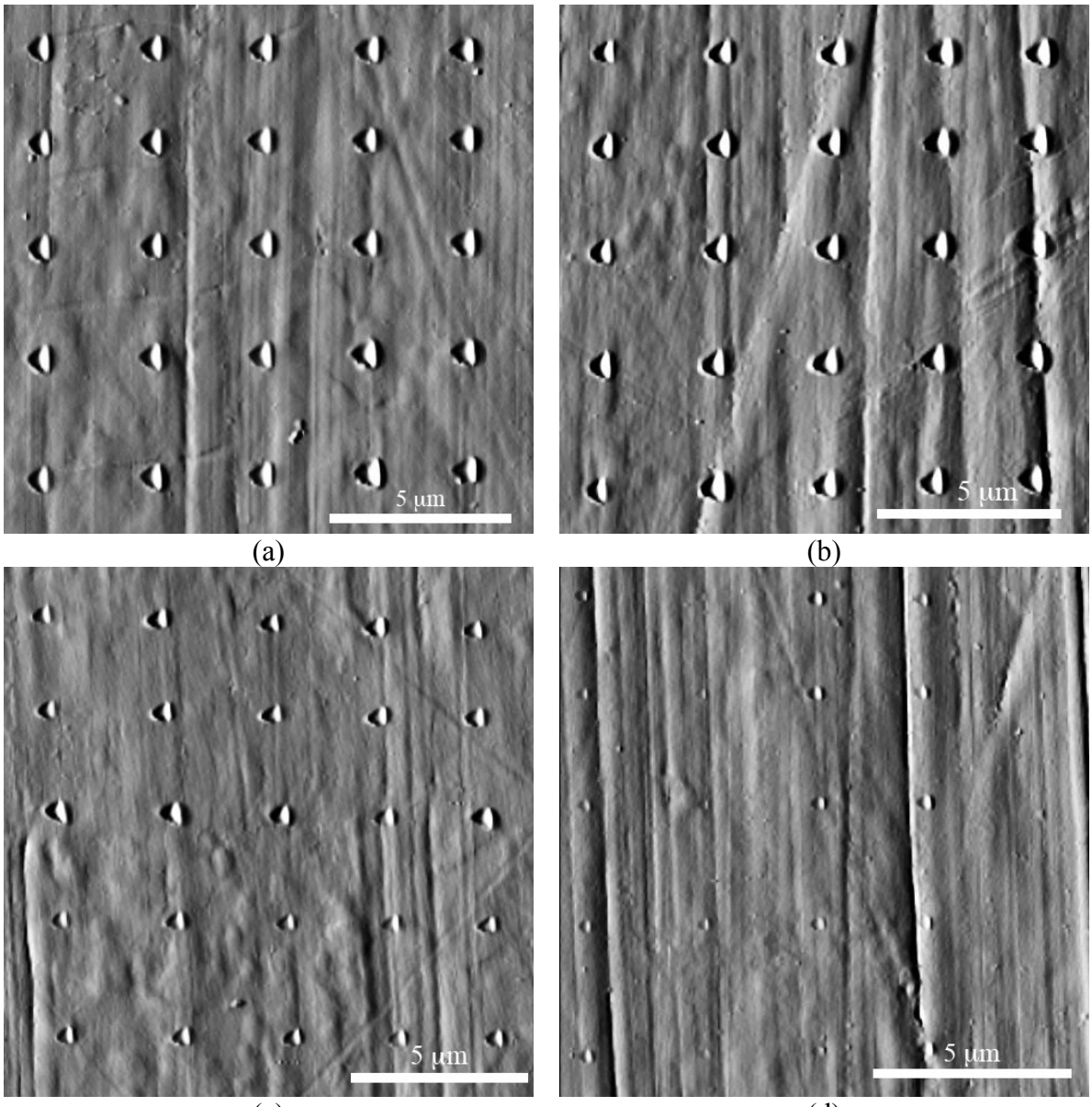

Figure 6: Selected indentations on soaked PET fiber performed with normal loads of a) 372.5, b) 298; c) 149 and d) 74.5 nN.

Fiber-Fiber Wear Apparatus

Ideally, wear events between weave fibers could be monitored and imaged as the wearing process occurs. This would provide the most accurate assessment of fiber wear within a three-dimensional fabric. Because imaging is difficult within a woven material, the apparatus shown in Fig. 7 has been designed to induce controlled wear events, allowing for rapid wear patch location and imaging. One fiber is held stationary while the other is attached to a torsion spring and servo motor (Hitec RCD, Poway, CA), serving to reciprocate a fiber against another. The normal load between fibers can be calculated using the torque in the torsion spring and geometry of the

pulleys surrounding the contact area. The tension in the translating fiber is

$$F_f = \frac{T}{r_{ts}} \tag{1}$$

where T is the torque in the torsion spring and r_{ts} is the radius at which the torque is applied to the pulley. The fiber angle, γ, can be expressed as

$$\gamma = tan^{-1}\left[\frac{d_f - r_p}{h_f - h'_f}\right] \tag{2}$$

where r_p is the pulley radius, d_f and h_f are the distances from the stationary fiber to the nearest pulleys and base, respectively, and h'_f is an offset to account for the distance between the base and the bottom of the pulleys. The normal load between the fibers is

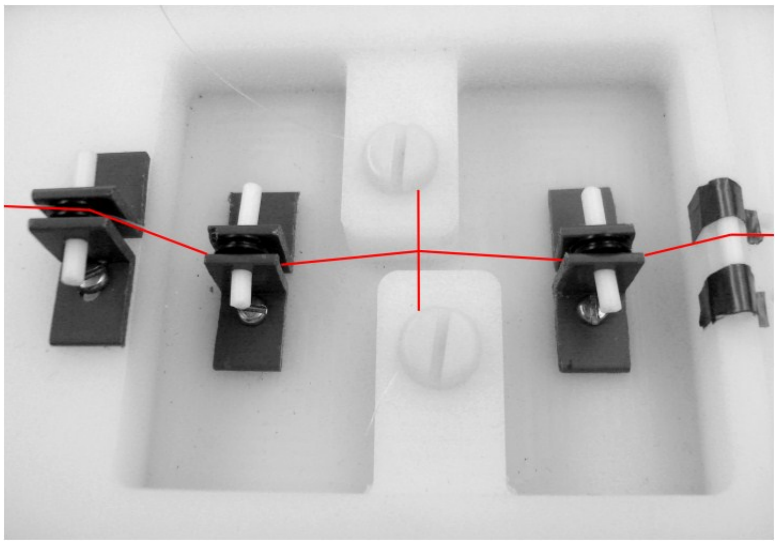

Figure 7: Micro-scale wear test between two fibers. One fiber is held in place by two nylon screws and the other orthogonally translates across it. Subsequent imaging of the wear spot allows for wear volume, surface morphology, and debris size to be determined.

$$N_f = 2F_f \cos\gamma \tag{3}$$

Parameters that can be varied in this setup include fiber materials, normal load, sliding distance, and number of cycles. Sliding distances used in the apparatus are significantly longer than would be seen in service and allow for accelerated life testing. The sliding distance has been set to approximately 20 mm, which ensures that a viable portion of the torsion spring is activated to yield smooth and reproducible loading.

Two phases of testing were performed; Phase I includes only self-mated monofilament fibers and investigates the effects of speed, load, and number of cycles. Two values of speed and load were chosen as 14 and 63 mm/s, and 0.3 and 1.0 N, respectively. During Phase II, multifilaments are included among the translating fibers and tests were performed using a speed

of 63 mm/s and load of 0.3 N. The second phase allowed more materials to be tested without greatly increasing the required number of runs.

During Phase I testing, monofilament poly(ether-ether-ketone) (PEEK) and polyester (PET) were used. Phase II testing included the addition of monofilament titanium (Ti) and nylon, and multifilament fibers of PET, PEEK, and ultra-high molecular weight polyethylene (UHMWPE). While titanium is not thought to be a viable material for the surface of a cartilage replacement, a metal wire may find use in the substrate weave to provide greater stiffness if desired or to serve as a scaffold for tissue integration. Also, titanium is of interest because of the occasional use of two-dimensional weaves or meshes in-vivo [Fujibayashi et al. 2004, Pederson et al. 1991, Sugar et al. 1992].

Stationary fibers were limited to monofilament PET, PEEK, and nylon to allow for more accurate calculations of wear volume. Although titanium was also available as a monofilament, initial testing confirmed that titanium showed no significant signs of wear when paired with a translating polymer fiber.

After performing each experiment, the wear patch on the stationary fiber was examined, with a sample patch shown in Fig. 8. Dimensions of the wear patch were measured using optical microscopy since this approach was determined to be the most efficient method for assessing patch size and morphology. Giordano and Schmid [2012] show that the volume of worn material is given by

$$V = 2\int_0^{h_{\max}/2} \frac{1}{2} w(y)\sqrt{r_s^2 - w(y)^2} - \frac{1}{2} r_s^2 \tan^{-1}\left[\frac{w(y)\sqrt{r_s^2 - w(y)^2}}{w(y)^2 - r_s^2}\right] - yw(y)\,dz \qquad (4)$$

The volume of removed material given by Eq. (4) can be used in the Archard wear equation [1953], to estimate the wear coefficient and produce a relative ranking of wear resistance. These coefficients will vary depending on material pairings and loading conditions but will allow a quantification of wear events in each situation.

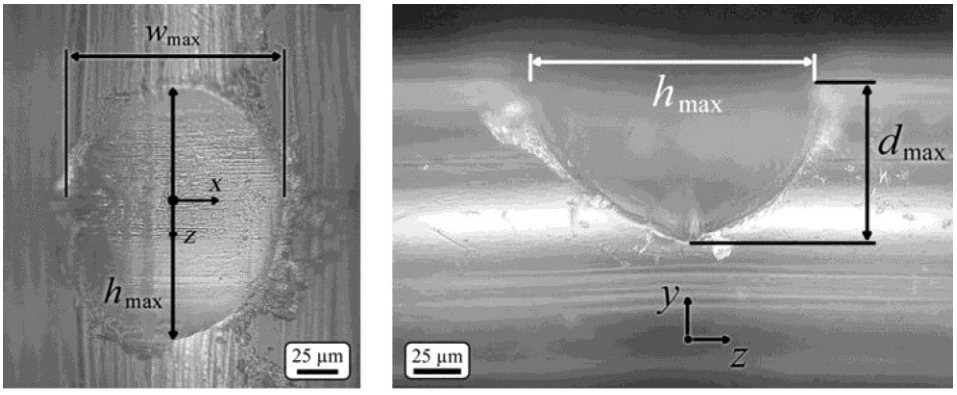

(a) (b)

Figure 8. (a) Top and (b) side views of resulting wear patches after the translating fiber has been removed. The values $w_{\max}$ and $h_{\max}$ are measured directly and $d_{\max}$ is calculated based on fiber radii.

In order to investigate the effects and importance of the various parameters on wear volume and wear coefficient, the commercial software package Design-Expert® (Stat-Ease, Inc., Minneapolis, MN) was used as a design of experiments (DOE) tool to develop an efficient rubric of tests and to analyze the results via a response surface method. By defining a desired design space and setting upper and lower limits to parameters, a factorial design aids selection of test values. Instead of performing a "full-factorial" experiment, during which values of each parameter are rotated such that every combination is tested, a "fractional-factorial" design is derived in which parameter combinations are chosen to provide sufficient data for response surface generation. Regression analysis of the data provides the response surface and confidence limits. By eliminating the need to test every parameter combination and selectively choosing test values, the number of experiments is greatly reduced without a significant loss of precision. Redundancy is added to further reduce error and to gauge variability in the results.

A two-factor interaction model was deemed significant by Design-Expert® with R2 = 0.90 and was used to describe the response surface for wear volume. Material, cycles, and load were found to be significant factors while speed was determined to be insignificant. A linear response surface was used to model wear coefficient. Material and load were the only significant factors and PET exhibited consistently lower wear coefficients than did PEEK.

Distinct wear patch and debris morphology were observed from the worn PET and PEEK fibers. Wear patches created between two PET fibers exhibited clearly defined worn volumes with light debris uniformly surrounding them; sample images are shown in Figs. 9a and b. Transverse lines across the wear patch were noticeable but not prominent. When PEEK fibers were used, more debris was present and accumulation around the wear patch was not symmetric, as seen in Figs. 9c and d. Debris was found attached to one side of the wear patch and the transverse marks within the patch were more significant than with PET.

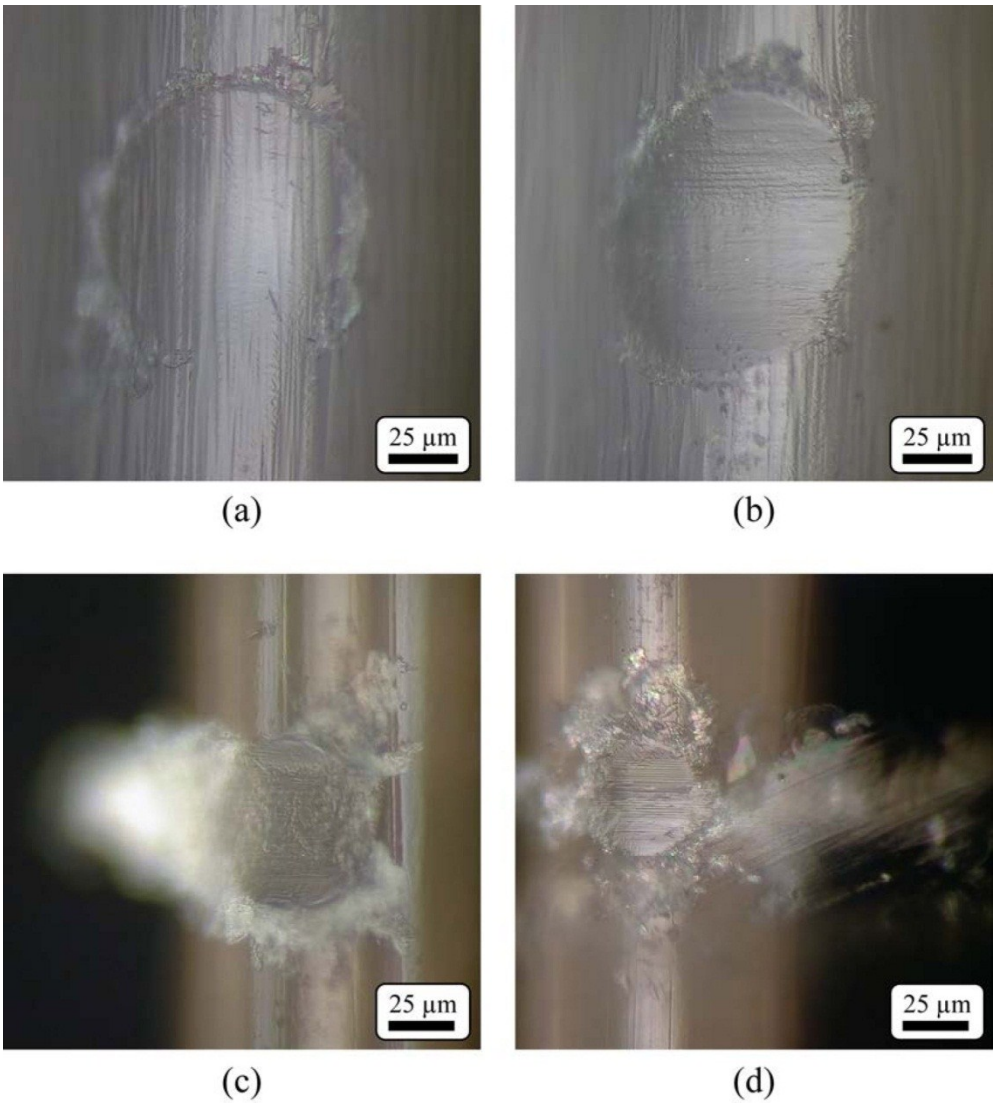

Figure 9. Wear patches for (a-b) self-mated PET fibers and (c-d) self-mated PEEK fibers. Testing variables are 1 N at 63 mm/s for (a) 5 cycles, (b) 1000 cycles, and 0.3 N at (c) 14 mm/s for 500 cycles, and (d) 63 mm/s for 1000 cycles.

As with self-mated polymers, a two-factor interaction model was used to describe the response surface for wear volume. Both the number of cycles and material of the translating fiber were determined to have significant effect on the wear volume but the stationary fiber material was found to be insignificant. For example, Figs. 10a-c shows stationary PET, PEEK, and nylon fibers after being worn by a translating PET monofilament. All wear patches exhibit characteristics of the PET-PET tests. Figure 10d-f show the same fibers when worn by a translating PEEK monofilament; wear patch morphologies closely resemble that seen by PEEK-PEEK testing. The same is true of the fibers in Figs. 10g-i, which have been worn by a translating titanium monofilament. Regardless of the stationary fiber material, the wear volumes created by titanium are significantly larger than those created by a translating polymer fiber.

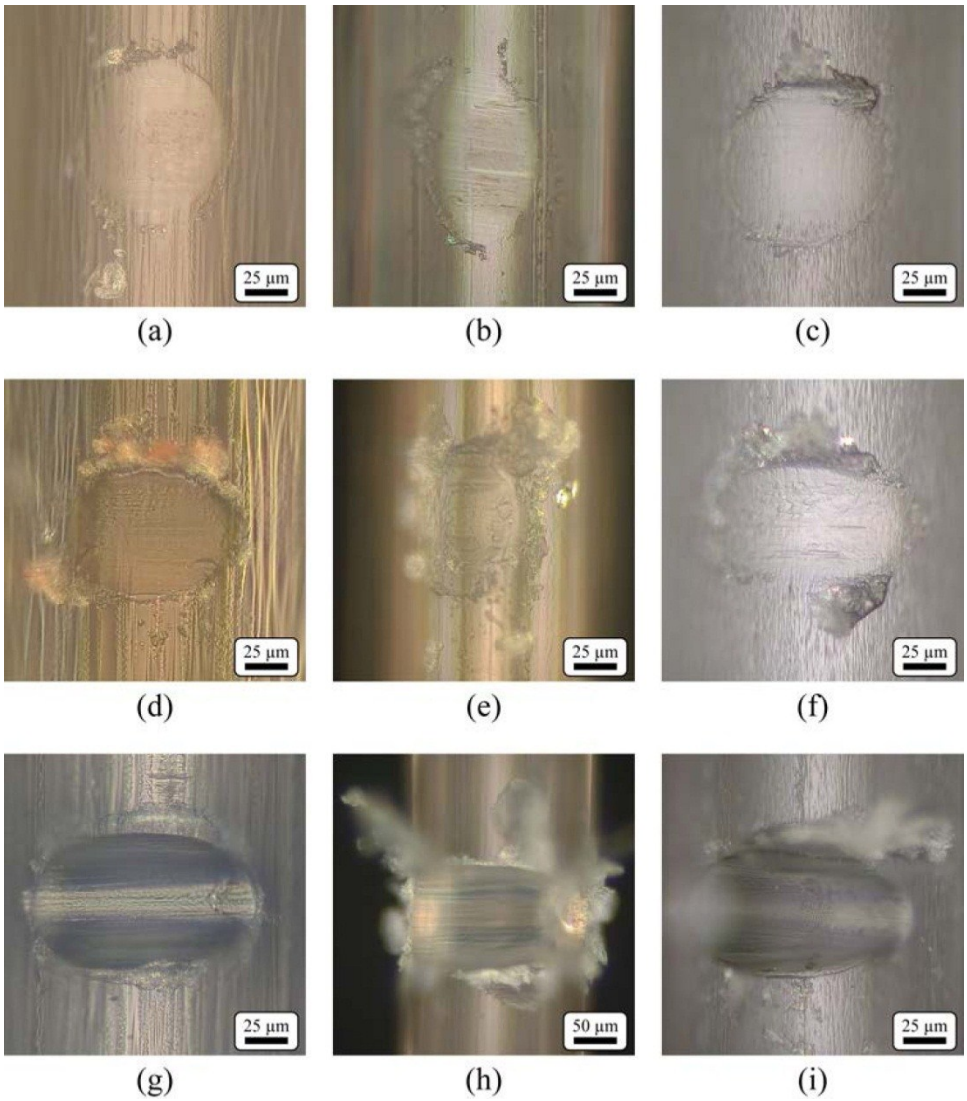

Figure 10. Wear patches from tests involving a (a-c) PET, (d-f) PEEK, and (g-i) titanium monofilaments as the translating fiber during Phase II of testing. Tests were performed using a normal load of 0.3 N and sliding velocity 63 mm/s. Stationary fiber material and number of cycles are (a) PET for 339 cycles, (b) PEEK for 1000 cycles, (c) nylon for 433 cycles, (d) PET for 802 cycles, (e) PEEK for 865 cycles, (f) nylon for 339 cycles, (g) PET for 100 cycles, (h) PEEK for 92 cycles, and (i) nylon for 100 cycles.

When multifilaments were used as the translating fiber, wear patch morphology changed drastically. Instead of creating a large depression of removed material, the individual fibrils of the multifilament created tiny wear patches of their own. Optical microscopy revealed that the fiber surface between the patches remained virtually unaltered. This indicates that individual filaments did not move along the axial direction of the stationary fiber during testing, instead their movement was only in the direction of translation. It was noted during testing that the multifilament fiber conformed to the surface of the stationary fiber when loaded. The fibrils arranged themselves such that the geometry of the fiber was more ovular in shape, thus spreading the load over a larger contact area.

Figure 11 shows stationary PET, PEEK, and nylon fibers worn by translating PET,

PEEK, and UHMWPE multifilaments, respectively. It can be seen that wear debris corresponds to that of the translating fiber. Again, these observations are in agreement with the statistical insignificance of translating fiber material with respect to wear volumes and coefficients.

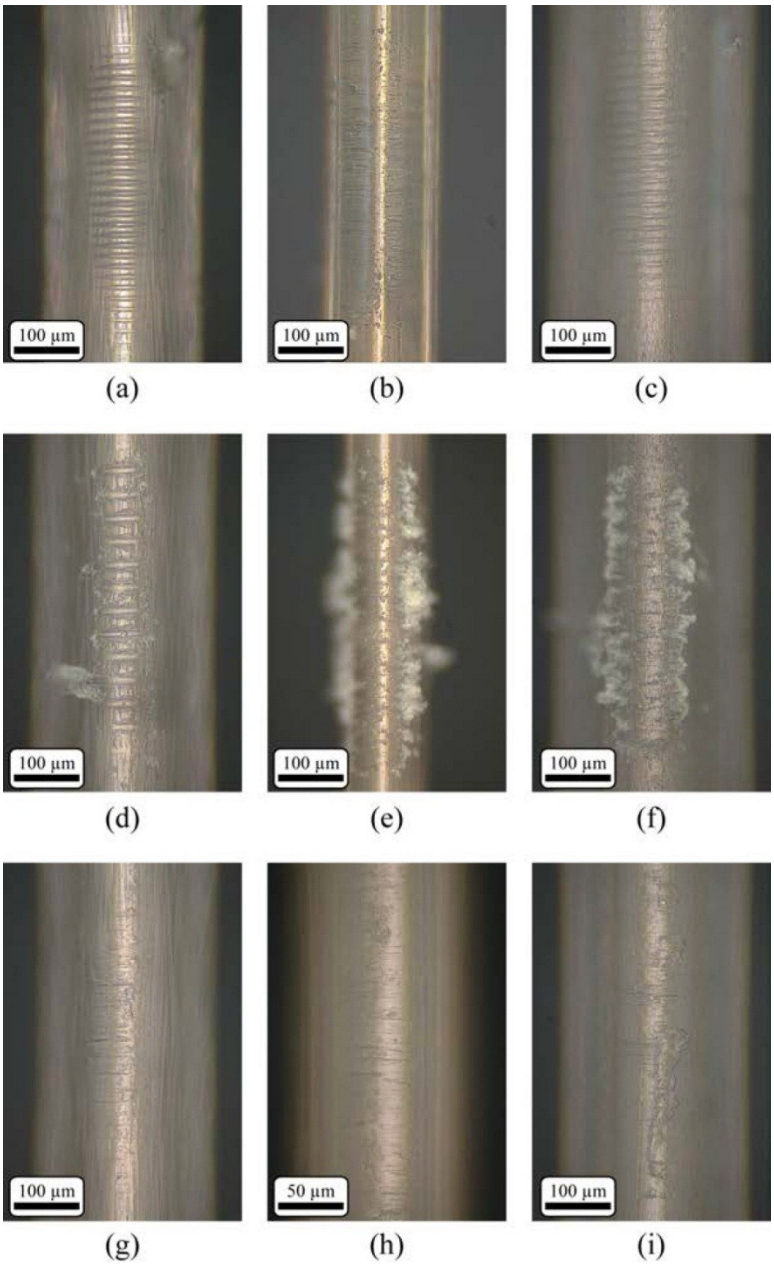

Figure 11. Wear patches for (a-c) PET, (d-f) PEEK, and (g-i) UHMWPE multifilament as the translating fiber during Phase II of testing. Tests were performed using a normal load of 0.3 N and sliding velocity 63 mm/s. Stationary fiber material and number of cycles are (a) PET for 1000 cycles, (b) PEEK for 100 cycles, (c) nylon for 636 cycles, (d) PET for 644 cycles, (e) PEEK for 303 cycles, (f) nylon for 438 cycles, (g) PET for 906 cycles, (h) PEEK for 559 cycles, and (i) nylon for 267 cycles.

Discussion

Comparing wear coefficients allows a relative ranking of wear resistance to be established. Those fibers with low wear coefficients are attractive for more advanced testing; those with high wear coefficients can quickly be identified as unacceptable candidates. Results from the current study are summarized in Fig. 12. It can be seen that multifilament UHMWPE provides the lowest wear coefficient and is thus identified as the most wear resistant of the materials tested. The titanium fiber clearly performed the poorest, causing severe wear of all opposing polymer fibers. Unlike the polymer fibers, the titanium was drawn with a lubricant that became trapped in pockets on the surface of the metal, seen in Fig. 13. These pockets formed sharp ridges, a common occurrence for strain-hardened metals during squeeze film operations like drawing [224], which increased the roughness of the titanium fiber. Typical RMS roughness of the titanium fiber surface is 125 nm, compared to the polymer fibers with RMS values of 30 nm (PP), 35 nm (UHMWPE), 40 nm (PET), 50 nm (nylon), and 80 nm (PEEK). The sharp titanium asperities combined with the high material hardness resulted in rapid polymer wear. Roughness of the polymer samples has much less effect since roughness is most likely decreased within the first few cycles of testing [Litwin 2011].

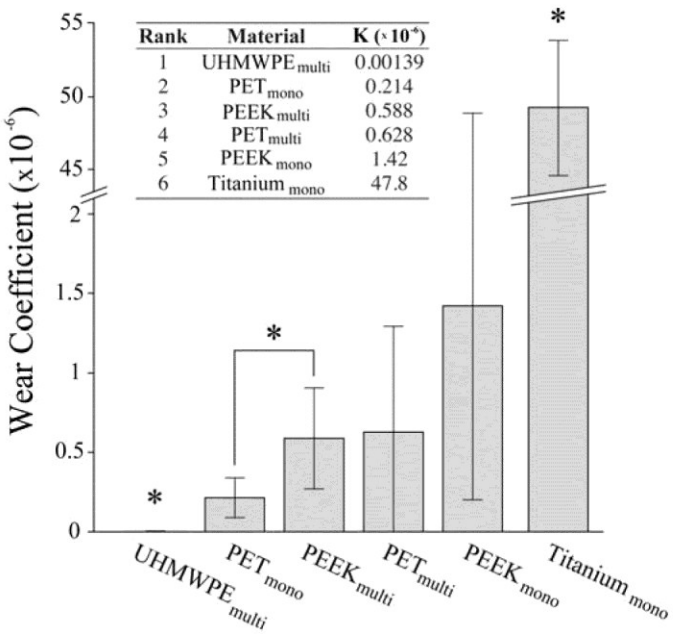

Figure 12. Wear coefficients for each of the translating fibers examined and their respective rankings. Single unpaired asterisks denote statistical differences when compared to all other materials.

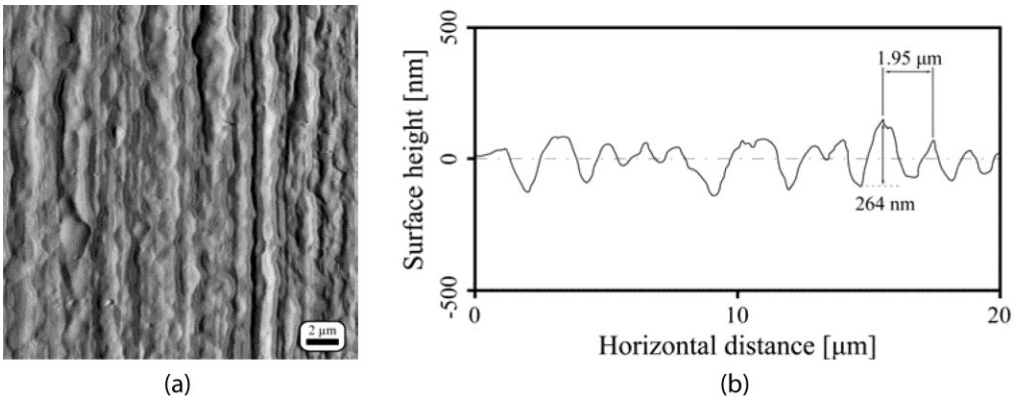

Figure 13. (a) Surface topography and (b) cross-section of the titanium monofilament.

When contact between two polymer samples is considered, adhesion is likely to play an important role. It is hypothesized that adhesion and the highly plastic nature of the samples contributed to the debris formation and buildup. Based on the insignificance of stationary fiber material on debris morphology, it is likely that significant amounts of debris transferred between fibers. This could explain why debris found near the wear patch was dependent only on translating fiber material. Any debris from the stationary fiber was transferred to the translating one and carried away from the contact area. The possibility of material compaction and densification inside the wear patch has also been investigated. It is possible that the material assumed to be worn away is instead plastically deformed and compacted below the wear patch. If this were the case, the material at the bottom of the patch would have different mechanical properties. Indentation tests were performed inside a wear patch and on the fiber outside the patch. There was no statistical difference found between the two groups of indentations. It is assumed that the material lost in the wear patch was through a combination of abrasion and adhesion.

The results of these tests are in agreement with previous experiments that identified PET and UHMWPE as materials deserving further testing. The previous tests also indicated a mono- and multifilament pair would provide better abrasion resistance than two monofilaments. Although this result was observed in the previous experiments, it was unclear why this occurred. The visual results of the current study reveal that a multifilament will deform via fibril rearrangement even under very light loads. Each fibril then acts as a translating fiber and creates its own wear patch. These patches are much smaller and support significantly less load. In effect, the volume of removed material for a multifilament is distributed more along the axis of the stationary fiber whereas the volume for a monofilament is concentrated directly under the contact area. Although the wear volume might not significantly decrease, or in fact might increase, the time to failure will be extended since the volume of lost material is distributed along the axis of the fiber.

Evaluate Fiber Materials for Wear-Resistance: Wet characterization of hydrogel fibers

Although hydrogel fibers can be woven, they did not prove to have sufficient strength for this application. Some hygroscopic materials were selected that would serve the same purpose, and

these have been evaluated. They are included in the discussion of wet testing of fibers contained above.

Develop Welded/Woven Materials: Evaluation of Toner and Process Parameters for Welding Fibers

As a first step in understanding polymer welding within fabrics, the behavior of welding at individual fiber-fiber contact sites must be understood. Polyethylene terephthalate (PET) yarns have been chosen to study the fiber-to-fiber welding process.

Laser welding of transparent polymers requires that a near-infrared absorbing material be added to the polymers prior to welding. This material can be in the form of a resin added during the manufacturing of the polymers or in the form of a liquid coating that can be applied in a variety of ways. The liquid coating method is being used throughout the entirety of this investigation. The product in use is the commercially available Clearweld® coating by Gentex Corporation (Binghamton, NY). Gentex selected two different versions of the coating for our application. The first was LD120C, which had an acetone base, and the second was LD140F, which is an ethanol base, both of which are intended for use with diode lasers with a 1000 nm wavelength.

Both versions of the coating are highly concentrated and initially destroyed fabrics when trial welds were attempted at 10% rated laser power. As a result, the Clearweld® product is diluted to reduce the concentration of the near-infrared absorbing component of the coating. An array of concentrations of each coating is created from a 1:1 concentration of reagent:Clearweld® to a 20:1 concentration of reagent:Clearweld®. Clearweld® LD120C is diluted with A.C.S. reagent quality acetone and Clearweld® LD140F is diluted with A.C.S. reagent quality ethanol.

The Clearweld® coatings are handled using 28 gauge insulin syringes. Approximately one tenth of a milliliter of Clearweld® is extracted from the vial with the syringe and a drop is applied to the fibers, which spreads along the majority of the fiber due to wicking. The fibers are allowed to dry for fifteen minutes before being handled. Once the fibers dry, the near-infrared absorbing material within the coating remains on the fibers.

Several parameters are identified as being critical to the welding process. An optimized solution for welding each of these polymer fibers is sought. The five parameters identified are laser speed, laser power, optics height, Clearweld® type and Clearweld® concentration. The most efficient way to manage the five parameters and to potentially determine an optimal solution for welding the fiber-fiber interaction is to use a Design of Experiments (DOE) approach.

The software package Design Expert 8.0 was employed to build a design of experiments matrix to evaluate the parameters and optimize system response. The quality of the welds was characterized according to weld strength. Each weld in the experiment matrix was subjected to a testing regime that applies a load to one of the two mating fibers. The load is then transferred across the weld zone to the second mating fiber, which is suspended from above. The optimum conditions for each fiber and material were determined and applied to produce selectively welded-woven materials.

Attempts to weld PET fibers resulted in four visually and qualitatively distinct categories (Fig. 14):

1. No Weld
2. Welded Fibers
3. Weld with Polymer Degradation

4. Severed Fibers

It was hypothesized that some fiber pairs would not weld and some would sever, even though the DOE was designed based on information gathered for the purpose of screening each of the four numeric factors.

Seventy-two Clearweld® -coated, PET fiber pairings were processed with the near infrared laser under no tension. Of the seventy-two samples processed, 82% demonstrated a weld of some varying degree (Table 1). Even without conducting weld strength tests, it is clear that the strength of the weld in thirteen samples is 0 MPa. The eight samples of Category 1 have no weld; to express this numerically, they have a weld of 0 MPa. Additionally, the five samples of Category 4 were so severely damaged by the laser radiation that the continuity of the PET fiber was disrupted; one or both of the fibers was severed. These five samples have no weld; also expressed numerically as a weld of 0 MPa (Fig. 15).

Table 1: Distribution of samples by category.

Category	**Number of Samples**
1. No Weld	8
2. Welded Fibers	47
3. Weld with Polymer Degradation	12
4. Severed Fibers	5

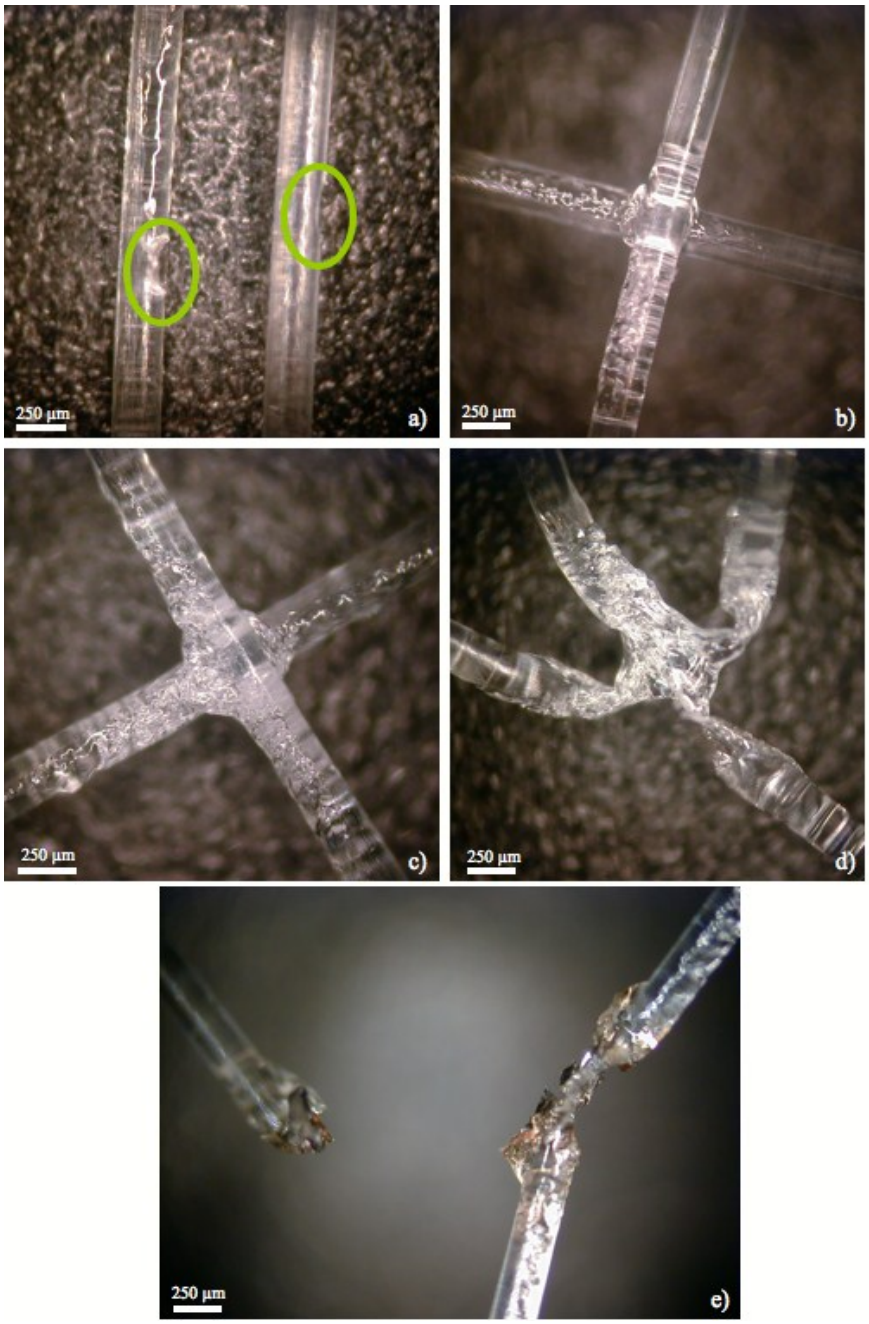

Figure 14: Examples of each category. a) No weld. b) and c) Welded Fibers. d) Weld with Polymer Degradation. e) Severed Fibers.

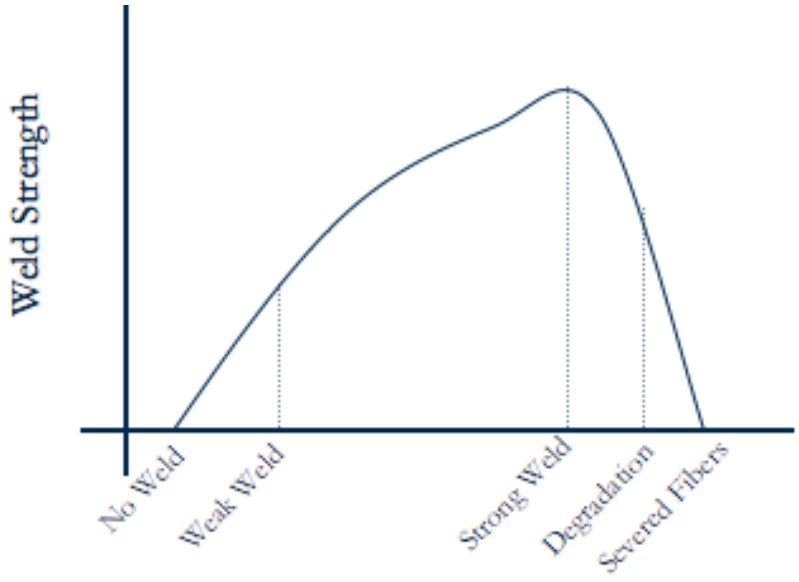

Figure 15: Schematic of weld strength response.

The forty-seven samples that have welded fibers have an unknown weld strength that exists somewhere between "No Weld" and "Degradation" on the schematic. Additionally, the twelve fibers from Category 3 exist somewhere between "Degradation" and "Severed Fibers". These fibers, though damaged, still possess some strength at the interaction of the two individual fibers. Thus, the Category 3 fibers must be tested for weld strength.

Initially, the results suggest that the design space is well explored because the extremes of the response (Weld Strength) are well characterized. Most of the samples are eligible for weld strength testing and, from visual inspection, appear to have varying quality welds.

Fiber-Fiber Weld Strength Tests

Each of the 59 eligible samples was tested for weld strength. Forty-four of the samples that were tested ruptured cleanly at the weld zone, resulting in two complete loops (each loop is one of the original fibers). An ideal rupture of the weld captures the full strength of the weld over the entire surface area of the weld (Fig. 16).

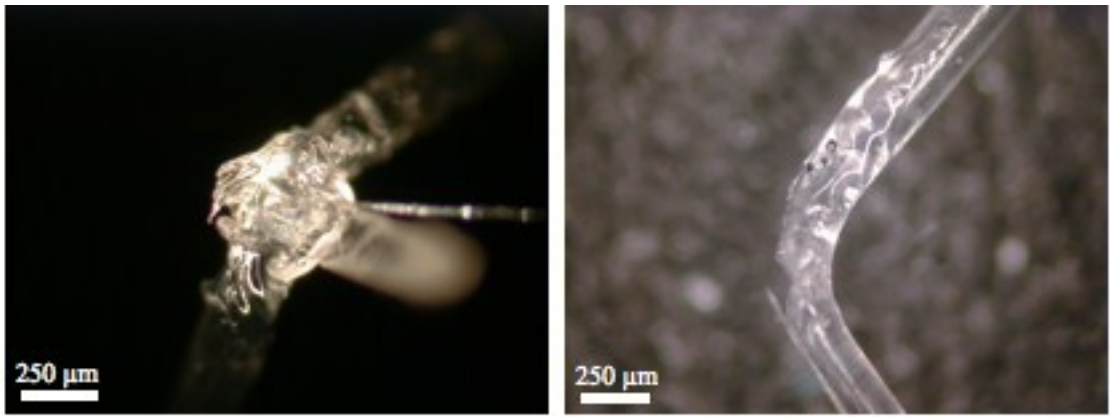

Figure 16: Each image is one fiber from an ideal weld rupture.

The other fifteen of the samples ruptured incompletely at the weld zone. In most of these cases, the bottom fiber ruptured on only one side of the weld zone. As a result, the sample at the conclusion of the test was one loop with a single fiber attached at the weld zone. The rupture at the weld zone was photographed under 4x magnification (Fig. 17). Considerable necking of what appears to be degraded polymer at the weld zone appears to be the failure mode for the incomplete rupture.

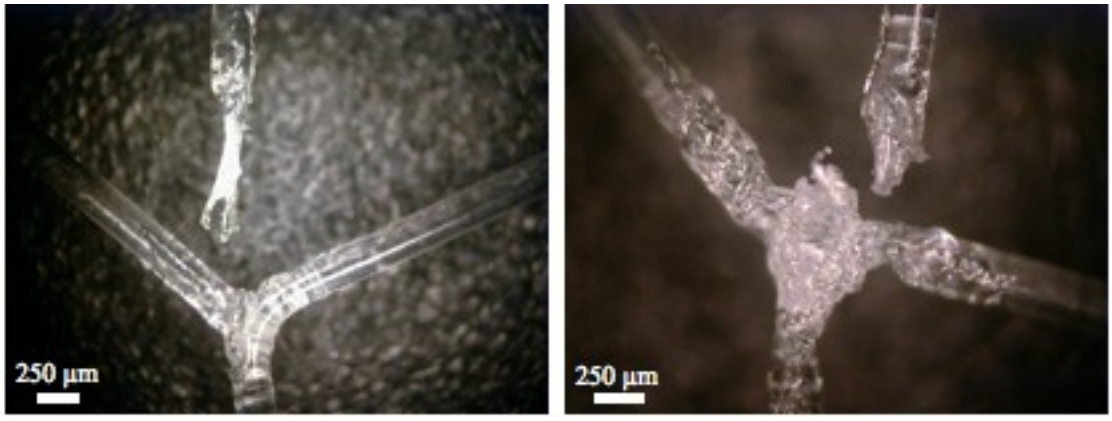

Figure 17: Incomplete rupture failure mode.

While this failure does not fully capture the strength of the weld, the center of the weld zone is guaranteed to able to withstand a greater load than the site of failure. Thus, the strength at the center of the weld zone is known to be at least as strong as the weld strength calculated as though the load caused failure over the full area of the weld zone.

Weld strengths for all seventy-two samples were entered into the DOE using Design Expert® 8.0.4 by Stat-Ease, Inc. Five parameters are included in the analysis to follow. Four numeric factors (A=Power, B=Speed, C= Focal Length and D=Clearweld® Concentration) and one categoric factor (E=Clearweld® Type) are analyzed for significance with the quadratic model using built in ANOVA significance testing. Regression is performed using backward elimination to determine the significant parameters (Table 2). Speed and Focal Length (B and C respectively) are only significant and included to support model hierarchy.

Rank	Parameter	F-Value		Rank	Parameter	F-Value
1.	B^2	22.41		7.	C^2	10.69
2.	A^2	20.88		8.	AD	2.95
3.	AC	16.77		9.	A	2.89
4.	AB	14.68		10.	D	2.84
5.	E	13.80		11.	B^*	1.31
6.	D^2	10.83		12.	C^*	0.83

Table 2: Model parameter ranked by significance from regression.

As expected, Laser Power (A) appears to have the most widespread effect on the model for weld strength. The interaction between Laser Power and Focal Length (AC) and between Laser Power and Laser Speed (AB) are highly significant as well. Clearweld® Type (E), either Acetone based or Ethanol based is a dominant factor in the model. A specific model for weld strength, *WS*, is given for each of the two Clearweld® Types

$$WS_A = -107.82 - 3.47A + 3.24B + 3.13C + 2.27D + 0.12AB + 0.039AC + 0.055AD - 0.051A^2 - 0.30B^2 - 0.018C^2 - 0.21D^2 \quad (5)$$

$$WS_E = -119.88 - 3.47A + 3.24B + 3.13C + 2.27D + 0.12AB + 0.039AC + 0.055AD - 0.051A^2 - 0.30B^2 - 0.018C^2 - 0.21D^2 \quad (6)$$

The difference between the model for the Acetone based Clearweld® given in Eq. (5) and the Ethanol based Clearweld® in Eq. (6) is the 12.1 MPa increase in weld strength for the Acetone model.

A routine to locate optimal solutions of the model is implemented based on defined criteria. All parameters are constrained to be within the minimum and maximum values of the design space, which eliminates the potential for extrapolation beyond the design space. The dominant criteria for the optimization routine are to maximize the weld strength within a region of 36.80 MPa to 71.36 MPa (50% and 100% of the largest experimentally observed weld strength, respectively) and to minimize the standard error of the model. After applying a weak filter for similar solutions, three optimized solutions were revealed (Table 3). The values in Table 3 were used to produce the welded-woven fabrics investigated below.

Solution	Power [W]	Speed [mm/s]	Focal Length [%]	Clearweld® Concentration [Reagent:Clearweld]	Clearweld® Type	Weld Strength [MPa]
1	36.53	13.31	127.96	10.30	Acetone	57.71
2	22.78	9.95	107.87	7.45	Acetone	56.12
3	36.11	13.11	126.82	10.27	Ethanol	45.74

Table 3: Optimized solutions of the weld strength model.

Develop Welded/Woven Materials: Design Fixtures for Loading 3D Weaves

A confined compression creep test was proposed to load 3D fabrics and determine their aggregate stiffness. The test requires that only uniaxial deformation of the sample be allowed during loading. To achieve this, the sample must be placed in a 6.35 mm confining chamber as described by Mow et al. [1984] (Fig. 18). A similar chamber was designed to work with an existing, unconfined compression creep apparatus at Zimmer, Inc (Warsaw, IN).

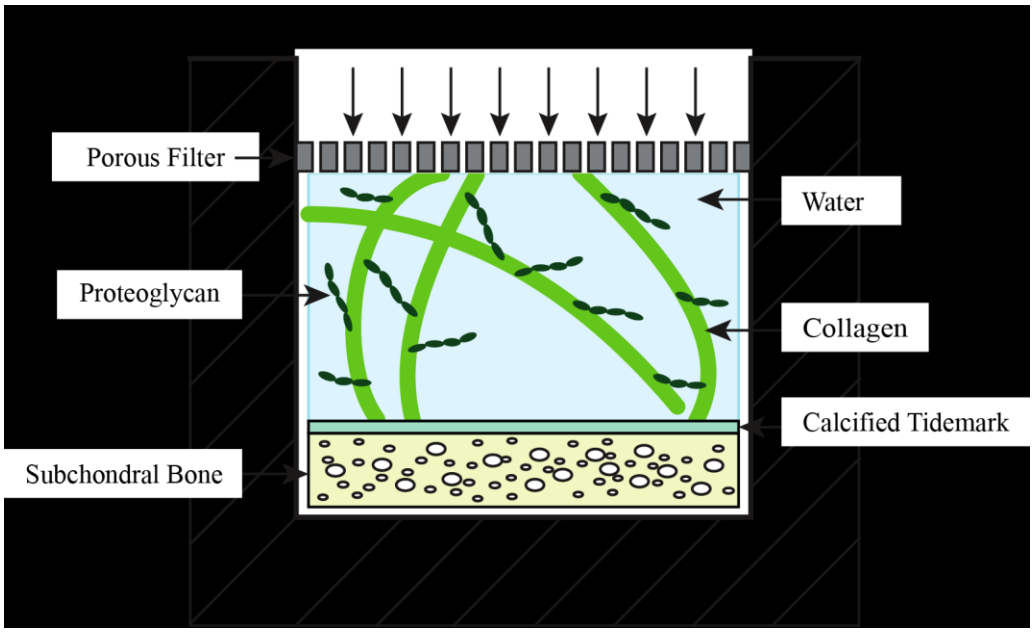

Figure 18: Schematic of Confined Compression Test (Adapted from Mow et al., 1984).

The existing rig consists of an optional temperature-regulated fluid chamber, a stage for the sample, a loading column, a LVDT, a hanging deadweight and a mechanism to transfer the deadweight to the loading column. The unconfined setup could not accommodate the confined compression creep test because the sample would be completely unconstrained on the stage.

The existing setup was modified so that the loading column was removed from the system and a fixture containing the 6.35 mm confining chamber was designed and fabricated from aluminum (Fig. 19). The fixture rests on the stage of the original setup. A revised loading column was also produced (Fig 19). The loading column was designed to allow the LVDT to sit constrained within the column. Additionally, it was designed to minimize the mass of the column. The column moves freely in the axial direction and is constrained in the radial direction.

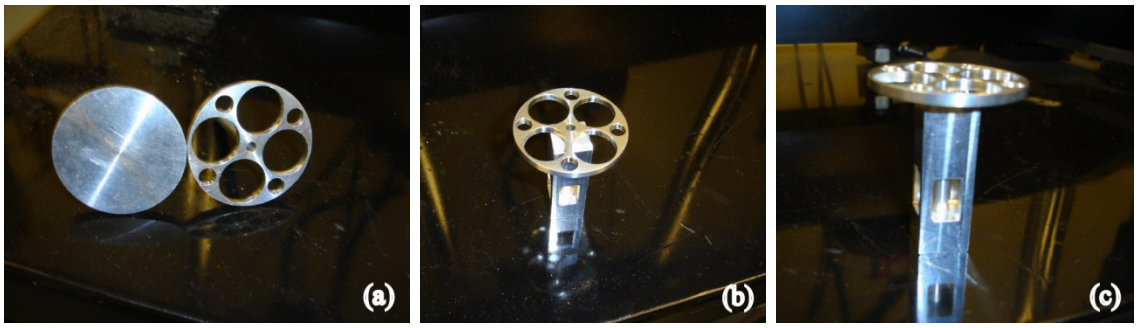

Figure 19: Aluminum fixtures. a) Weight-minimized loading column. b) and c) Loading column inserted into fixture containing the confining chamber.

The test requires that fluid flow freely from the sample as it is compressed and deformed. As a result of the confining chamber, fluid is radially constrained; therefore it must exude axially from the sample. Because the loading column is necessarily in contact with the specimen, it must be porous and allow fluid to flow freely through it. For a valid test, no hydraulic pressure is allowed to build due to the loading platen. As a result, a rigid, porous filter of 75-80% porosity is manufactured with a diameter of 6.35 mm. The filter is affixed to the loading column with adhesive tape. The creep test requires that an applied pressure of 0.1 MPa be applied to the samples, which was accomplished with a 323 g mass placed on the sample (Fig 20).

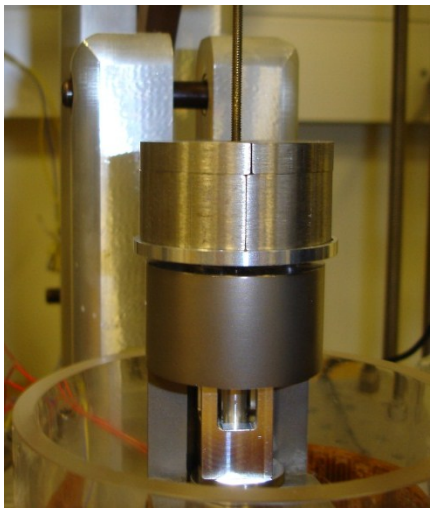

Figure 20: Calibrated weights with loading column in test configuration.

The first step in the procedure was to fully assemble the fixture with the loading column resting in place on the stage. The LVDT is inserted into the recess in the loading column until it reached the bottom of the recess. The loading column and LVDT must move axially as one unit

without resistance. Manually raising and lowering the components several times without observing resistance ensures that the components are oriented correctly. The calibrated weights were placed atop the loading column and the components are again raised and lowered to ensure no resistance to axial motion exists. Once smooth operation is confirmed, the LVDT was zeroed through the controller software.

The next step in the procedure was to place the samples in the confining chambers. The loading column, weights and LVDT must be raised and removed from the confining chamber in order to place the sample inside. The apparatus employed a mechanical arm that was driven by two linear actuators. The components were raised to the upper limit of the actuators with a manual override switch.

The sample was removed from the fluid bath in the plastic container with forceps. The sample is placed in the confining chamber and lightly pressed with the tip of the forceps to ensure that the sample lays flat on the bottom of the chamber. Excess fluid (Deionized water or Krytox® 143AB) from the plastic container was extracted using a pipette and transferred to the confining chamber. The sample was completely covered with fluid and the chamber was filled beyond capacity. This ensured that the sample remained a biphasic mixture of solid matrix and interstitial fluid; as opposed to potentially including a third phase of air if the sample dried out during the test.

The test is designed to smoothly apply the full magnitude of the load within 1 second. The data acquisition software allows for customizable sampling routines that can vary throughout the test. The test is conducted over 3 hours and 5 seconds with an initial sample rate of 20 Hz for the first 5 seconds and then 2 Hz for the remaining 3 hours. The high sample rate during the first 5 seconds is to allow for enough data to monitor the smooth application of the load.

Data acquisition is commenced when the 323 g mass loads the sample. The test runs according to the prescribed schedule. At the conclusion of the creep test, the control arm is automatically raised, thus removing the load from the sample.

The sample is removed from the chamber with forceps. It is examined for any irregularities such as folding or fraying. The sample is returned to the container. The data files are saved for post-processing and analysis according to the Infinitesimal Deformation Biphasic Mixture Model [Mow et al., 1980].

Develop Welded/Woven Materials: Evaluate Methods of Applying Toner

Fabric reinforcement with the introduction of laser welds requires that two polymer surfaces be joined under the conditions of elevated temperature and pressure. The individual surfaces to be joined are the portions of adjacent fibers or yarns that are in contact with each other. As such, an absorbent layer of the Clearweld® coating must be present at the interface between two yarns. Two methods of application have been used in the development of this new class of materials: soak-deposition and direct application. The first method allows for the targeted delivery of Clearweld® to a specific depth and the subsequent, targeted welding at the specified depth. It also

allows for distinct transitions between welded and non-welded regions within the fabric. The direct application method is simpler and ideal for creating welds only at the surface of a fabric.

Soak-Deposition Process

Due to the fact that untreated polymers transmit roughly 85% of the energy incident on the surface, some energy is necessarily absorbed. In order to achieve a weld in a subsurface layer identical to the high quality surface weld, the same energy must be absorbed at the subsurface interfaces as is absorbed at the surface interfaces, or else welding must be integrated with weaving.

To overcome the energy loss attributable to the untreated polymer, the subsurface incident energy must be increased or the density of the absorbent coating must be increased, thereby increasing the percentage of the incident energy that is absorbed.

The transmission of a laser in a semi-crystalline polymer is a function of the depth into the polymer workpiece [Kagan et al., 2002]. This indicates that the laser energy is likely scattered as it progresses through the workpiece [Kagan et al., 2002]. Thus, if the energy intensity decreases as a function of depth within the polymer, then increasing the concentration of the absorbent coating as a function of depth will correct for the loss of intensity. A functional gradient of Clearweld® coating density must be achieved as a function of the fabric thickness (Fig. 20).

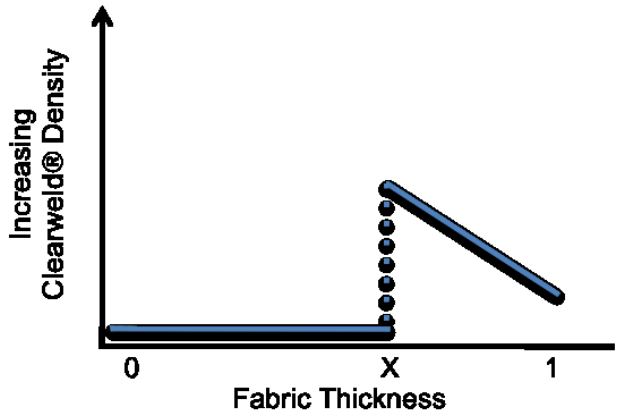

Figure 20: Schematic of Clearweld® density as a function of fabric thickness.

Additionally, it is desirable to be able to target welds at a specific depth without creating welds below that level, a tidemark. The Soak-Deposition process makes use of both the ethanol-based Clearweld® solution and oil that, together, are immiscible (Fig. 21). The density of the oil used must always be significantly higher than the density of ethanol. The oil is used to provide a density barrier within the fabric for the lighter Clearweld® solution to settle on top of. The fabric is placed in a clean, dry receptacle and the oil is added. The oil level is increased until the depth of the desired tidemark is reached. The oil is allowed time to infiltrate the fabric.

The next step in the process is to slowly add the dilute Clearweld® solution on top of the oil layer; taking care not to allow the fluids to mix. Again, the Clearweld® solution is given time to infiltrate the fabric. At this point in the process, the ability to target a specific welding depth exists (Fig. 21).

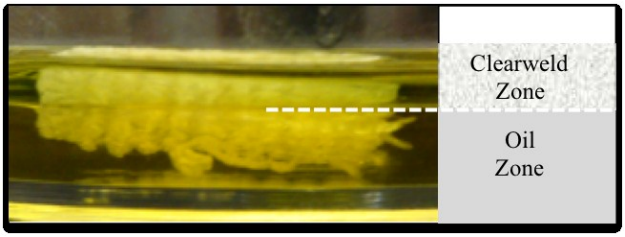

Figure 21: Three-dimensional fabric undergoing Soak-Deposition application of Clearweld® coating.

In order to achieve the gradient of the Clearweld® density, the ethanol solvent is now driven from the solution. The volume of Clearweld® solution is relatively large. As the ethanol begins to evaporate, the uppermost layers of the fabric emerge from the solution. As the Clearweld® solution recedes, the absorbent material is deposited on the fibers with a density dictated by the current concentration of the Clearweld® solution. As the ethanol solvent evaporates, the concentration of the remaining pool necessarily increases. As such, once all ethanol has evaporated, the uppermost layer of the fabric will have the lowest density of the Clearweld® absorbing material. This density will increase with depth up to the tidemark.

The next step in the process is the initial cleaning of the fabric. In this step, a majority of the oil is removed because it is no longer necessary to support the Clearweld® solution. To do this, the fabric is first removed from the remaining oil bath. Next, the fabric is soaked in deionized water to remove additional oil. Passing water through the sample increases the amount of oil removed. The fabric is allowed to dry for several hours. This process does not remove all oil. A sufficient amount is removed, however, to proceed to the welding process.

Direct Application

Several dilutions of the ethanol-based Clearweld® coating are created using reagent quality ethanol. The dilute solutions must be applied to the contact region between adjacent yarns in a controlled manner. In the Direct Application method, a 28 gauge insulin syringe is used to apply the dilute coating. The droplet is then brought into contact with the fabric and disperses evenly due to surface tension.

The coating is distributed over the surface of the fabric sample with a 0.25 cc/cm^2 distribution. To determine the necessary volume of the coating, the area of the top surface of the sample is calculated by measuring its diameter (circular specimens) or its length and width (rectangular specimens).

After the coating is applied, the samples are placed in a vacuum chamber to evaporate the ethanol solvent. The samples remain in the vacuum for one hour. The samples are then brought to atmospheric pressure and any remaining ethanol is allowed to evaporate for another two hours.

Determine Optimal Combination of Weave Constituents and Weld Densities: Mathematical Modeling

Mathematical modeling of the woven materials is important to help design 3D welded-woven fabric with high performance. The software package WiseTex has been used to build a 3D woven geometry (Fig. 22) and to define many material properties. The software has allowed us to perform some quasi-static compression simulations.

From the quasi-static compression simulations, we have been able to determine that the most influential variables are:

1. Number of layers
2. Warp yarn spacing
3. Weft yarn spacing

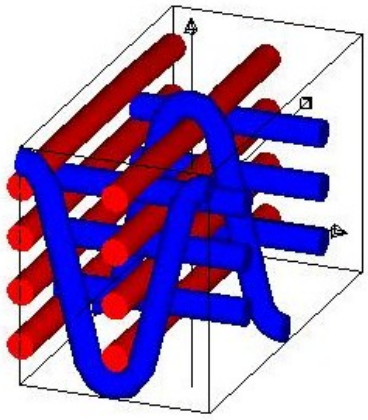

Fig. 22: Geometry of a 3D woven material created within WiseTex®

Within the software package, we have yet to be able to determine the influence of the coefficient of friction between yarns. From Duan et al.[1], we know that this should have an impact. Simulations within WiseTex have not been very robust, so export of the geometry to a commercial finite element package (ANSYS®) has been emphasized. Unfortunately, the files exported by WiseTex® have not imported well to the ANSYS® software. The next step in the modeling is to build a purely geometric model of the fabric to import to ANSYS®. Once the geometry is introduced to ANSYS®, the material properties will be defined, rather than doing so in WiseTex®.

We have been in contact with the WiseTex developer to establish an ability to transfer this data to ABAQUS®. A development version of the software has been provided which may help develop a stand-alone program to convert the files to an ABAQUS® input file.

In addition, a study of the contact between individual yarns in ABAQUS has commenced. A simple sine wave geometry warp yarn is coupled with a straight weft yarn (Fig.23).

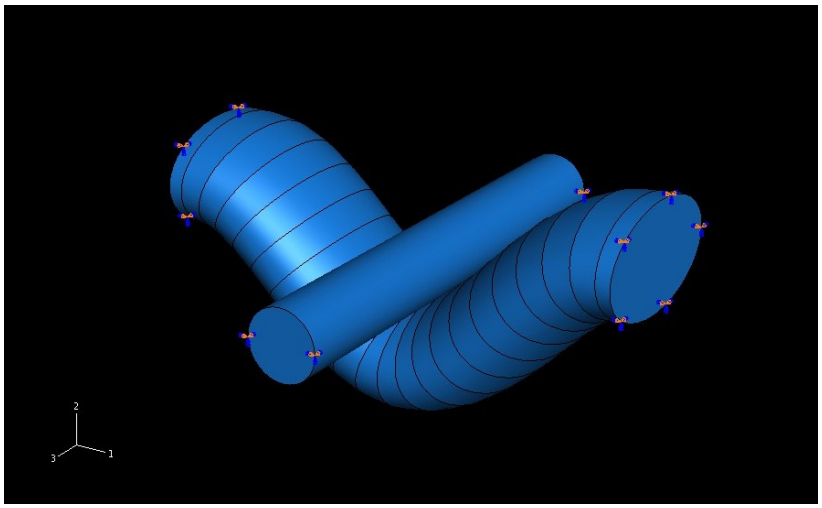

Fig. 23: Yarn contact in ABAQUS®

The yarns have fixed boundary conditions for all degrees of freedom at the end of each yarn. The interaction between each yarn will be studied for a perfectly frictionless and an infinite friction contact. The infinite friction will effectively model a local weld at the yarn-yarn contact. The model is being constructed with linear tetrahedral elements (Fig 24.).

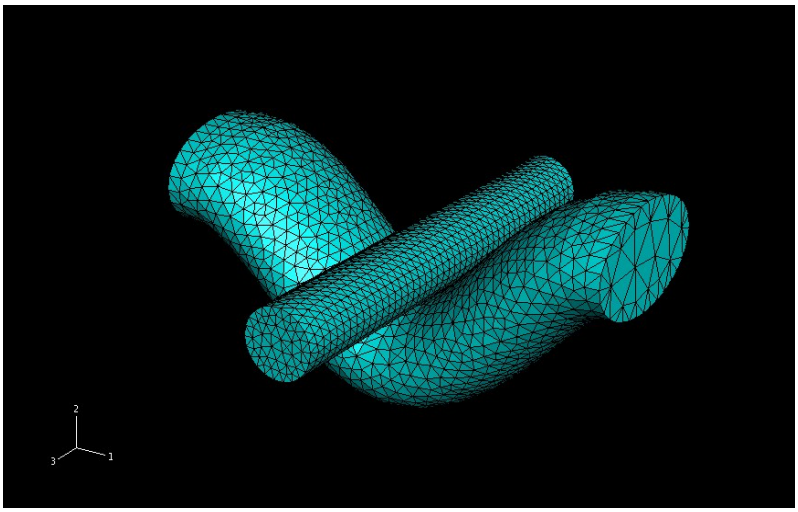

Fig. 24: Tetrahedral meshing of model.

The first deformation and stress outputs (Fig 25) have resulted in a reexamination of the contact model. It has been determined that the yarns are not interacting in a physical way; hence the lack of stress in the warp yarns (Fig. 25).

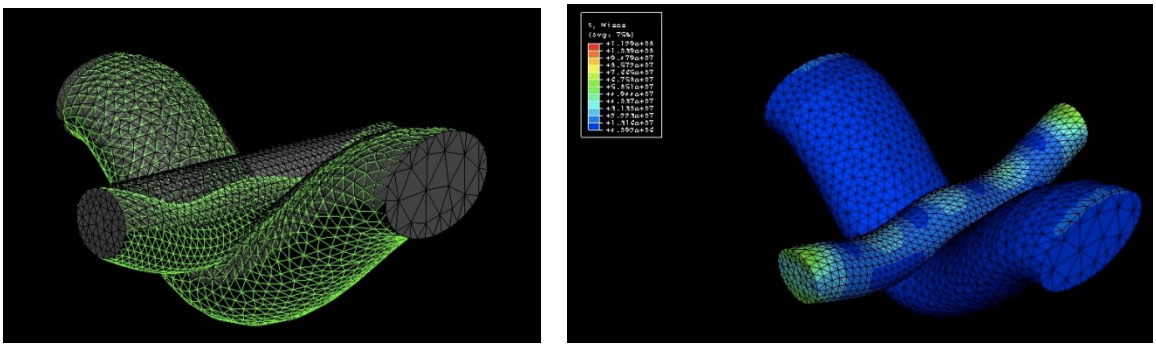

(a) (b)

Fig 25: Deformation (a) and stress output (b)

The contact of the yarns is most important part of this model. In addition to fixing this interaction, customized, refined meshing will likely be called for near the contact region.

Unfortunately, we were never able to develop a conversion algorithm to allow the rapid construction of new finite element models. Without this ability, these computational models were not effective tools.

Determine Optimal Combination of Weave Constituents and Weld Densities: Material Characterization of Wovens and of Welded/Wovens

The Clearweld® coated fabrics are reinforced with uniform surface welds. The fabric coupons are placed on the center of the laser stage. The samples are centered using the visible red targeting laser. A quartz disk is placed on top of the fabric to aid in diffusion between adjacent fibers during welding and to prevent the fabric from warping out of the initial fabric plane (Fig. 26).

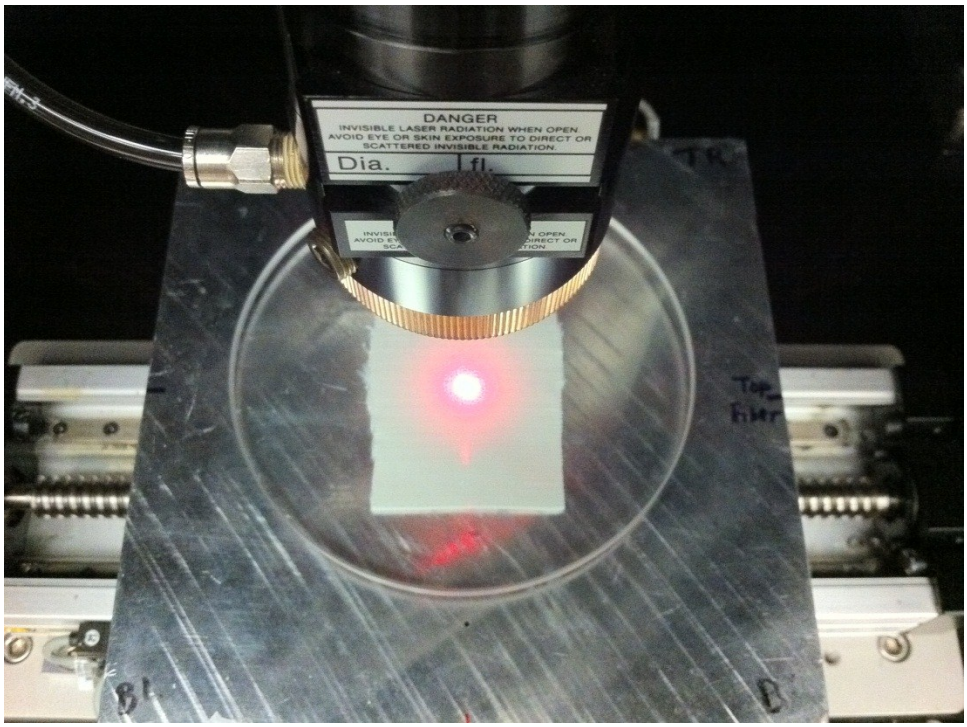

Figure 26: Fabric sample centered with targeting laser and compressed with quartz disk.

All fabric coupons are exposed to an unfocused beam at 140% of the 100 mm focal length of the optics assembly. At this distance from the sample, the beam diameter expands to 2.0 mm. The laser path is programmed to be a series of successive line passes with a line spacing of 1.5 mm. The spacing causes each beam profile to overlap the previous pass of the beam to ensure that a uniform energy distribution is achieved (Fig. 27).

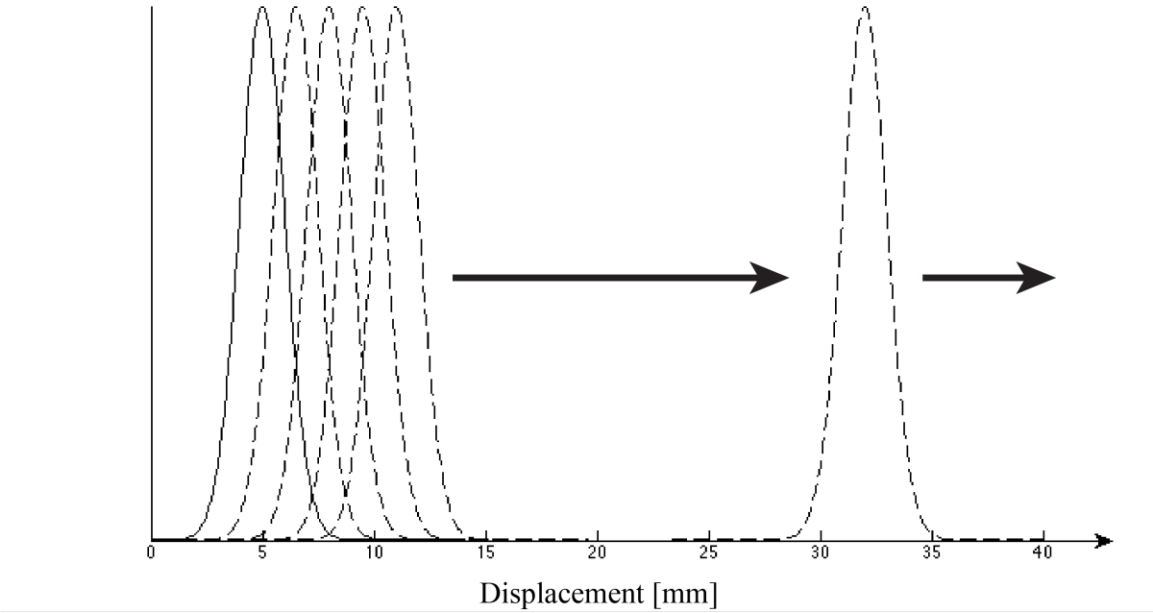

Figure 27: Schematic of overlapping beam profiles.

A laser profile is programmed to pass over the fabric coupon with multiple passes exposing the entire coupon (Fig. 28).

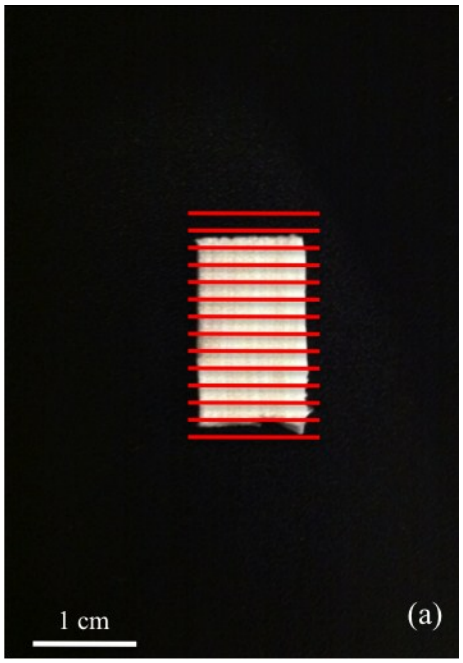

Figure 28: Schematic of laser path overlaid with the 1 cm × 2 cm fabric coupon.

Three parameters are required as inputs to the system in order to manufacture the reinforced fabrics. The parameters are laser power, P_L, laser speed, v, and focal length, L_f. Combining the laser speed and beam diameter, D_B, allows expression of exposure time, t_e, as:

$$t_e = \frac{D_B(L_f)}{v} \tag{7}$$

The focal length of the fiber affects the beam diameter and can be mapped directly to determine beam diameter, D_B.

The three parameters of laser power, exposure time and beam diameter can be converted to one parameter, applied energy, E_A. With the assumption of a Gaussian profile for the beam profile, the applied energy can be calculated over the entire region covered by the beam [Becker and Potente, 2002] as

$$E_A = \int_{t_e} \int_{A} I(D_B) dA dt \tag{8}$$

The laser's power intensity is a function of beam diameter. More important, though, is the applied energy density, *AED*, of the laser beam

$$AED = \frac{E_A}{A_B} \tag{9}$$

$$A_B = \pi\left(\frac{D_B}{2}\right)^2 \tag{10}$$

where A_B, is the area of the incident beam. In this way, three parameters are easily mapped into one, intuitive parameter. The settings selected for welding each fabric are given in Table 2 along with the resultant applied energy density.

TABLE 2

LASER PARAMETERS AND APPLIED ENERGY

Fabric	Power [W]	Speed [mm/s]	Applied Energy [J]	Applied Energy Density [J/mm^2]
SN 3725	10	10	2.0	0.63
SN 3726	10	10	2.0	0.63
SN 3786	10	10	2.0	0.63
SN 3787	7.5	10	1.5	0.47

The parameters are programmed into the integrated controller software as part of the profile paths for each fabric type. Once the end of the welding path is reached, the disk is removed from the top of the fabric and the sample is removed from the laser enclosure.

Each sample is viewed through a microscope at four times magnification (Fig 29). The fabrics are inspected to ensure that welding has taken place on the surface of the fabric. Additionally, the surface is examined for degradation to the surface layer. The examination consists of tracking individual yarns for the length of the fabric and ensuring that there are no significant discontinuities. Using a digital camera, photographs of each welded sample are captured and stored for future analysis. It is noted that some of the polymer fibers are visibly degraded. The welding procedure is completed.

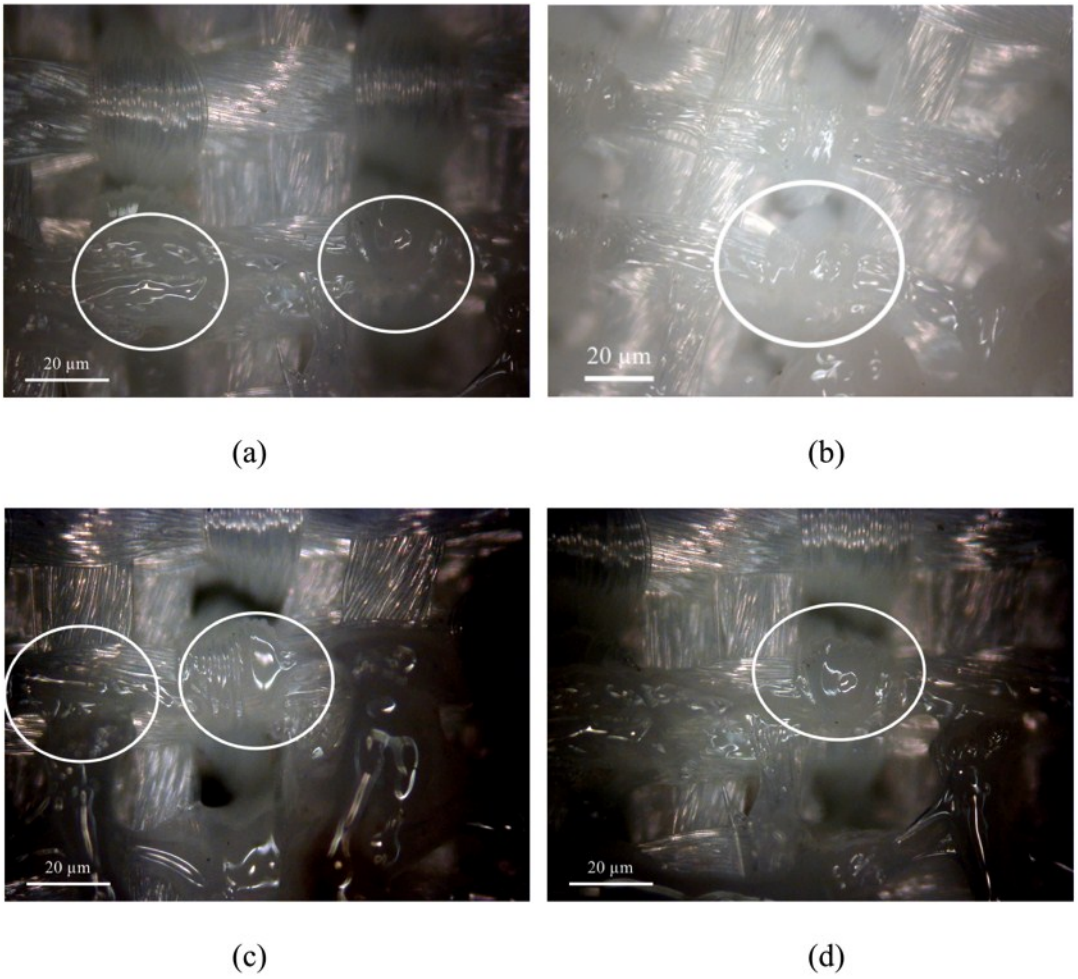

Figure 29: a–d) Successful surface welding of orthogonal PET fabrics. The circular regions indicate high quality welds between contacting yarns.

The welded materials were tested in confined compression and compared to the results for non-welded fabrics. Displacement data for the LVDT was taken over the three hour and five second duration of the test. The raw LVDT data exhibited considerable noise around the true displacement value (Fig. 30).

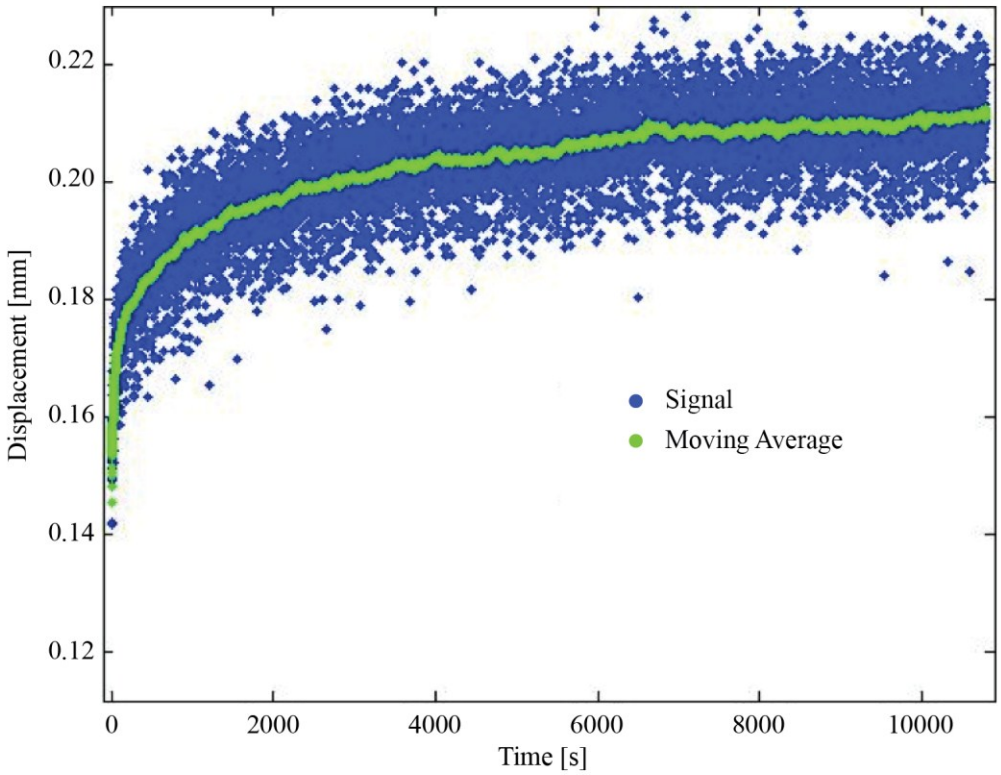

Figure 30: LVDT signal for one confined compression creep test.

Though the data contains significant signal noise, it clearly exhibits viscoelastic behavior. The tests do not include a stress relaxation period and, thus, yield a curve that is monotonic in nature. Filtering the data will remove the noise in the signal. Because the signal is monotonic, a simple moving average filtering scheme can be implemented without the concern that any particular events in the data will be lost.

A moving average filter is implemented. The filtered curve retains some of the nuances of the original signal, but drastically reduces the signal to noise ratio (Fig. 30). The filtered signal allows for a more robust fit to the Infinitesimal Deformation Biphasic Mixture Model.

The filtered data is fit to the model using the Matlab Curve Fit Toolbox. A 1,000-term expansion of the model is implemented. The aggregate modulus, H_A, and the hydraulic permeability, k, are returned from the nonlinear regression, along with 95% confidence intervals (Fig. 31).

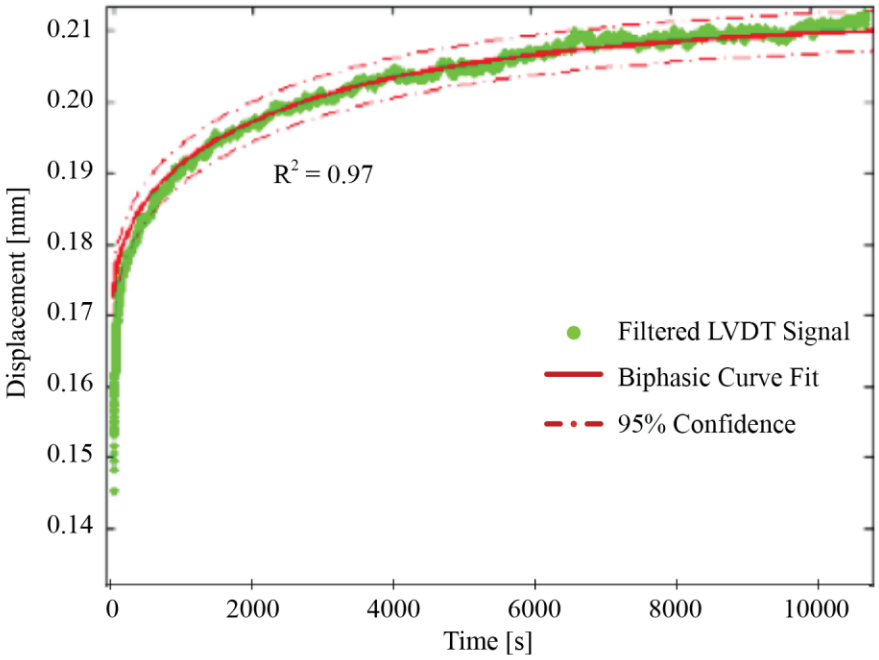

Figure 31: Filtered LVDT signal with biphasic curve fit.

The curve fitting routine was performed iteratively to find the best R^2 fit. The solutions determined are local minima and are not guaranteed to be the best fit of the model.

The aggregate moduli of the virgin fabrics are presented in Fig. 32 and within the published range of articular cartilage: 0.1 – 2.0 MPa. The densest fabric (SN 3786) exhibits the highest aggregate modulus of the fabrics tested: 1.0 MPa when paired with deionized water and 1.29 MPa with Krytox 143AB. This is the only statistically significant change attributed to the interstitial fluid among the four fabrics tested. Due to Darcy effects, the higher viscosity fluid coupled with the relatively smaller voids between the fibers of the fabric explains the higher modulus values when paired with the far more viscous Krytox 143AB.

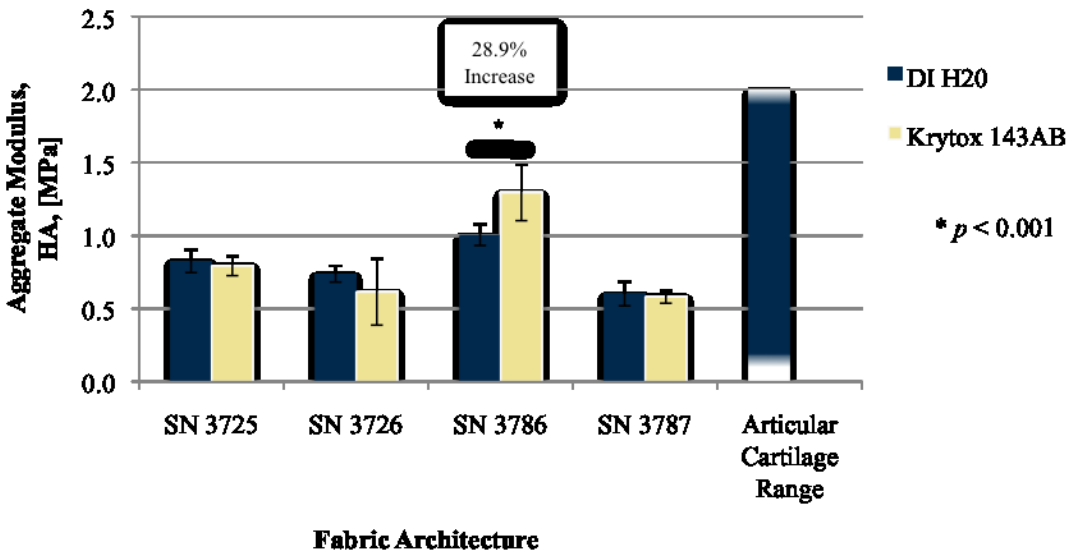

Figure 32: Aggregate modulus of virgin fabrics in deionized water and Krytox® 143AB with one-way ANOVA statistical significance. Also shown is the range of published values for articular cartilage (Mow, 2002).

The permeability of each fabric was recorded for each group of tests (Fig.33). There is no statistically significant effect of the type of fluid used on the permeability of a particular fabric. The wide variation of permeability is due to the model's sensitivity to this parameter and due to the solutions of the curve fit being at local minima and not guaranteed to be at the global minimum.

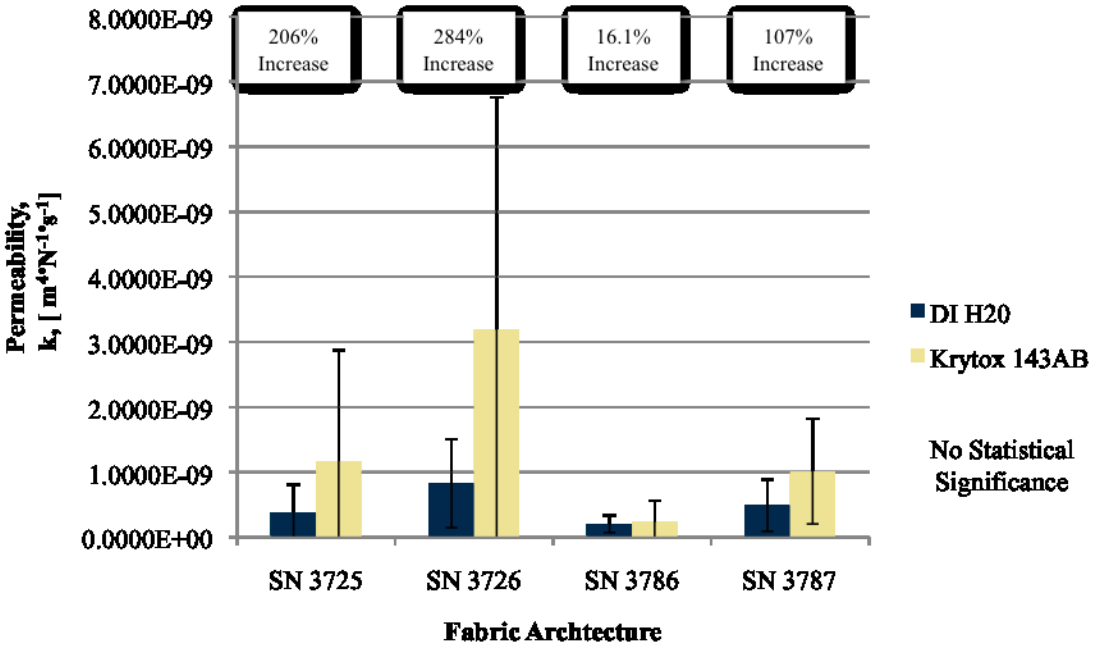

Figure 33: Permeability of virgin fabrics in deionized water and Krytox® 143AB. There is no statistical significance in the change of the mean value within each fabric.

The permeability values, k, of each virgin fabric are given in Table 2 along with the numerical values for the aggregate modulus, H_A. The permeability values for all fabric types paired with either fluid are at least five orders of magnitude larger than the published values for articular cartilage [Athanasiou et al., 1991, Setton et al., 1993]. The difference is attributable to the structural differences between articular cartilage and three-dimensional fabrics.

TABLE 3

AGGREGATE MODULUS AND PERMEABILITY

RESULTS OF VIRGIN FABRICS

	DI H_20		**Krytox 143 AB**	
Fabric Architecture	H_A **[MPa]**	k **[m^4/N·s]**	H_A **[MPa]**	k **[m^4/N·s]**
SN 3725	0.872 ± 0.079	3.83E-10 ± 4.23E-10	0.793 ± 0.067	1.17E-9 ± 1.71E-9
SN 3726	0.737 ± 0.055	8.30E-10 ± 6.80E-10	0.614 ± 0.226	3.19E-9 ± 3.57E-9
SN 3786	1.00 ± 0.072	2.02E-10 ± 1.29E-10	1.29 ± 0.192	2.35E-10 ± 3.23E-10
SN 3787	0.601 ± 0.081	4.90E-10 ± 3.98E-10	0.581 ± 0.043	1.01E-9 ± 8.07E-10

The results for the aggregate modulus of each fabric and fluid pairing are consistent and repeatable, as indicated by the standard deviations. In addition to the significant difference between the permeability values of the fabrics and articular cartilage, the fabric values have high variability within the same architecture (Table 3). The variability may be due to the fact that the curve fitting routine finds local minima of residuals as opposed to a global minimum.

The welded fabric data was analyzed in the same manner as the virgin fabric data. The aggregate modulus, H_A, for all four fabrics was shown to increase due only to surface welding. The aggregate modulus of the welded fabrics increased between 29.8% and 64.2% across the four fabric types (Fig. 34). The increase between the virgin and welded versions of each fabric architecture is statistically significant.

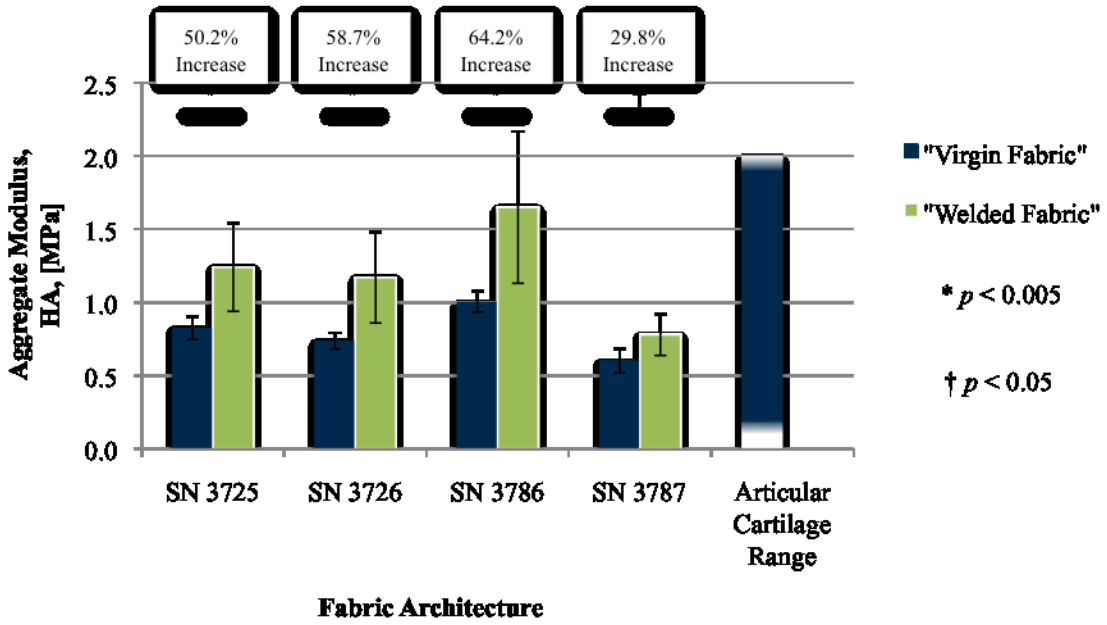

Figure 34: Aggregate modulus of virgin and welded fabrics in deionized water with one-way ANOVA statistical significance. Range of published values for articular cartilage is also shown [Mow, 2002].

The aggregate modulus of each of the four welded fabrics is within the range of published values of articular cartilage.

The permeability of each fabric type decreases drastically with the weld-reinforced surface (Fig 35). The permeability values of each virgin fabric are given in Table 4 along with the numerical values for the aggregate modulus.

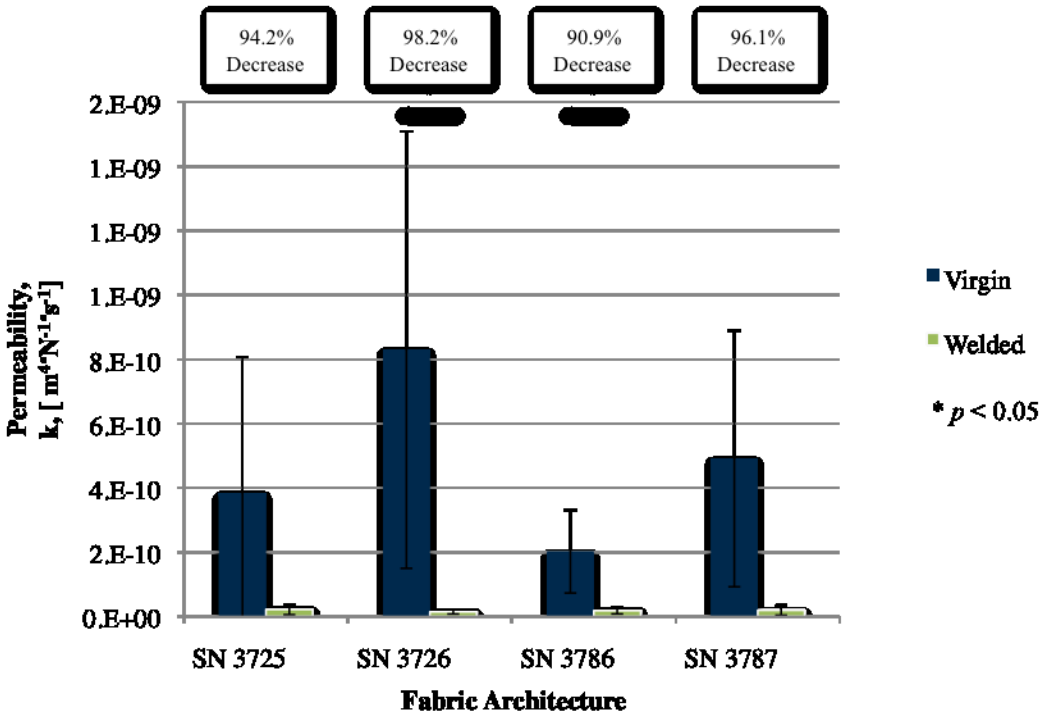

Figure 35: Permeability of virgin and welded fabrics in deionized water and with one-way ANOVA statistical significance.

TABLE 4

AGGREGATE MODULUS AND PERMEABILITY

RESULTS OF WELDED FABRICS

Fabric Architecture	H_A [MPa]	k [$m^4/N \cdot s$]
SN 3725	1.24 ± 0.300	2.21E-11 ± 1.64E-11
SN 3726	1.17 ± 0.310	1.46E-11 ± 6.77E-12
SN 3786	1.65 ± 0.518	1.84E-11 ± 1.04E-11
SN 3787	0.780 ± 0.142	1.94E-11 ± 1.53E-11

Welding causes the surface fibers and yarns to bond with the adjacent fibers and yarns. The welds prevent the yarns from displacing laterally into the fabric voids. The decreased relative motion limits fluid flow due to Biot's Consolidation. As a result, the permeability of a welded fabric is lower than an untreated version of the same fabric architecture.

Determine Optimal Combination of Weave Constituents and Weld Densities Design of Multi-weave Implants, w/ Welded-Woven Sections

The effect of weld densities could not be achieved due to the uniform application of the Clearweld coating to the fabrics. In order to effectively disperse welds with varying densities in the plane of the fabric, selective application of the Clearweld system, in the plane of the fabric, must be achieved. This would be better achieved if the fabric was woven with yarns that were impregnated with a Clearweld resin during yarn manufacturing. This treatment of yarns was outside the scope and budget of the project.

Demonstrate that the Woven Composites Maintain a Long Life: Design Specimens for Wear Testing

Samples of three-dimensional woven materials were obtained from Secant Medical (Perkasie, PA) for pin-on-disk accelerated life testing. Four three-dimensional fabrics have been chosen for wear testing. All fabrics were orthogonal polyester (PET) weaves with single pairs of end stitching. An OrthoPOD (AMTI, Watertown, MA) six station pin-on-disk testing machine is used for the experiments.

Circular samples were produced from a large strip of fabric using a punch and mallet. A 35 mm hole punch was used to cut the majority of the sample and a sharp razor blade was used to carefully sever the remaining intact fibers. To prevent fraying, a controlled flame was used to sear the fabric edges.

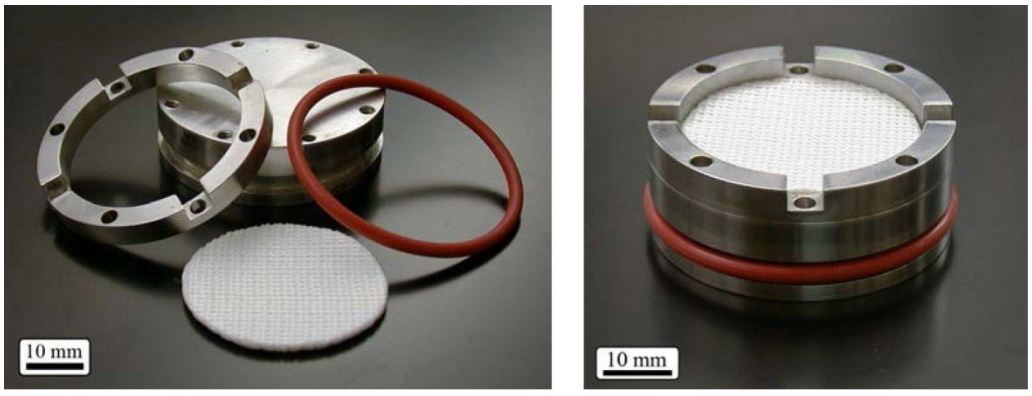

Figure 36 (a) From left to right, the retaining ring, metal puck, fabric smaple and O-Ring used for Orthopod testing; (b) the assembled fixture.

Fixtures previously used to test two-dimensional woven materials [Jones 2010] have been modified to accommodate three-dimensional fabrics. The assembly consists of a solid metal puck

used as a base with a shallow retaining ring screwed onto the surface, as illustrated in Fig. 36. High performance spray adhesive (Loctite, Westlake, OH) was used to adhere the fabric samples to the metal pucks. This method provides enough resistance to prevent sliding and bunching during testing. A stencil was used to ensure the adhesive spray was confined to the circle formed by the retaining ring and the adhesive was allowed to dry to tack before the fabric samples were secured, per the manufacturer's instructions. Small amounts of overspray were inevitable but were observed to be unchanged at the end of testing and did not interfere with the lubricant or wear of the samples. Fabrics were aligned preferentially so that the direction of lowest friction aligned with the path of the pin. Light pressure was applied and the adhesive was allowed to dry overnight.

Demonstrate that the Woven Composites Maintain a Long Life: Wear Testing 3D Woven and Welded/Woven Materials

Welded test coupons with dimensions of 4.5 cm × 7 cm were cut from the 7 cm strip of fabric manufactured by Secant Medical®. The fabric coupons were cleaned ultrasonically in a 30% ethanol, 70% deionized water bath for 10 min. The coupons were removed from the bath and placed in a vacuum chamber for one hour and then removed.

Next, a dilute 30:1, ethanol:Clearweld®, ethanol-based Clearweld® Material System was applied to the fabrics. The solution was applied with a dropper with an application density of 0.20 mL/cm^2 for all four fabric architectures.

After the dilute Clearweld® solution was added to the fabric coupons, they were placed in a vacuum chamber for one hour. The coupons were removed and allowed to vent in open air for an additional hour to remove the ethanol carrier.

As before, the coupons were centered on the laser stage compressed by a quartz disc, and then welded. All fabrics were exposed to an unfocused beam at 140% of the 100 mm focal length, which yields a 2 mm beam diameter at the fabric surface. A laser profile was created with an overlapping, 1.5 mm beam spacing (Fig. 37). The selected laser parameters were programmed as part of the profile (Table 5).

Figure 37: Schematic of laser path overlaid with the 4.5 cm × 7 cm fabric coupon.

TABLE 5

LASER PARAMETERS AND APPLIED ENERGY

Fabric	**Power [W]**	**Speed [mm/s]**	**Applied Energy [J]**	**Applied Energy Fluence [J/mm^2]**
SN 3786	10	10	2.0	0.63
SN 3787	7.5	10	1.5	0.47
SN 3796	5	12.5	0.8	0.25
SN 3825	7.5	10	1.5	0.47

The samples were welded and examined in a microscope to visually and qualitatively assess the weld quality. It was noted that neither of the satin-topped fabrics appeared to weld as uniformly as the orthogonal fabrics (Fig. 38).

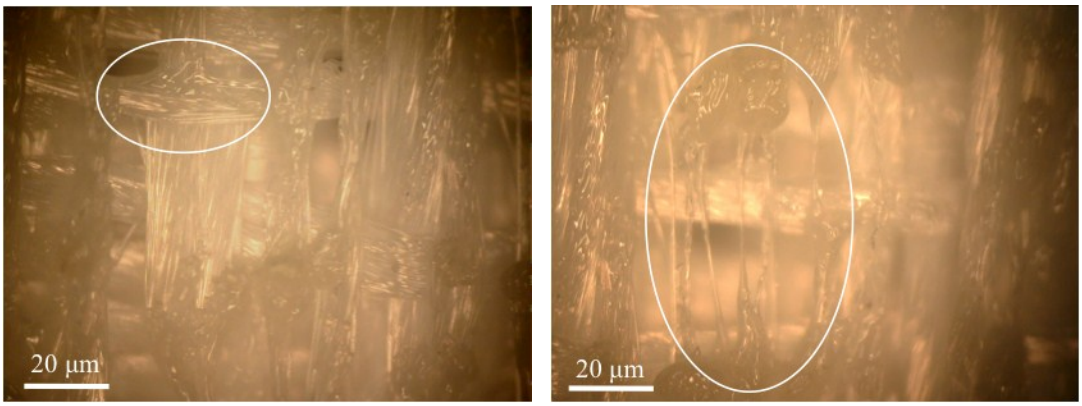

(a) (b)

Figure 38: a) Successful welding of satin PET fabrics. b) Degradation of satin PET fabrics.

Samples were punched from the previously prepared welded coupons of each fabric type using a 35 mm diameter, circular hole punch and a scalpel as needed (Fig. 39). The fibrous edge of the fabric sample was exposed to an open flame to seal it and prevent any damage (fraying of fiber pullout) from initiating at this location.

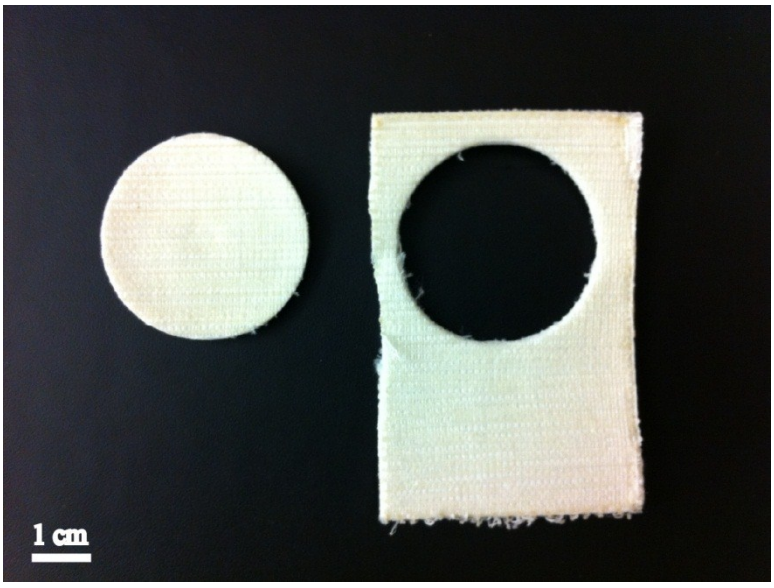

Figure 39: Sample produced from a welded fabric coupon (SN 3786 shown).

Samples from the welded coupon were scanned using a SCANCO Medical (Brüttisellen, Switzerland) μCT 80. 3D renderings were created to confirm uniform surface welding as well as the preservation of the subsurface fabric (Fig. 40).

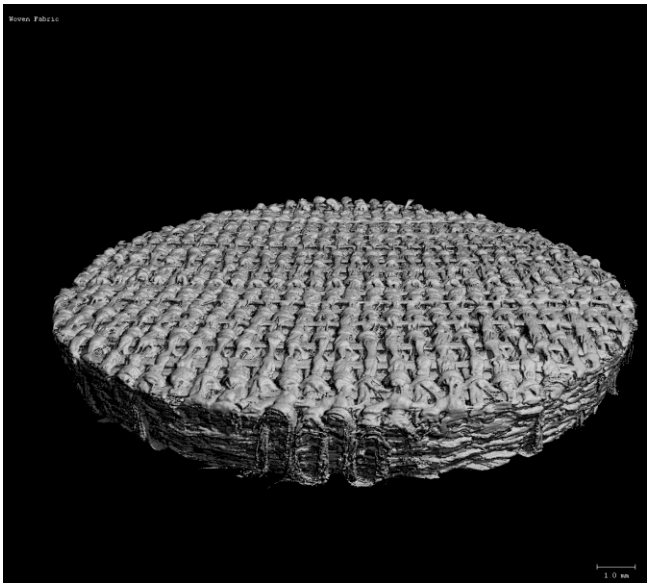

(a)

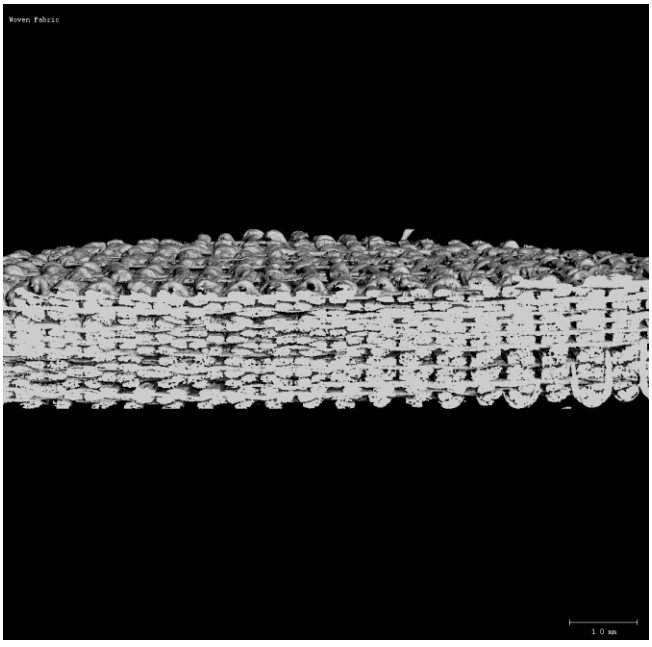

(b)

Figure 40: 3D MicroCT rendering of successful surface welding and of SN 3786

The samples were soaked in 99.5% A.C.S. reagent quality ethanol for 10 minutes and gently agitated to remove the Clearweld® coating. The samples were then sonicated for 10 minutes in a mixture of 30% ethanol and 70% deionized water. Following the sonicating cycles, the samples were rinsed with deionized water. The samples were then placed in a vacuum oven at 40ºC and between 75 and 85% vacuum for 10 hours. The elevated temperature aids in the evaporation of ethanol and deionized water, but is significantly lower than the glass transition temperature of PET, 70ºC [Alves *et al*, 2002] and the melting temperature of PET and UHMWPE, 250ºC and 145ºC, respectively [Rodriguez *et al*, 2003]. Thus, there was no change to the polymer structure during drying. The samples were removed at the end of the 10 hour drying period.

Four samples of each fabric were created; one control sample and three test samples. The samples were weighed three times in rotation to determine the initial mass of each fabric.

The samples were mounted to fixtures consisting of a puck, retaining ring and O-ring (Fig. 41). The fixtures were designed for studies on two-dimensional fabrics [Jones, 2010] and revised for the previous study of three-dimensional fabrics [Giordano, 2011].

Figure 41: Fixtures used in pin-on-disc wear tests.

All three components, as well as the hex head bolts used to mount the retaining ring to the puck were cleaned with 91% isopropyl alcohol.

The assembly of the sample and fixture requires that the sample be affixed to the puck. Spray Adhesive High Performance produced by Loctite® (Westlake, OH) was used to adhere the fabric to the puck. A 35 mm stencil was placed on the puck, covering the holes of the bolt circle. The adhesive was applied and allowed to dry to tack for 7 min., in accordance with the manufacturer's directions. The stencil was removed and the retaining ring is installed while the adhesive dries to tack.

The fabrics were placed on the pucks with the direction of the welding path perpendicular to the stance phase of the loading path. Light, uniform pressure was applied over the surface of the fabric to join the puck and the fabric sample. The complete assemblies were allowed to cure overnight (Fig. 42).

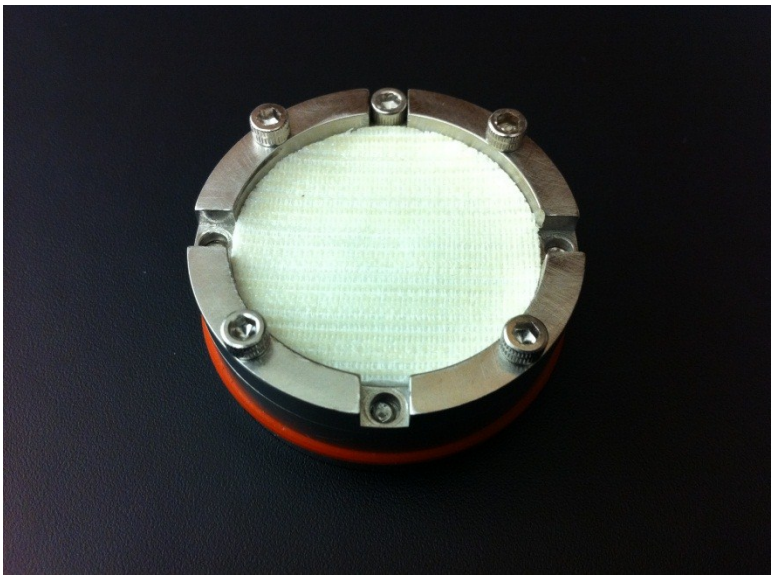

Figure 42: Complete fabric-puck assemblies.

Pin-On-Disc Test Procedure

An Ortho-POD, six station, multi-directional pin-on-disc machine manufactured by Advanced Mechanical Technology, Inc. (Watertown, MA) was used for the wear study. A load-velocity profile was previously developed to mimic the human gait cycle (Fig. 43) [Giordano, 2011]. Human gait can be partitioned into two main phases: stance and swing [Hesse and Uhlenbrock, 2000] among many others. The stance phase comprises approximately 62% of the cycle; swing phase the other 38% [Ayyappa, 1997; Kadaba et al., 1989 and Giordano, 2011]. Giordano designed the profile to account for each phase with their respective loads and sliding velocities.

The profile was comprised of two phases. The first stage was designed to mimic the stance phase of human gait with a lower velocity and higher load. The second stage was designed to mimic the swing phase of human gait with a higher velocity and lower load.

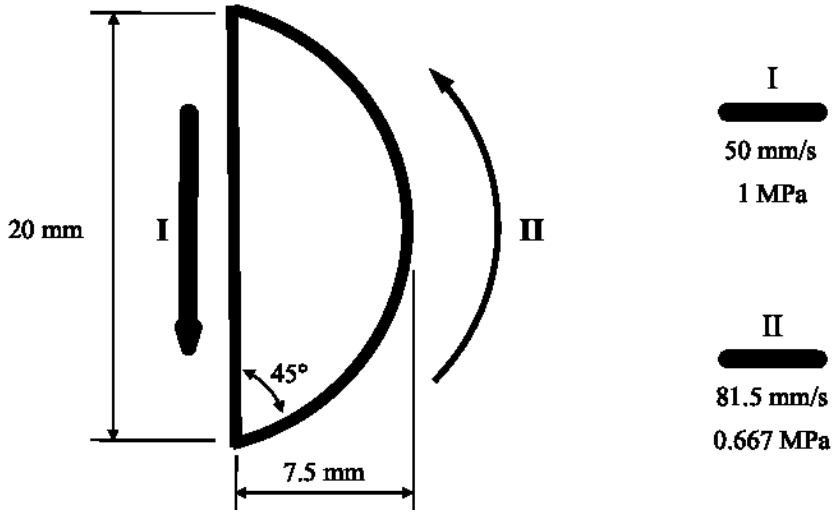

Figure 43: One cycle of the human gait mimicking load-velocity profile (Giordano, 2011).

The profile was designed to execute one cycle every 0.785 seconds (1.27 Hz) [Giordano, 2011]. In practice, it was measured that the controller software executes one cycle approximately every 0.501 seconds (2 Hz). This can be attributed to the limitations of the controller governing the motors of the disc and pins of the Ortho-POD. This was deemed acceptable as multiple studies have cited knee simulator tests of tibial inserts using frequencies of 1-2 Hz [Muratoglu et al., 2004; Muratoglu et al., 2007; Tsukamoto et al., 2006; McEwen et al., 2005].

The tribopair consists of the polymer fabric samples and a cobalt chrome pin with a 12.7 mm tip radius. The pins were weighed three times in rotation prior to each testing interval. The surface roughness of each pin was measured at each testing interval using a NewView 7000 Series Optical Profiler from Zygo Corporation (Middlefield, CT).

Prior to each test interval, the fabric assemblies and control samples underwent a cleaning procedure modified from ASTM F2025-06. The samples were rinsed in a stream of deionized water. Next they were placed upside down in a plastic container, which was then filled with deionized water. The containers were sealed and placed in an ultrasonic bath for 5 min. The samples were removed and again rinsed with a stream of deionized water. The samples were returned to the plastic containers, right-side up, filled with deionized water and sealed. The samples were sonicated for 15 min. Again, the samples were rinsed in a stream of deionized water. The samples were then exposed to a jet of lab air to remove the majority of water and then were placed in a vacuum oven at 40ºC and between 75 and 85% vacuum for a minimum of 10 hours.

The samples were then removed and allowed to cool to room temperature for one hour. The samples are weighed three times in rotation and recorded. The dry samples were photographed at each wear test interval.

The fabric assemblies are fitted with the rubber O-rings and a plastic fluid containment ring. The assemblies are filled with 20 mL of deionized water and allowed to soak for one hour. The control samples are placed in a plastic container and also filled with 20 mL of deionized water and allowed to soak for one hour. This soak period is intended to allow water to infiltrate the fabrics and displace the interstitial air of the dry fabric.

The assemblies were installed on the Ortho-POD six station disc and lowered into place on the Ortho-POD chassis (Fig 44). The pins were lowered and clamped in place and the load cells were balanced. Next, the number of cycles for the interval was programmed using the Ortho-POD's controller software. The test commenced and was allowed to run to completion.

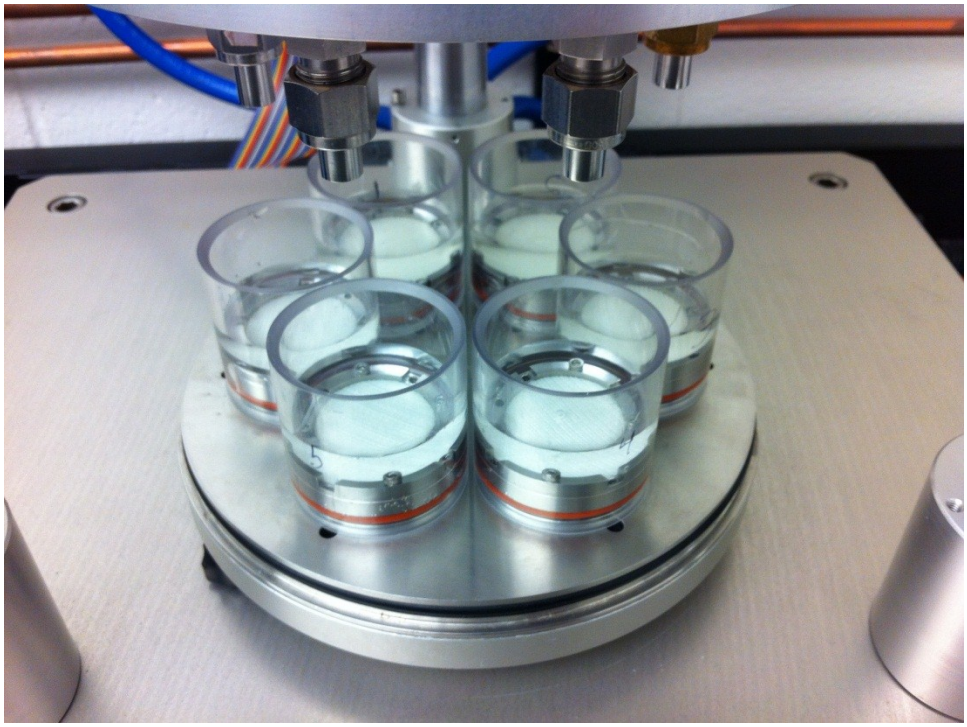

Figure 44: Fabric assemblies installed in Ortho-POD.

One control sample of each fabric type tested was placed under static loading in 20 mL of deionized water for the entire duration of the pin-on-disc wear test (Fig. 45).

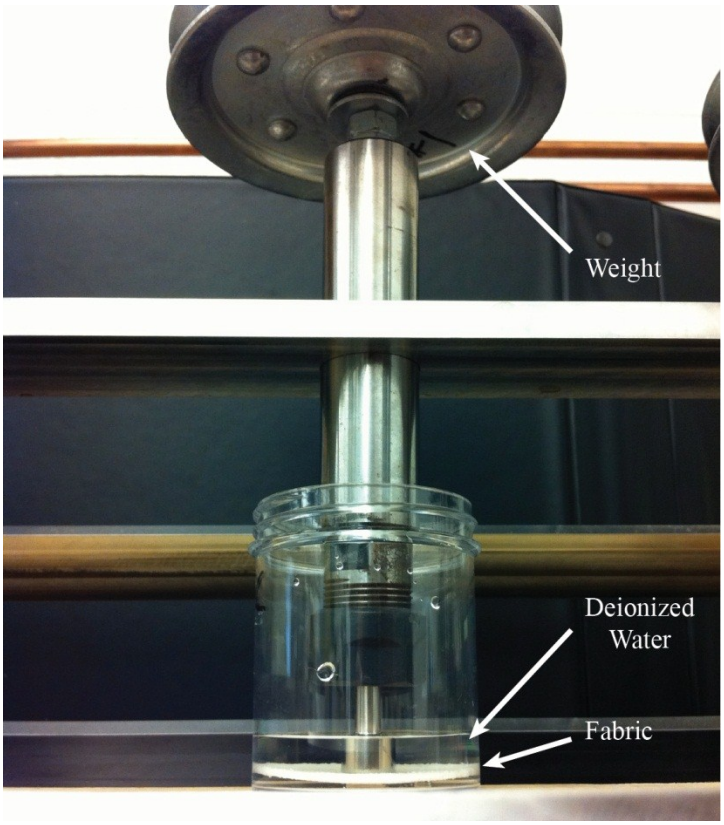

Figure 45: Control samples in a static load-soak configuration.

The gravimetric data from the load-soak control samples was used to account for hygroscopic effects.

Upon the completion of each interval, the lubricating bath of deionized water and wear debris was collected. Note that not all debris can be collected due to the design of the fixtures and fluid containment rings. The plastic retaining ring and O-rings were removed for cleaning. The cleaning procedure detailed above is conducted between each test interval.

The number of cycles per interval was initially low to give resolution to the gravimetric data in order to identify any run-in that may occur. The intervals then increased in duration until fabric failure.

Gravimetric Analysis

One control and three samples (n =3) of each fabric were used in the wear study. The following procedure for gravimetric analysis was conducted according to ASTM F2025-06. The mass of each fabric was recorded before mounting to the puck assemblies as C_{init} and $M_{init,j}$. j is the fabric index where j = 1, 2, …, n. The samples were then adhered to the puck assembly.

The initial mass of the control, C_0, and three samples, $M_{0,j}$, were recorded. After every i^{th} interval to a total of N intervals, the mass of the control and samples are recorded as C_i and $M_{i,j}$

respectively. The cumulative number of cycles completed at the conclusion of a particular interval is recorded as S_i.

After each interval, the average mass change of the set of fabric samples is calculated as

$$M_i = \frac{1}{n}\sum_{j=1}^{n}\left(M_{i,j} - M_{i-1,j}\right) \tag{11}$$

The wear over a given interval can be quite small and may be masked by the overall fluid sorption of the polymer during that interval. As such, the gravimetric wear, W_i, must take into account this hygroscopic effect. The gravimetric wear after each interval is calculated as

$$W_i = M_i + \left(C_i - C_{i-1}\right) \tag{12}$$

The wear rate for an individual interval is calculated as

$$\dot{W}_i = \frac{W_i - W_{i-1}}{S_i - S_{i-1}} \tag{13}$$

where S_i is the number of cycles elapsed at the end of the i^{th} interval. The wear rate over any individual interval can be determined by adjusting the interval index, i, in Eq. (7).

Results

Gravimetric analysis was conducted after each interval. The results from each interval were used to determine the duration of the next interval. As the tests progressed, the intervals were generally increased in duration.

The initial conditions of each fabric were documented quantitatively as well as with photographs for referencing throughout the tests. In addition to evaluating the gravimetric wear data, it is important to monitor the quality of the bearing surface. Throughout the tests, several samples developed large tufts of fabric near the end of life, which did not immediately detach. The gravimetric analysis alone does not reveal this severe damage as it does not release and contribute to mass change.

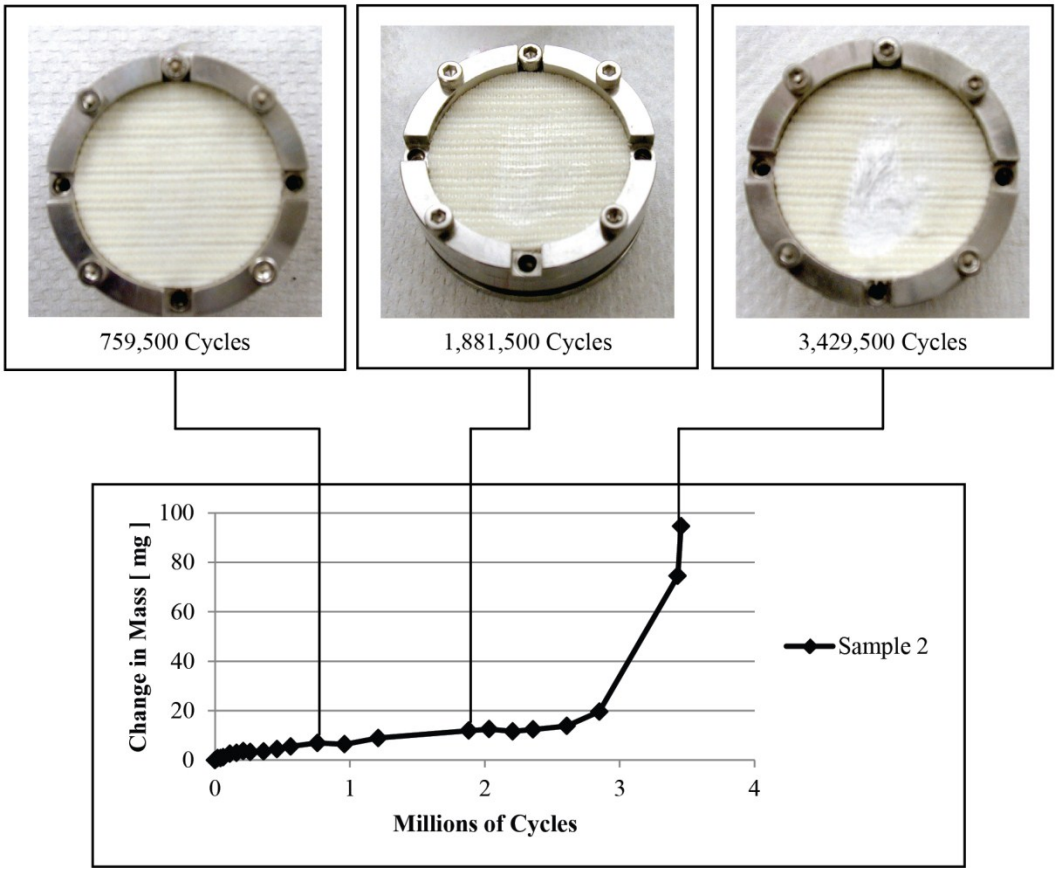

Figure 46: The wear history and evolution of damage of an individual sample of SN 3786 (PET-HD).

The fabric samples were run to failure, which is defined as the cobalt chrome pin wearing through the thickness of the fabric to the metal puck surface. The progression of wear is analyzed in conjunction with visual inspection of the sample (Fig. 46). The welded surface of the high density orthogonal PET fabric (SN 3786) functioned very well as a mating surface to the cobalt chrome pin for over two million cycles. The two earliest photographs of the sample show the development of a shiny, polished imprint of the wear profile. The profile is strikingly visible while the surrounding welded surface had no observable damage or degradation. The welds have served not only as a good bearing surface, but also as an inhibitor for the spread of damage away from the contact region due to fraying or fiber pullout.

As the test progressed past 2.75 million cycles, the wear rate increased drastically. In addition, there was a related change in the appearance of the fabric surface. The welded surface of the fabric was worn so that subsurface, non-welded layers of the fabric sample were exposed. This is evident by the bright white portion of fabric in the photograph of the sample at 3,429,500 cycles (Fig. 46). The fabric began to fray and create tufts of fibrous debris that remained partially attached to the surface. All three welded samples of SN 3787 exhibited similar behavior (Fig. 47).

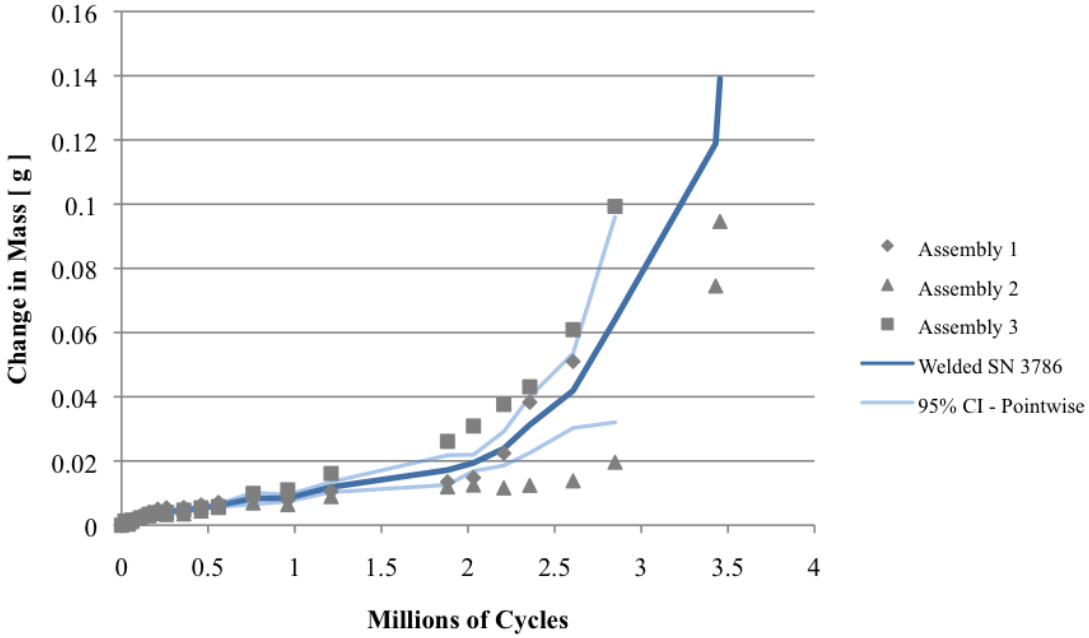

Figure 47: The aggregate wear behavior of SN 3786 (PET-HD) with pointwise 95% confidence intervals.

The low density orthogonal PET fabric (SN 3787) exhibited similar trend to SN 3786 (Fig. 48). The welded surface wore slowly for approximately two million cycles before it was fully removed. The wear profile was again visibly imprinted into the fabric surface. Once the welded surface layer was fully consumed, the fabric deteriorated more rapidly. Again, the tufts of fabric were produced along with significant fraying. Even in the most severe stage of the wear progression, the fabric surrounding the wear profile contact area was preserved quite well. This reinforces the idea that the welded surface isolates damage to a particular region of the fabric.

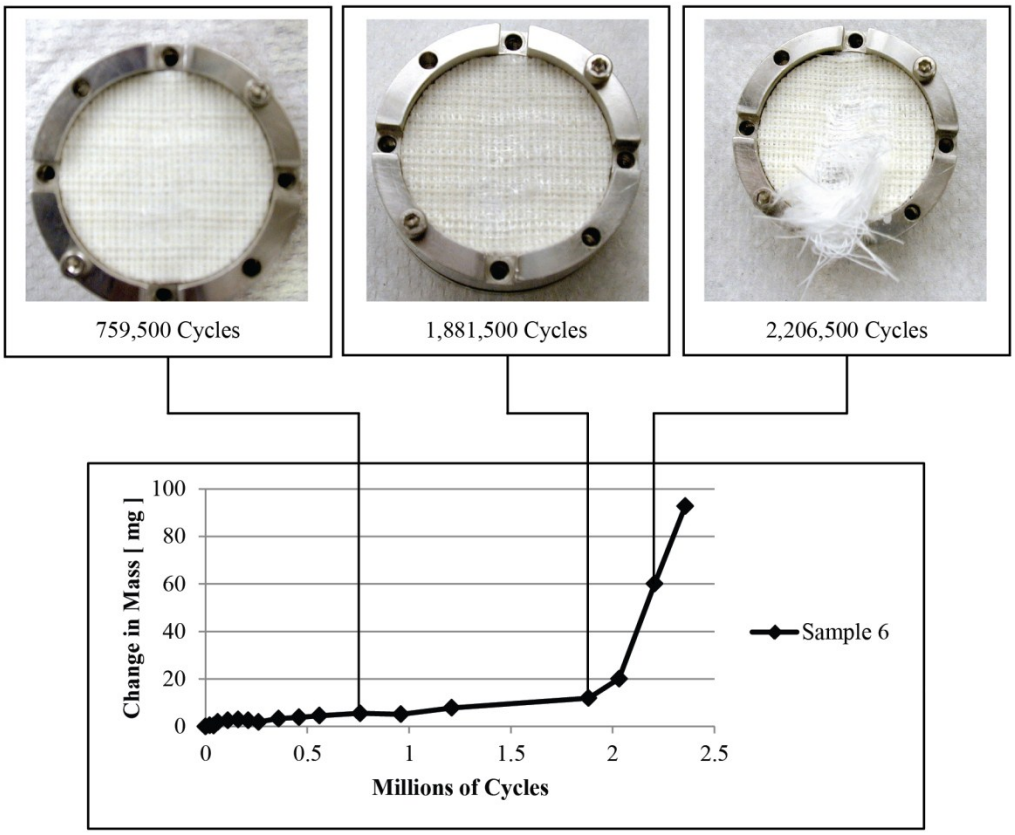

Figure 48: The wear history and evolution of damage of an individual sample of SN 3787 (PET-LD).

The aggregate results for the test of SN 3787 exhibited more consistency than did SN 3786 through the early stage of wear, as evidenced by the smaller margins of the 95% confidence intervals (Fig. 49). Once the welded surface began to deteriorate, however, a significant increase in the scatter of the data is noticed. This is attributable to the large tufts remaining partially attached to the fabric past a single interval of testing. The tufts were not removed but were allowed to detach during testing.

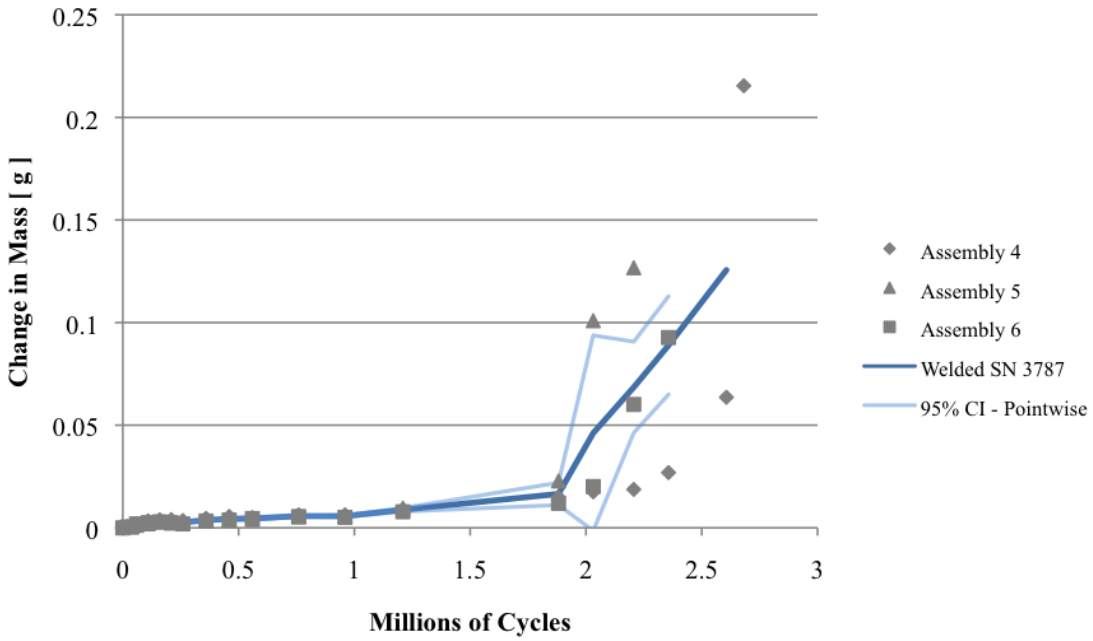

Figure 49: The aggregate wear behavior of SN 3787 (PET-LD) with pointwise 95% confidence intervals.

The welded satin-topped PET fabric (SN 3787) did not fare nearly as well as the previous two fabrics (Fig. 50). There is no distinguishable difference in the wear of the surface layer as compared to the subsurface layers. This fabric also failed much earlier than the two orthogonal PET fabrics above. During welding trials for this fabric architecture, it was noticed that the yarns of the surface layer did not weld uniformly as the orthogonal PET fabrics had. The 5-harness satin pattern on the surface is a loose fabric architecture. There is very little residual tension in the yarns after weaving and, thus, very little natural contact pressure between adjacent yarns. As a result, the pressure required for effective diffusion bonding between yarns is not reached. It is suspected that this is the cause of poor wear behavior of the satin surface.

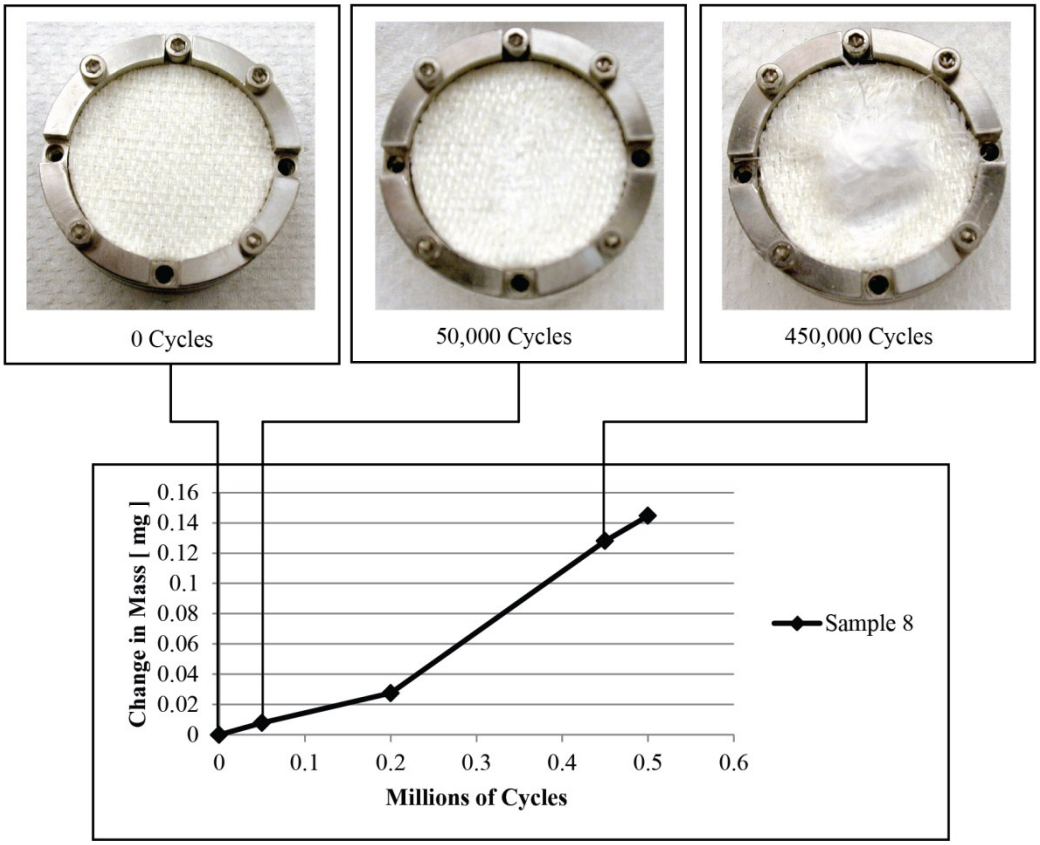

Figure 50: The wear history and evolution of damage of an individual sample of SN 3796 (PET-S).

The aggregate behavior of this fabric supports the previous explanation (Fig. 51). As wear progresses, scatter in the data increases and the 95% confidence intervals widen around the aggregate wear curve.

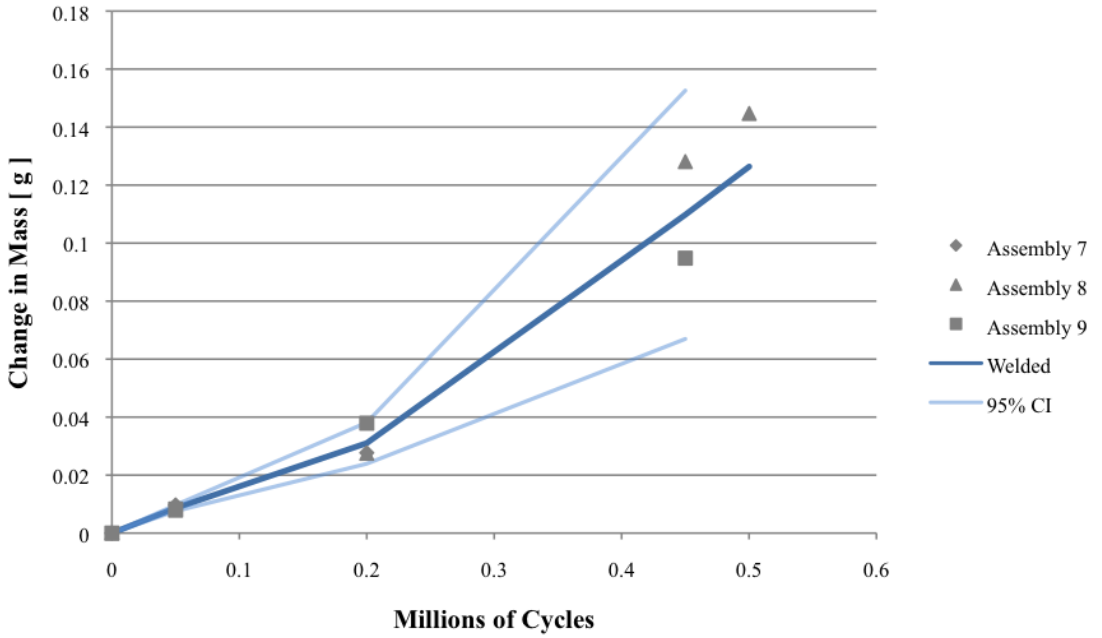

Figure 51: The aggregate wear behavior of SN 3796 (PET-S) with pointwise 95% confidence intervals.

As previously discussed, the two orthogonal PET fabrics (SN 3786 and SN 3787) exhibited distinct regions of wear. The wear curves are not monotonic and therefore require more than a single wear rate derived from the entire lifespan of the fabric. The wear performance can be divided into two regions: Welded Surface Wear and Virgin Subsurface Wear (Figs. 52 and 53). The quantitative analysis, coupled with the visual tracking of the fabric characteristics, show a clear change in wear behavior attributable only to the welded surface and the subsequent loss of that surface. As a result, two wear rates are calculated for these fabrics and are reported in comparison to the virgin fabric wear rates in Table 6 [corrected data from Giordano, 2011].

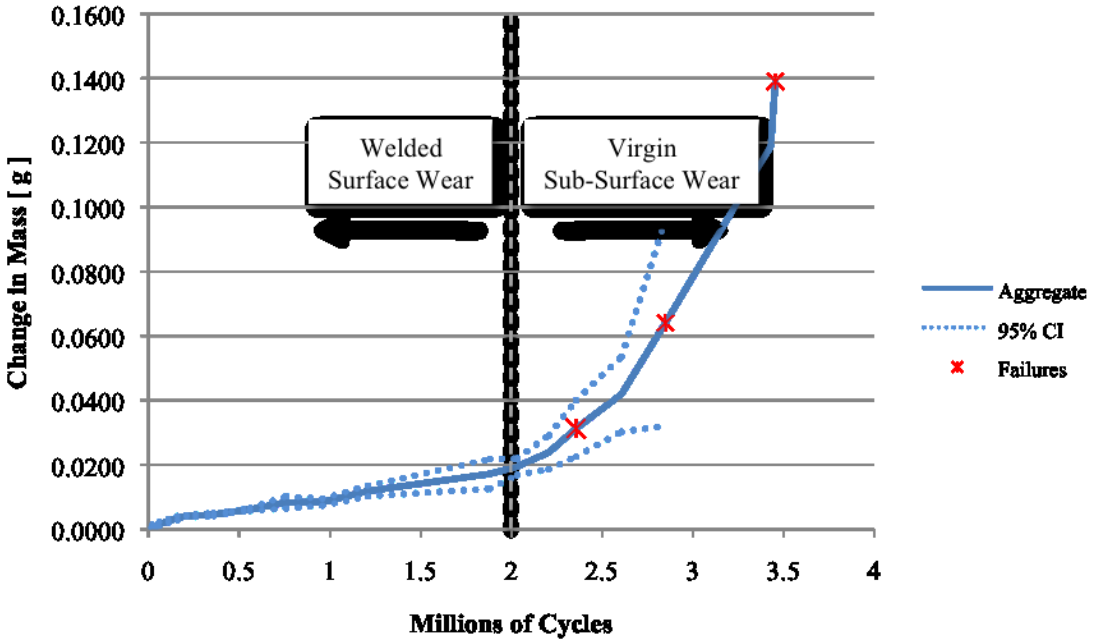

Figure 52: Two regions of wear performance for the aggregate behavior of SN 3786 (PET-HD).

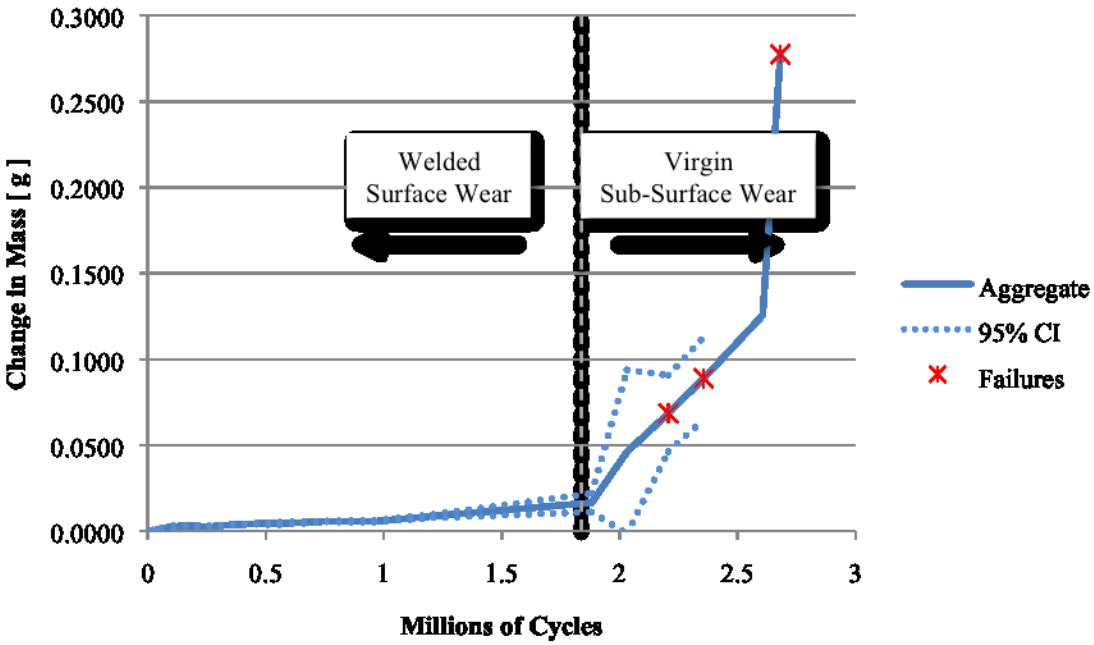

Figure 53: Two regions of wear performance for the aggregate behavior of SN 3786 (PET-HD).

TABLE 6

FABRIC WEAR RATES

	Virgin*	Welded	
Fabric Architecture	**Wear Rate [mg/Million Cycles]**	**Welded Surface Wear Rate [mg/Million Cycles]**	**Virgin Sub-Surface Wear Rate [mg/Million Cycles]**
SN 3786	230.3	9.550	71.17
SN 3787	142.3	8.788	138.1
SN 3796	130.2	244.0**	
SN 3825	6.032	2.899***	-

*From Giordano [2011].

**PET-S (SN 3796) displayed linear behavior to failure.

***UHMWPE-S (SN 3785) is reported through 1.15 million cycles.

The two welded orthogonal fabrics (SN 3786 and SN 3787) exhibit a reduction in wear rates of 95.9% and 93.8% respectively, during their Welded Surface Wear region. After the welding surface has been removed, the wear rates of the Virgin Subsurface Wear region increase by a factor of 6.45 and 15.7, respectively. The wear rate in this region of SN 3787 is essentially the same as for the virgin fabric.

The wear behavior of the virgin fabrics is linear with the exception of the UHMWPE-S (SN 3785) fabric (Fig. 54) [Giordano, 2011].

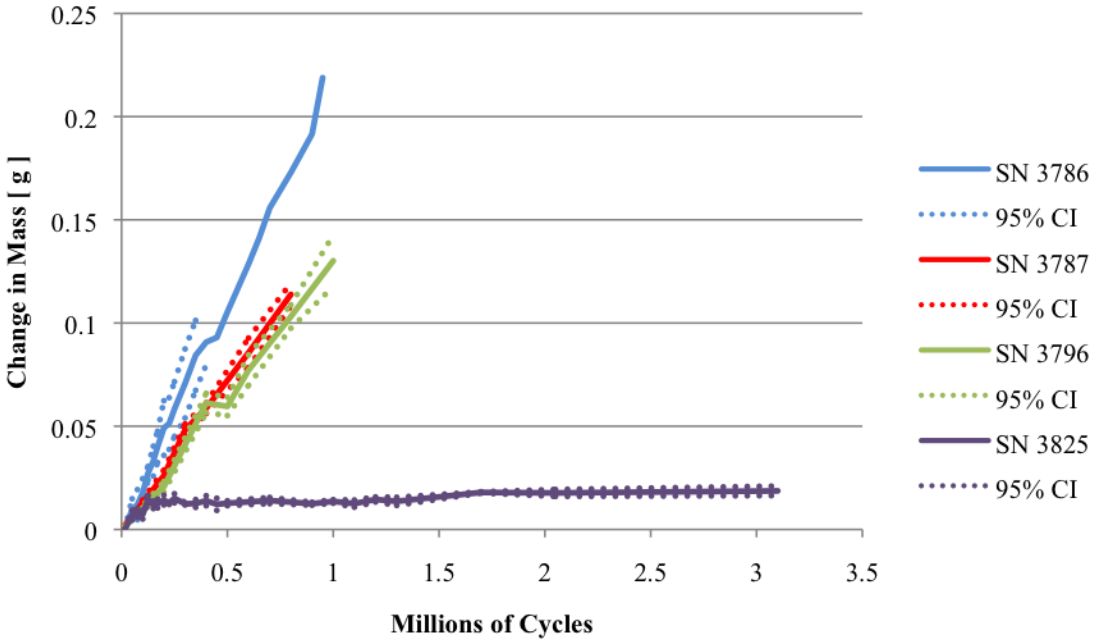

Figure 54: Wear of the four unwelded fabrics (corrected from Giordano, 2011).

The UHMWPE-S fabric exhibited a brief run-in period and followed by a plateau in the wear curve. The test was stopped, without failure, at 3.1 million cycles [Giordano, 2011].

The welded PET-HD (SN 3786) outperforms the virgin fabric through two million cycles. The welded surface essentially provides a two million cycle offset, or lifespan gain, in this fabric (Fig. 55).

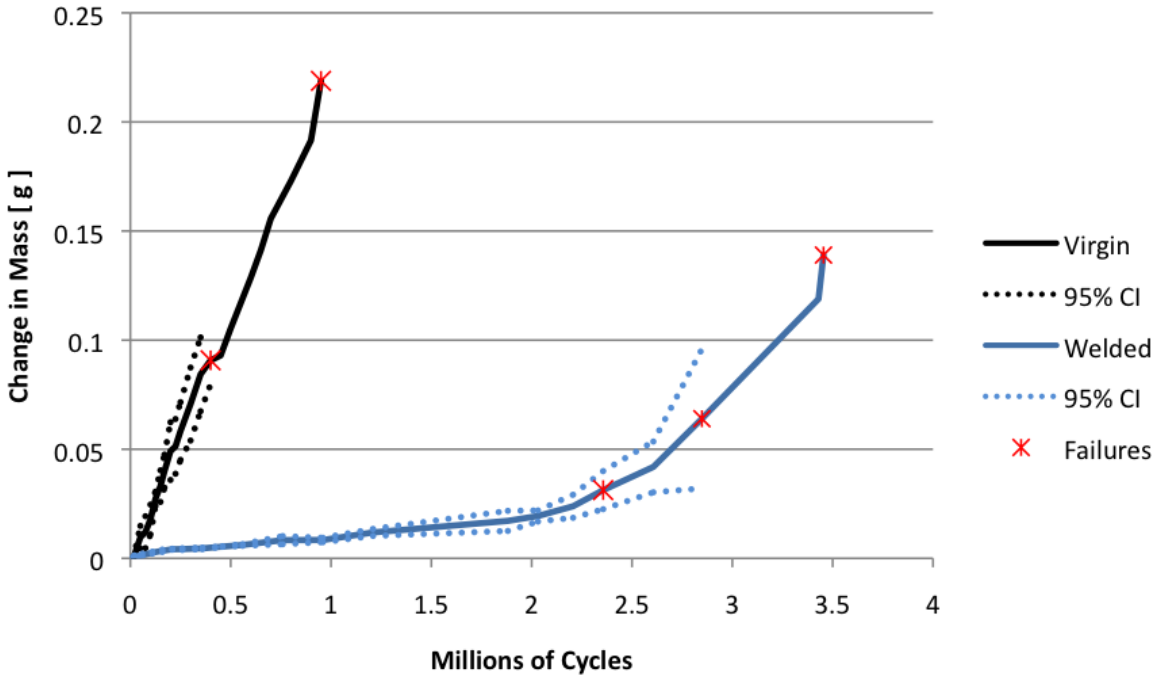

Figure 55: Comparison of the welded and virgin PET-HD (SN3786) fabric. The time of individual fabric failures are indicated on the aggregate line.

The welded PET-LD (SN 3787) outperforms the virgin fabric through roughly 1.9 million cycles. The high final wear value depicted here is due to a large tuft of fabric that had built up during the test on one sample (Fig. 56). During the interval in which the fabric was deemed failed, the tuft had detached and caused an increase in mass removal (Fig. 57).

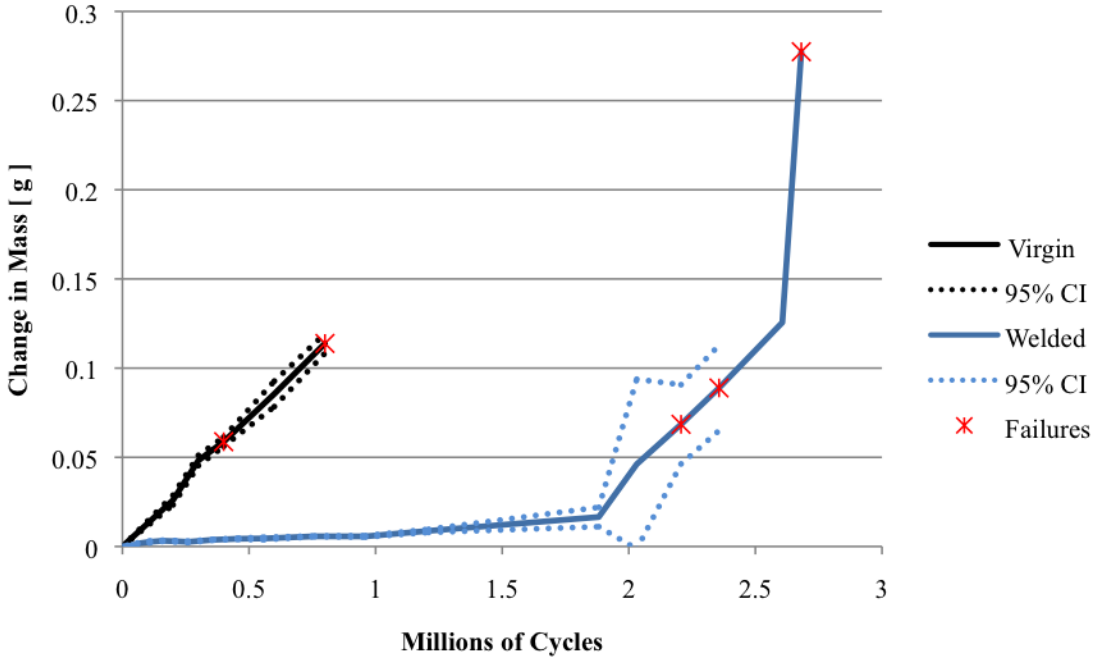

Figure 56: Comparison of the welded and virgin PET-LD (SN3787) fabric. The time of individual fabric failures are indicated on the aggregate line.

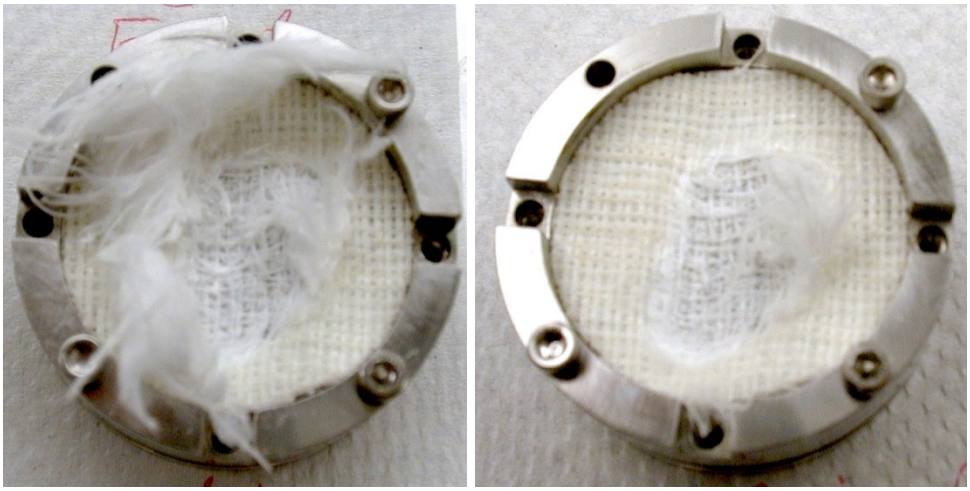

(a) (b)

Figure 57: A sample of PET-LD (SN 3787)
a) Before and b) after failure. The large tuft of fabric detached during failure.

The virgin and welded PET-S (SN 3796) fabrics had similar behavior throughout their lifespan (Fig. 58). The first welded fabric failure was determined to be due to a failure of the adhesive backing. The welded fabrics failed prior to the virgin fabrics. This is likely attributable to the inability to achieve high-quality welds of the satin layer. Instead, the welded fabrics appear to have been damaged, likely contributing to the worse wear performance. The 95% confidence intervals of the welded and virgin fabrics overlap and require further investigation. Finally, it is worth noting that the average pin roughness (R_q and R_a) increased over the entire duration of the wear tests (Table 7).

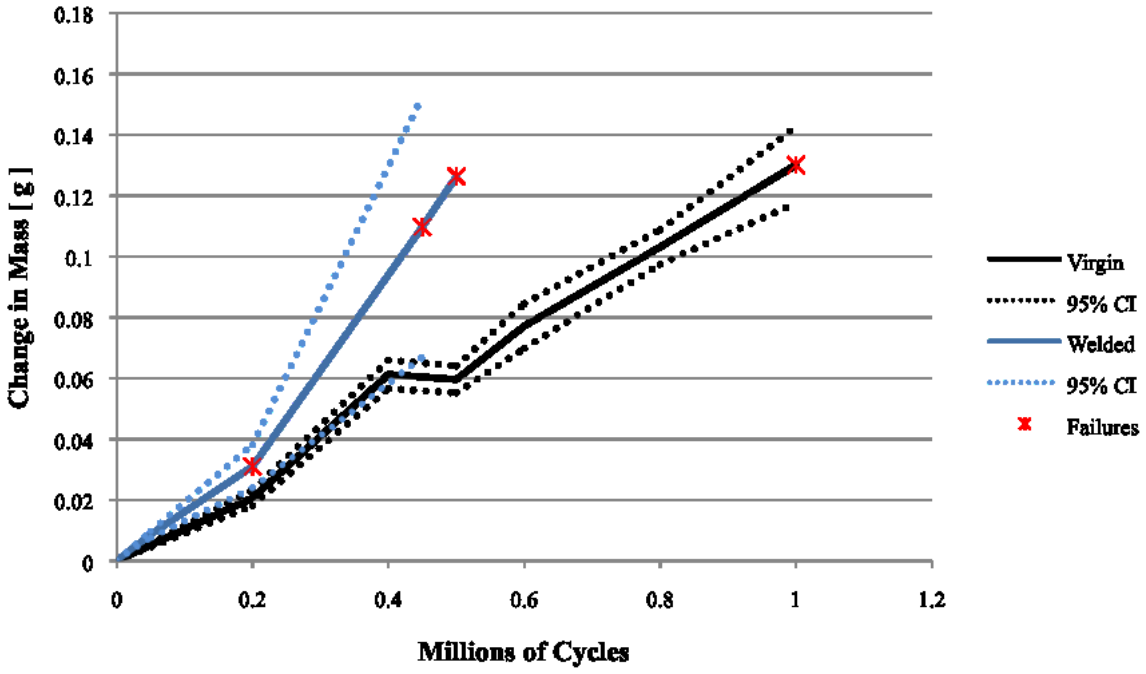

Figure 58: Comparison of the welded and virgin PET-S (SN3796) fabric. The time of individual fabric failures are indicated on the aggregate line.

TABLE 7

PIN ROUGHNESS VALUES

	Rq [nm]	Ra [nm]	Peak-to-Valley [μm]
Beginning	49.7 ± 31.8	38.0 ± 24.2	1.57 ± 1.2
End	407 ± 117	256 ± 148	4.40 ± 0.823
Increase	180%	720%	575%

Demonstrate that the Woven Composites Maintain a Long Life: Wear Testing of Multi-Weave 3D Materials Pin-on-Disk

All our wear testing was done on specimens that contained a single weave.

Demonstrate that the Woven Composites Maintain a Long Life: Wear Testing of Multi-Weave 3D Materials Joint Simulator

This task is dependent on an industry partner and is pending. At this timepoint, it is felt that more pin-on-disk testing is required before allocating joint simulators to the program. Based on the pin-on-disk testing, the welded-woven composites are very attractive, but because simulator testing is expensive and very time consuming, it should only be done after thorough screening tests.

Assess Cartilage Damage and Wear: Design Specimens and Wear Test

Experimental techniques to repair focal defects in articular cartilage involve replacing a small area of damaged cartilage with an artificial implant. An important consideration with these devices is the potential for cartilage to wear against the implant surface. To evaluate these implants and to screen for optimal materials and finishes, a method to quickly and accurately predict *in vivo* cartilage wear is required. In determining the optimal set up, two different cartilage surface geometries were compared: smaller specimens had a flat surface that made complete contact with the opposing disc during wear testing while larger ones made contact in the center of the specimen but not at the edge due to the radius of curvature of the articulating surface. The flat surface of the smaller specimens conformed to the disc to provide a well-defined and consistent contact area and allowed for a relatively uniform contact pressure. However, an artifact of the specimen preparation is the cut cartilage edge. In the larger convex specimens, this cut edge was separated from the disc and did not directly experience wear, while in the smaller specimens the edge was exposed to contact pressure and frictional forces. The two

geometries were compared using three different metrics to quantify cartilage wear: a modified wear factor based on the mass of cartilage removed per N-m was calculated, the surface damage was assessed with a semi-quantitative method, and the change in surface roughness was measured. To interpret experimental data from the two different specimen geometries, three dimensional finite element (FE) models of a single phase elastic solid undergoing sliding contact were created using a commercial FE software package, and maximum shear stress was evaluated.

Methods

Samples with 1/4 and 3/8" diameters were prepared as has been described previously [McGann and Wagner, 2009] and were equilibrated overnight in a 0.15 M saline and protease inhibitor solution [Wagner et al, 2006]. Surface images were taken before testing with the use of India ink to ensure no surface imperfections or damage were present. To determine contact area for each sample, a 44 N load applied pressure between the articular cartilage surface and a sheet of paper covered with charcoal, resulting in a transfer to the cartilage [McGann and Wagner, 2009]. Images of the articular surface were captured with a digital camera through a dissection microscope and were analyzed to determine contact area (Matlab).

The surface curvature of the 3/8" samples was measured with a scanning white light profilometer (New-View 6300; Zygo Corp., Middlefield, CT) using a 2.5X objective. Specimens were placed on a level stage so that the measured curvature would be that of the surface contacting the wearing plane. Measurements were taken in three locations and the overall curvature as well as the radius of curvature were recorded. The 1/4" samples were considered flat, and the curvature was not measured.

Wear testing was performed with a pin-on-disc wear testing machine (OrthoPOD from AMTI, Watertown, MA) at room temperature at approximately 1.4 MPa in a saline solution with protease inhibitors. One cycle consisted of four 18mm strokes in the shape of a square, with a rehydration length of 45% along each side [Bell et al., 2006] at 4 mm/s [Forester et al., 1996] for a total of 2400 cycles. Specimens were tested against stainless steel discs (R_a= 0.018 ± 0.003 um).

Pre- and post- wear surface roughness measurements were obtained with the same optical profilometer as above (Zygo) with a 20 X Mirau interferometric objective. The vertical resolution of the device is less than 0.55 μm, which is well below the surface roughness measurements obtained in this study. Prior to measurements, the surface was blotted with low lint wipes, sprayed with canned air for 5s, and air dried for 1-2 min at room temp in order to avoid interference of discrete fluid films with the interferomety measurements [Shekhawat et al, 2009].

After testing, India ink was again used in images of the articular surface. A visual, semi-quantitative analysis of the wear was performed by quantifying the amount of India ink adhering to each surface (Matlab).

Two statistical correlations were performed: 1) surface curvature vs visual wear of the 3/8" samples, and 2) change in roughness vs visual wear (GraphPad Software, San Diego California USA).

Evaluation of Specimen Surface Geometry for use in Wear Testing

As has been discussed in previous reports, initial wear testing of cartilage on steel yielded three distinct groups with varying degrees of visual wear (Fig. 59). The larger 3/8" samples, having a smaller radius of surface curvature appear to have significantly less wear than the smaller 1/4" samples. However, the two distinct groups of the 3/8" samples are of some concern should this size be used for testing of cartilage friendly materials. The varying degree of wear from sample to sample could cause incorrect differences in the wear of the cartilage against different potential implant composites. To resolve this, the cause of these differences needs to be identified.

It has been hypothesized that varying degrees of curvature are the cause behind the observed differences; samples obtained from larger bovine knees have a greater radius of curvature resulting in a larger contact area upon loading. A study comparing the effect of the surface curvature on the wear of the samples consisted of the 3/8" samples with varying curvature and 1/4" samples (n=7). The radius of surface curvature of all the 3/8" specimens ranged from 1.2 to 4.8 cm. Samples with a smaller radius of curvature had contact in the central region of the sample, with clear separation around the circumference of the pin. The larger surface curvature appeared to be nearly flat with limited separation around the circumference. The surface curvature of the smaller samples was not measured as these samples were considered to be flat and in complete contact with the wearing plane upon loading.

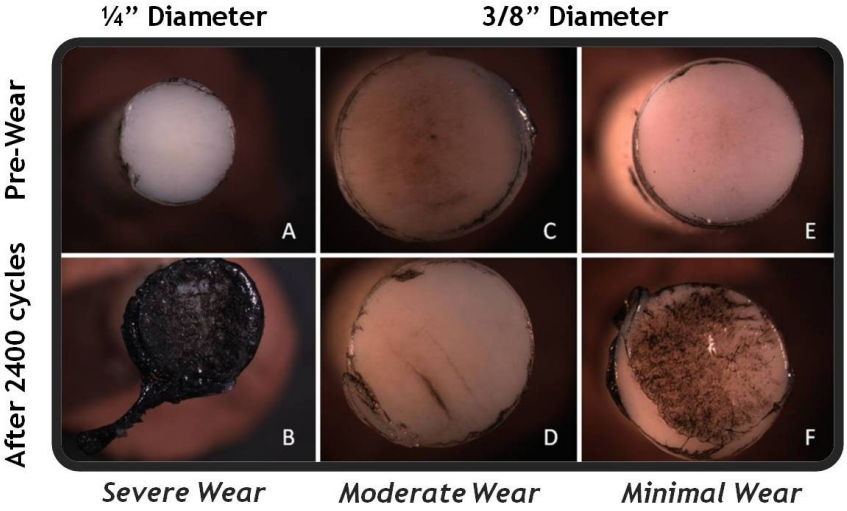

Figure 59: Visual grouping of worn samples.

No correlation between the initial surface curvature and the visual wear was found (Figure , $p=0.641$). However, the change in surface roughness after the wear test does correlate to the visual wear (Figure , $p<0.02$).

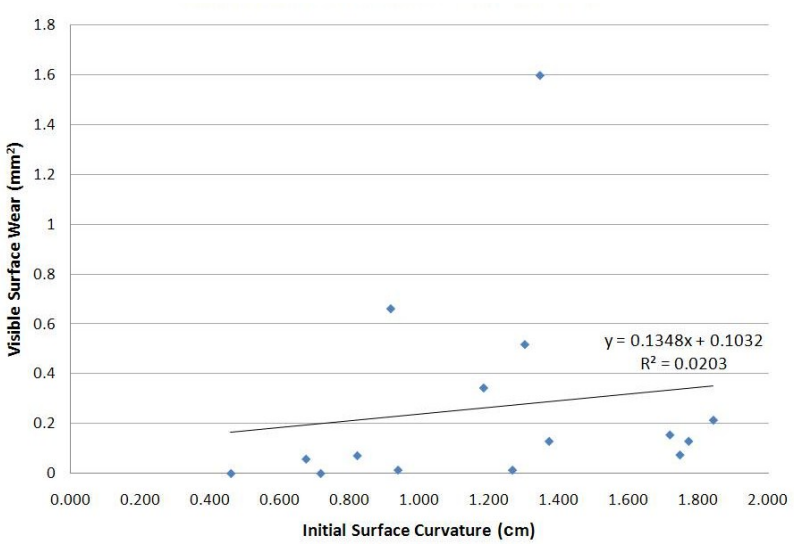

Figure 60: Initial Surface Curvature vs Visual Wear. No correlation was found (p=0.641).

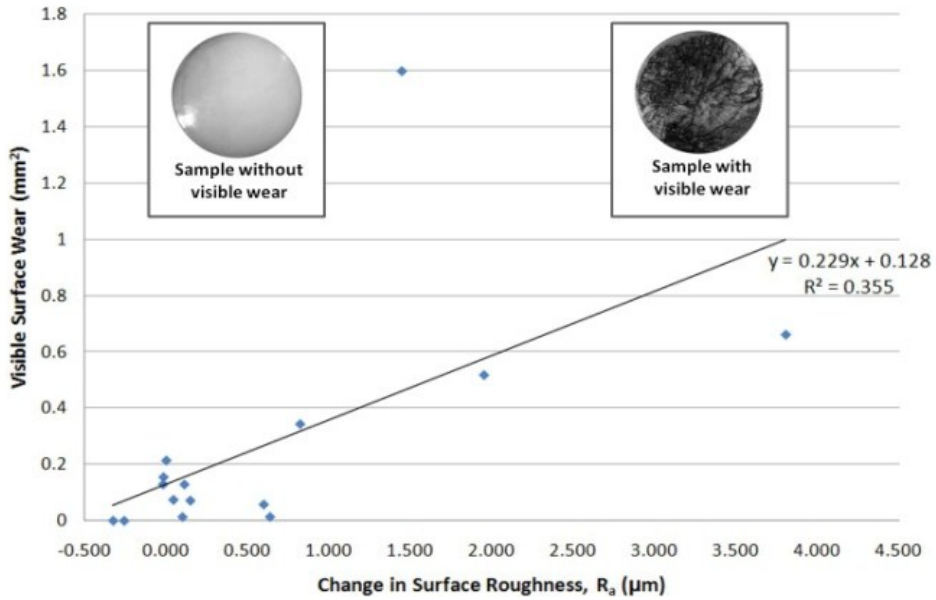

Figure 61: Change in Roughness vs Visual Wear. These factors are positively correlated ($p < 0.02$).

Results of this study demonstrate that the surface curvature of the specimens does not affect the specimen wear. It was hypothesized that a smaller radius of curvature would eliminate the stress concentration at the cut edge of the specimen and would generate less wear. However, the results of this study suggest that for a given anatomical location surface curvature may not need to be considered when harvesting samples.

The significant correlation between the change in surface roughness and the visual wear of a specimen offers the potential to use surface roughness measurements as a quick means for evaluating specimen wear. It was previously shown that surface roughness itself does not

correlate well with wear [Verberne et al., 2009], but this study demonstrates that the change in surface roughness before and after wear does correlate to the visual wear of the specimen. If validated chemically, changes in surface roughness can be used in future testing to quickly screen proposed implant materials.

Chemical Analysis

In order to quantify the amount of cartilage that is worn away from the samples chemical analysis has been used. Because the composition of cartilage varies with depth, an appropriate analysis technique that could directly relate to mass of cartilage needed to be selected. The major constituents of the organic matrix of cartilage are collagen and glycosaminoglycans. Since hydroxyproline is a unique constituent of collagen it can be used to determine the amount of wear of cartilage tissue during an experiment. It has previously been found that hydroxyproline content is consistent throughout the depth of cartilage and is thus an adequate means for determining the amount of wear of the tissue during the course of an experiment [Lipshitz et al., 1975]. The weight percent of hydroxyproline was found to be approximately 7.8% throughout the depth of bovine articular cartilage [Verberne et al., 2009]. Further, HPLC measurement of hydroxyproline is sensitive, accurate, and easy to perform.

Past testing has revealed two main issues with the chemical quantification protocol being used. First, and most importantly, there was a significant loss of material during the sample preparation process. And second, a potential interference from the chemicals being used as protease inhibitors was observed.

In investigating the cause for the loss of material, two areas of concern were identified. These two areas are improper hydrolysis of the lubricating fluid and debris causing degradation of the hydroxyproline, or a loss of hydroxyproline during the filtering process. Because the hydrolysis in HCl at elevated temperatures is a well-used and documented process, focus was placed on the potential for material lost at the filtering stage. A 10μM hydroxyproline standard was analyzed and compared to a filtered 10μM hydroxyproline standard (0.22μm pore size). While there was some loss of material, approximately 0.5μg, the filtering process did not account for the entire loss of hydroxyproline previously observed. This loss of material corresponded to the filtered hydroxyproline standard having a concentration of 7.7μM, as opposed to the expected concentration of 10μM. Due to the loss of over 30% of the material, using a filter with larger sized pores is recommended.

Each of the components of the lubricating fluid were analyzed to determine if there was any interference with the chemicals being used. To do this, each of the protease inhibitors added to the lubricating fluid (EDTA (DS), EDTA (TS), NEM, PMSF, and Benzamidine) were hydrolyzed with 6 M HCl, dried and then derivatized and run through HPLC. The internal standard, sarcosine, was added to each of the above mentioned ingredients. There was no affect on the internal standard when combined with EDTA (TS), NEM, PMSF, or Benzamidine. However EDTA (DS) inhibited any detection of the internal standard, and instead had another highly florescent component present. Because the ratio of hydroxyproline to sarcosine is necessary for the current quantification process, EDTA (DS) has since been eliminated from the protease inhibitor cocktail.

The last step in the analysis of the chemical quantification focused on the use of an internal standard (IS), sarcosine, in the quantification of hydroxyproline, and in turn cartilage. With this work, the two primary reasons for using an IS are: 1) to compute a ratio of the fluorescence intensity of the hydroxyproline to that of the sarcosine in order to obtain the concentration of the hydroxyproline in the sample, and 2) to ensure that all samples have been properly derivitized and that fluorescence tags have properly attached to the amino acids. Following reported methods from the literature, this internal standard was initially added to the dehydrated samples prior to the extraction of the amino acids. Further research determined that when performing HPLC in quantitative bioanalytical methods, the biofluids should be spiked with analytes after extraction to allow for accurate analysis. A new standard curve in which the IS is added following extraction was generated and future procedures were altered to adhere to these findings.

Frictional Coefficient Analysis

One of the reasons that cartilage is believed to have such low wear rates *in vivo* is the low coefficient of friction of cartilage on cartilage movement. To better track the onset of damage to the superficial layer of the cartilage and the initiation of wear, the coefficient of friction can be measured throughout all future wear testing. The coefficient of friction can in fact be tracked throughout the course of the wear test with the current set up (Figure , Figure). Thus far, no direct correlation has been identified between the coefficient of friction and the wear of the cartilage. This could be for one of two reasons: 1) the wear test is not being carried out long enough to observe the increase in the frictional coefficient, or 2) any noticeable increase in the coefficient of friction is occurring in the first 200 cycles, and is thus not seen. It is unlikely that either of these is occurring. If the wear test is in fact too short to capture an increase in the frictional coefficient, then the use of this parameter to identify the onset of wear is not of use to us, as the samples are already significantly worn. At the other extreme, if the increase in the coefficient of friction, and thus the proposed onset of wear, is occurring before the first 200 cycles, then the current testing procedure is not accurately replicating the wear of articular cartilage in vivo. The analysis of the frictional coefficient and its accuracy is being explored to determine if it could be used to detect the onset of wear.

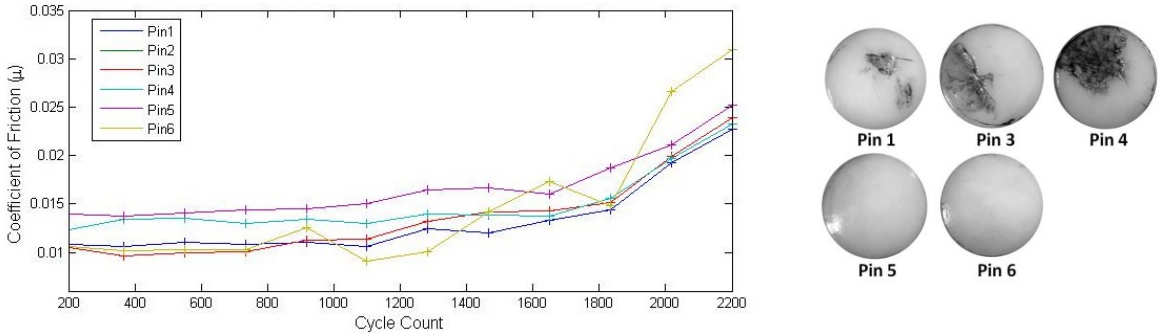

Figure 62: Group 3, (left) frictional coefficient over time, (right) post-wear images.

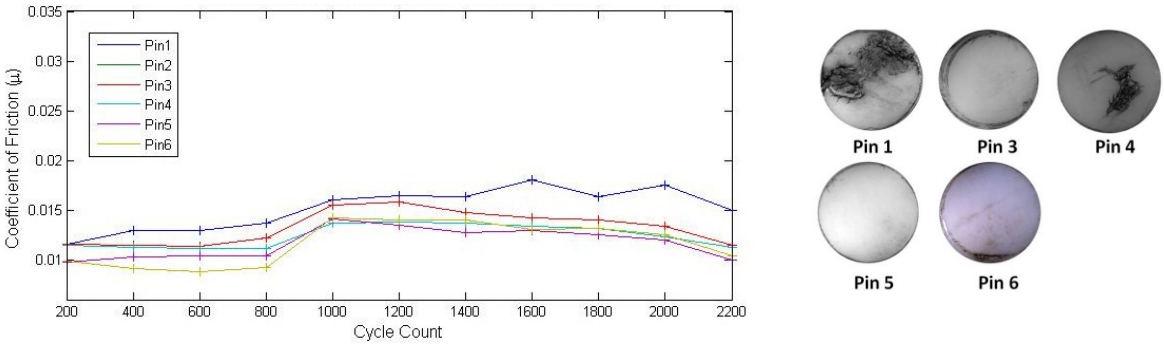

Figure 63: Group 4, (left) frictional coefficient over time, (right) post-wear images.

Finite Element Analysis

In addition to the above experiments, three dimensional FE models of single phase elastic solids undergoing sliding contact were created using a commercial FE software package (Abaqus 6.10-1ef, SIMULIA Inc., Providence, RI) to help interpret the experimental data for the two specimen geometries tested. Two different models were created, representing the specimen geometries; the first model was of a flat, 6.35 mm diameter cartilage-bone cylinder and the second model was of a 9.53 mm diameter cartilage bone cylinder with a centrally located flat region with a diameter of 6.35 mm (Fig. 64). A thickness of 0.6 mm was assigned based on experimental measurements. The cartilage tissue was modeled as a linear elastic material with a modulus of 8.6 MPa [Hayes and Bodine, 1978] and a Poisson's ratio of 0.2 [Radin et al. 1973]. The opposing surface was an analytical rigid body representing the steel discs in the wear test. The model was discretized with four-node quadratic tetrahedron elements (C3D10M) seeded at 0.2 intervals around the circumference of the contacting surfaces, generating 30,420 and 63,477 elements in the flat and curved models, respectively. The simulation was carried out through two steps: first the specimen was loaded in the y-direction followed by propagation in the x-direction. In order to simulate the constraining effect of the subchondral bone, the top surface of the cartilage was restricted from rotation and displacement in the x- and z-directions during loading. To allow movement in the second step, displacement was permitted in the direction of sliding but was constrained otherwise. In the model of the flat specimen, a load of 44N was simulated on the cartilage with a loading rate of 80 N/s. Due to the increased contact area in the larger specimen, the load was increased to 72N to obtain a contact pressure of 1.4 MPa, the same as the smaller specimen. Once loaded, the cartilage traveled along a 1 cm path with a coefficient of friction of

0.07 [Merkher et al. 2006]. Because shear stress has been associated with cartilage damage, the maximum shear stresses along the midline of the contacting surfaces were evaluated.

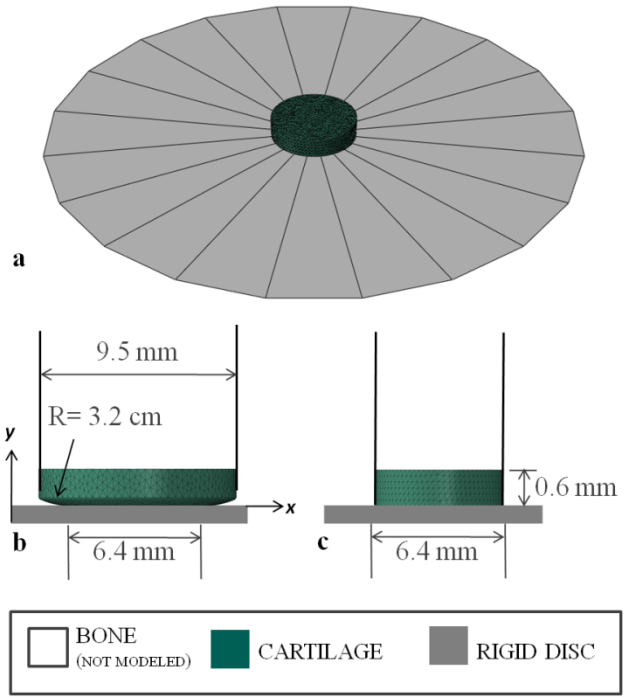

Figure 64: Geometries for FE model. (a) Cartilage model against rigid surface, (b) profile of large, curved specimen and (c) profile of small, flat specimen.

The average contact stress from the each FE model was in agreement with the expected stress of -1.4 MPa. The FE simulations showed a shear stress concentration at the leading edge of the smaller specimen, which was reduced at the cut edge of the larger specimen (Figure 65). The maximum shear stress at the cut edge of the specimens was decreased in the larger specimen by 94% and 89% at the leading and trailing edges, respectively. This reduction in shear stress at the cut edge of the larger, curved specimen is in agreement with the reduced wear observed in the larger specimen when compared to the smaller, flat specimen. Both the experimental and computational results will be applied to future studies evaluating both prospective implant materials and treatments for improving the wear of native cartilage.

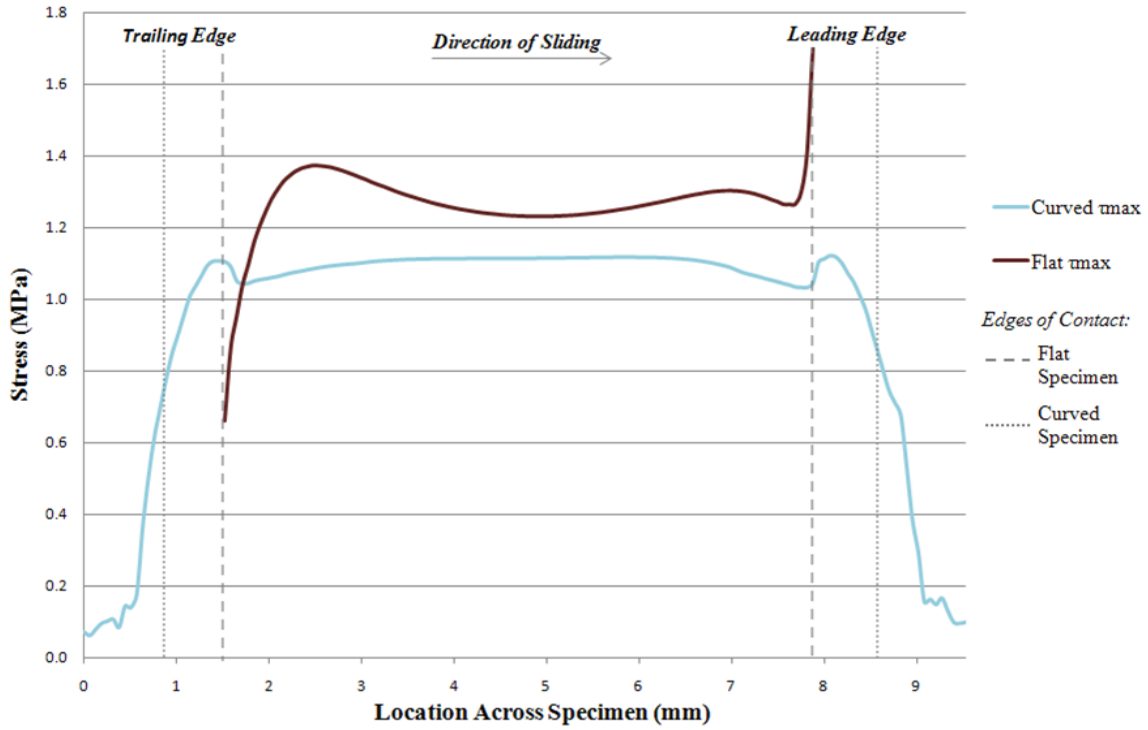

Figure 65: Maximum shear stress along the midline of flat and curved specimens following sliding contact from the FE model. Dashed grey lines denote edges of contact.

Assess Cartilage Damage and Wear: Testing Incorporating Woven Materials- Pin on Disk

Once tests had been completed to determine the best method for wear testing cartilage, tests were performed against various 2-dimensional woven materials from Zimmer. Four polyester (PET) weaves and eleven polyethylene (PE) weaves were tested, as well as PET and PE pucks. Two different clamping methods were used for testing the woven materials.

Specimen Preparation

Articular cartilage specimens were taken from bovine knees, as was described above. Locations on the femur were isolated, and 3/8 in diameter specimens were cored out using a drill press. Specimens were hydrated with Optimal Cutting Temperature (O.C.T.) compound and phosphate buffer saline (PBS), vacuum packed, and frozen for storage. Before testing, specimens were thawed and hydrated in PBS for 1 hour.

Experimental Setup

Wear tests were performed on an OrthoPOD machine, which could test 5 samples at a time. As shown in Figure 66, the testing materials were attached to the bottom plate. The surrounding cylinder held in 18 mL of lubricating fluid. Throughout the entirety of the test, the cartilage specimens were submerged in the lubricating fluid. Cartilage that wore off was collected in the lubricating fluid bath, and the solution was stored frozen for chemical analysis.

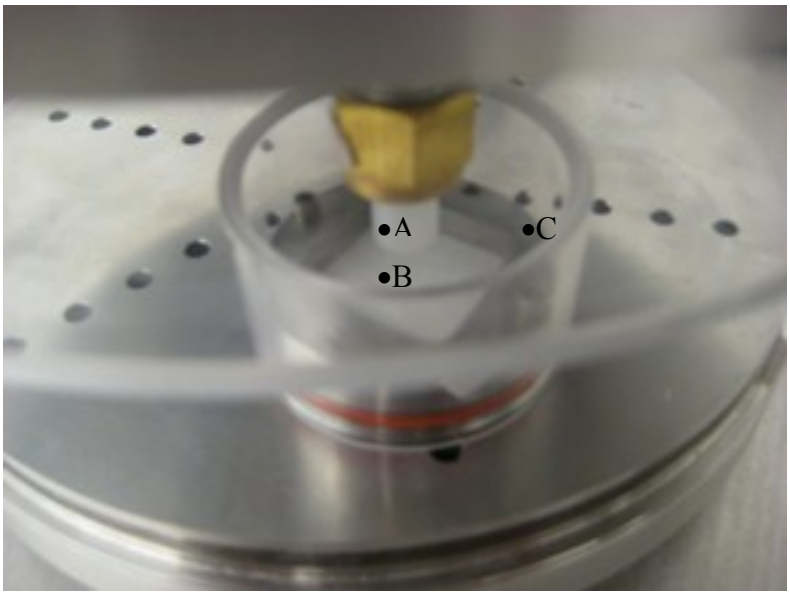

Figure 66: OrthoPOD testing setup. A: Cartilage specimen, B: Wear surface (woven material), C: Container for lubricating fluid

Wear Pattern

- 12 mm line back and forth
- Aligned with the grain of the fabric
- Loaded for first 6 mm, then lifted for next 6 mm [Bell et al., 2006]
- Speed: 4 mm/s [Forester et al., 1996]
- 2400 cycles
- Test length: 4 hours
- Pressure: 1.4 MPa. The initial contact area of each specimen was measured and used to determine the load required for 1.4 MPa minimum for each specimen in the test. [Cottrell et al., 2008]

Analysis

- Imaging
  - After testing, the cartilage specimens were stained with black india ink, and imaged under a microscope at 2X magnification.
  - The ink attached to the damaged fibers and showed the texture of the specimen surface.
- HPLC
  - Chemical analysis was done on the lubrication fluid samples to determine the mass of cartilage worn off during testing.
  - Samples were freeze-dried and hydrolyzed in 6N HCl for 18 hours at 110 degrees F and dried. The hydrolysates were dissolved in a known volume of purified water and filtered. Sarcosine was added as an internal standard. The elution time and efficiency of hydroxyproline were determined with a hydroxyproline standard. [Hutson et al., 2003]

  - Hydroxyproline and the internal standard were quantified by HPLC; from the ratio of the two, the concentration of the hydroxyproline in a sample can be determined.
  - Hydroxyproline is found primarily in collagen and the amount of collagen in the sample can be calculated directly from the hydroxyproline measurement. From the collagen concentration, the dry weight of cartilage can be found [Lipshitz et al, 1975].
  - The preparation and chemical analysis were time consuming, so the HPLC could not be done for all samples.
- Surface Roughness
  - As preparation, each specimen was blotted with a Kimwipe and dried with a jet of nitrogen gas for three seconds. [Shekhawat et al., 2009]
  - The surface roughness of each specimen was measured using a ZYGO New View with a 20x objective.
  - Three measurements were taken for each specimen before and after testing.

Results

Group 1: Polyester Wovens (PET)

The initial method for clamping the woven materials used a strap as a backing as shown in Figure 67. Because tests were only being done with the two-dimensional materials, the strap was used to imitate the compliance of the 3-dimensional weaves. The strap on top of the wovens kept the wovens from slipping.

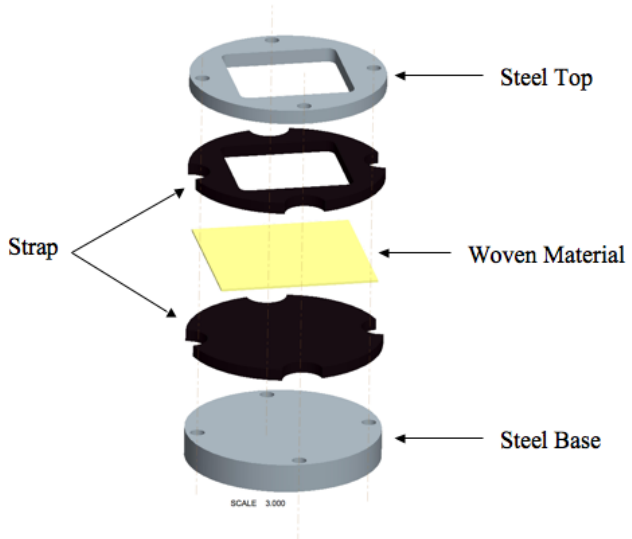

Figure 67: Initial clamping method for woven materials

The clamping method with the strap was used for the majority of tests on the PET materials. Figure 68 can be compared to the images in Figures 69, 70, 73-78 to see the wear on the specimens after being tested on PET wovens.

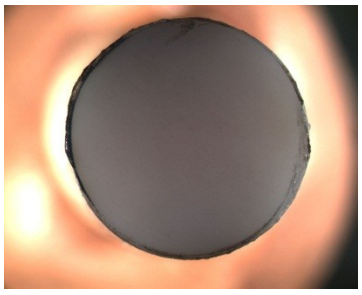

Figure 68: Stained cartilage specimen before wear testing

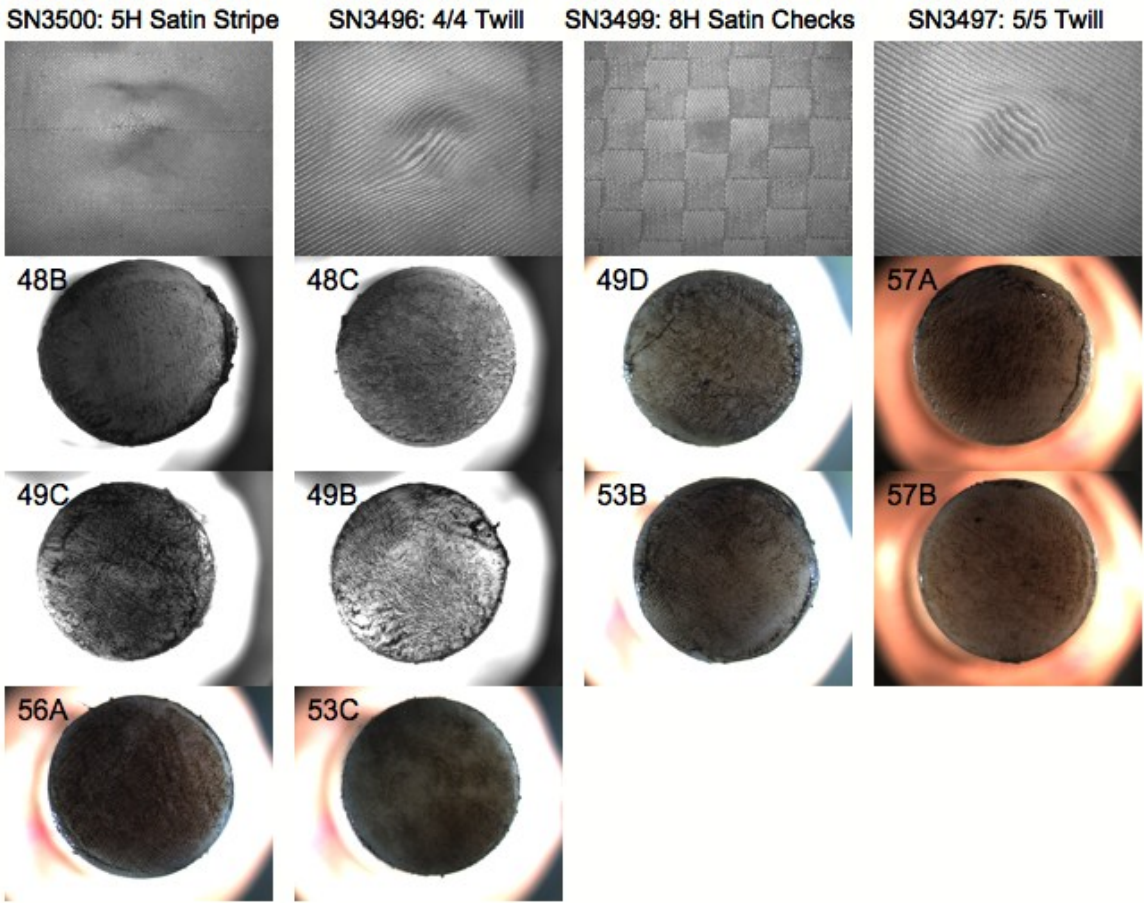

Figure 69: Stained cartilage specimens after wear tests on PET wovens. Each column of specimens in was worn on the same type of material, shown at the top. Each specimen used a new piece of the material.

After one test, it can be seen that each of the woven materials deformed. Each of the specimens has significant wear, but from these images the wear appears to be about the same. From these test, no material can visually be determined to wear better than another (Figure 69).

As a comparison, wear tests were also done on flat, solid PET pucks. The wear on the PET pucks was significantly less than the wear on the PET fabrics (Figure 70). Also, the wear from the pucks is only in the center of the specimens, where the initial contact area was. The clean

white surfaces at the edges of the specimens show that theses area did not wear. However, the specimens worn on the woven materials wore across the entire surface, probably due to the conformity of the strap. When the cartilage specimens wore edge-to-edge, the surface area is greater than the initial area measured, so the contact pressure decreases. Also wearing edge-to-edge brings into account the flaws on the edges cause by coring the specimens with the drill press, which could increase the wear.

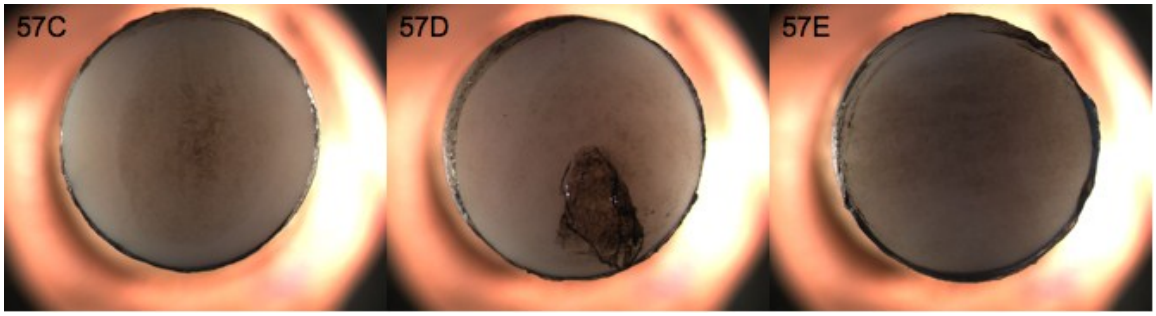

Figure 70: Stained cartilage specimens after wear tests on PET pucks

With the deformed woven materials and the cartilage wearing from edge to edge, it is likely that the compliance of the strap under the wovens caused the wovens to form to the shape of the cartilage. To avoid this effect, a new method of clamping was used. As Figure 71 shows, the strap was removed, and the woven material was clamped directly between the steel base and steel top.

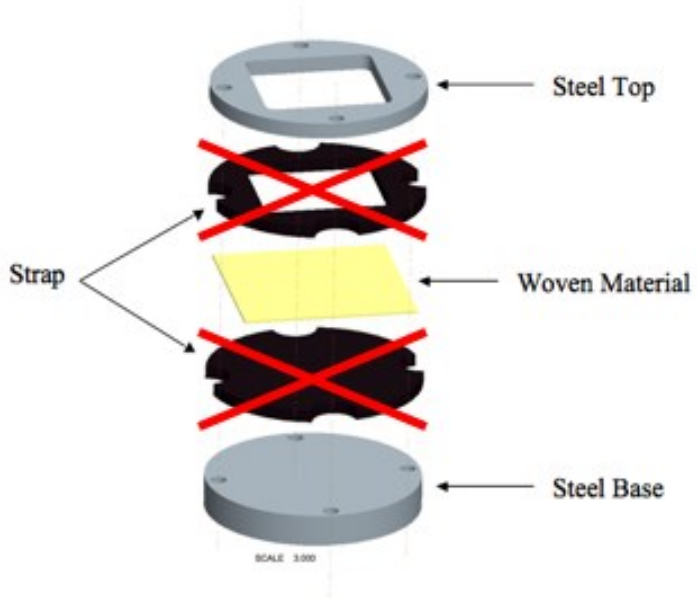

Figure 71: Revised clamping method without strap

The new clamping method was tried initially on two PET wovens, and after testing with no strap, the wovens did not deform (Figure 72). This method was used for the remainder of testing. Because of the limit of time, only one test used this clamping method for PET wovens. There

were more polyethylene (PE) wovens to be tested, which felt smoother to the touch and were expected to wear better, so the remaining tests were done with PE wovens.

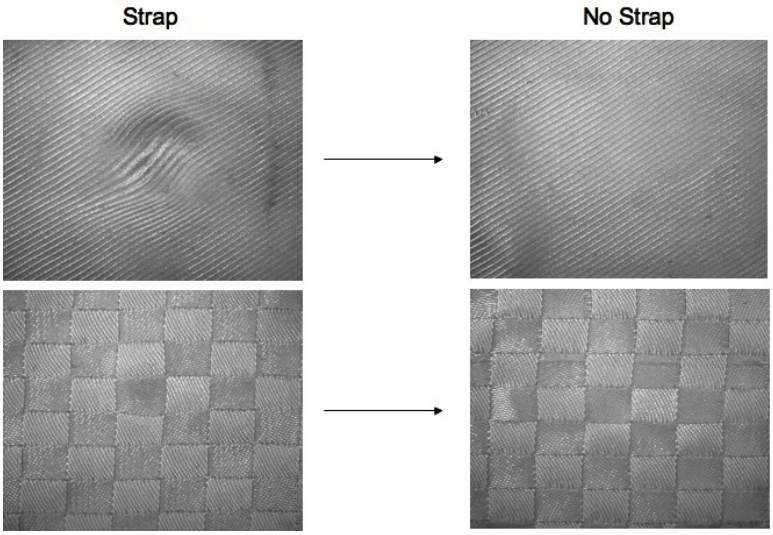

Figure 72: PET wovens after wear tests with different clamping methods

Group 2: Polyethylene Wovens (PE)

One test was done comparing PET to PE wovens with no strap. After wearing, there was still white on the edges of the specimens, so they did not wear across the entire surface (Figure 73). The PET satin stripes and the PE twill appeared to cause the least wear. The PET satin checks, and PE satin appeared to cause slightly more wear. The PET twill wore all the way to the bone. The wear for the PET twill is much worse in this test than in the tests with the strap, but in this test, there are noticeable differences between the fabrics, unlike the tests with the strap.

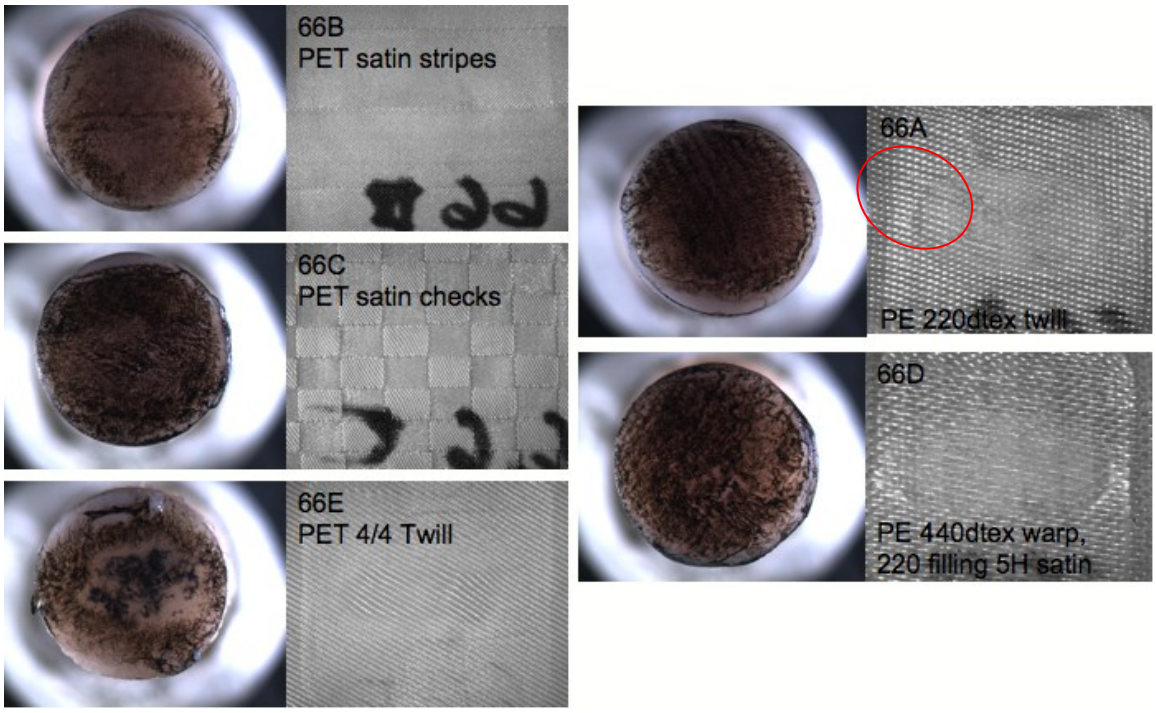

Figure 73: Cartilage specimens after wear test on PET and PE wovens with no strap. None of the PET wovens were damage in this test. The PE twill (66A) did have one thread come loose, circled in red.

On all three samples worn on plain weaves, the threads on the woven materials were separated and deformed (Figure 74). On the 60D sample, a group of threads were also pulled out of the side where the material was cut. Because of the severe damage to the cartilage and to the wovens, no further tests were done using plain weaves.

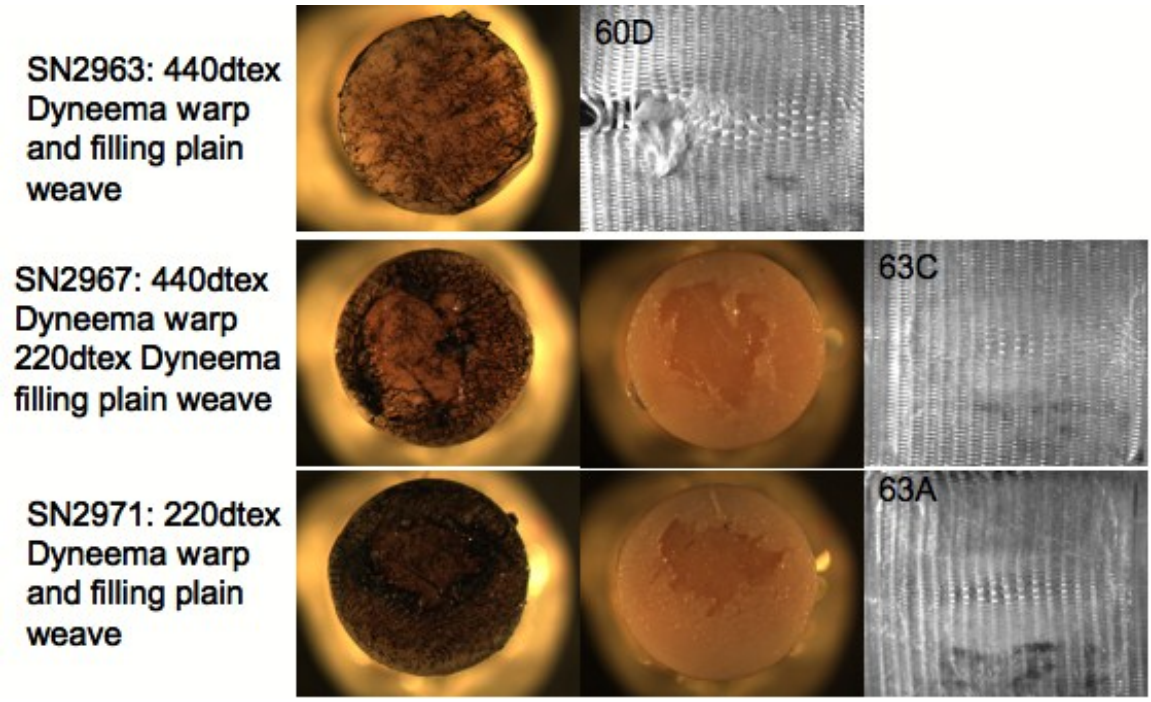

Figure 74: Cartilage specimens after wear tests on PE plain weaves. All specimens wore significantly, and the 63C and 63A specimens wore down to the bone, which can be seen clearly by the pink in the unstained images.

The PE 8 harness satin weaves were significantly damaged in the wear tests (Figure 75). On 61E, a large thread appears to have pulled out of its weave from the side. The specimens all had significant wear, with SN2962 being better than the other two wovens, which wore down to the bone.

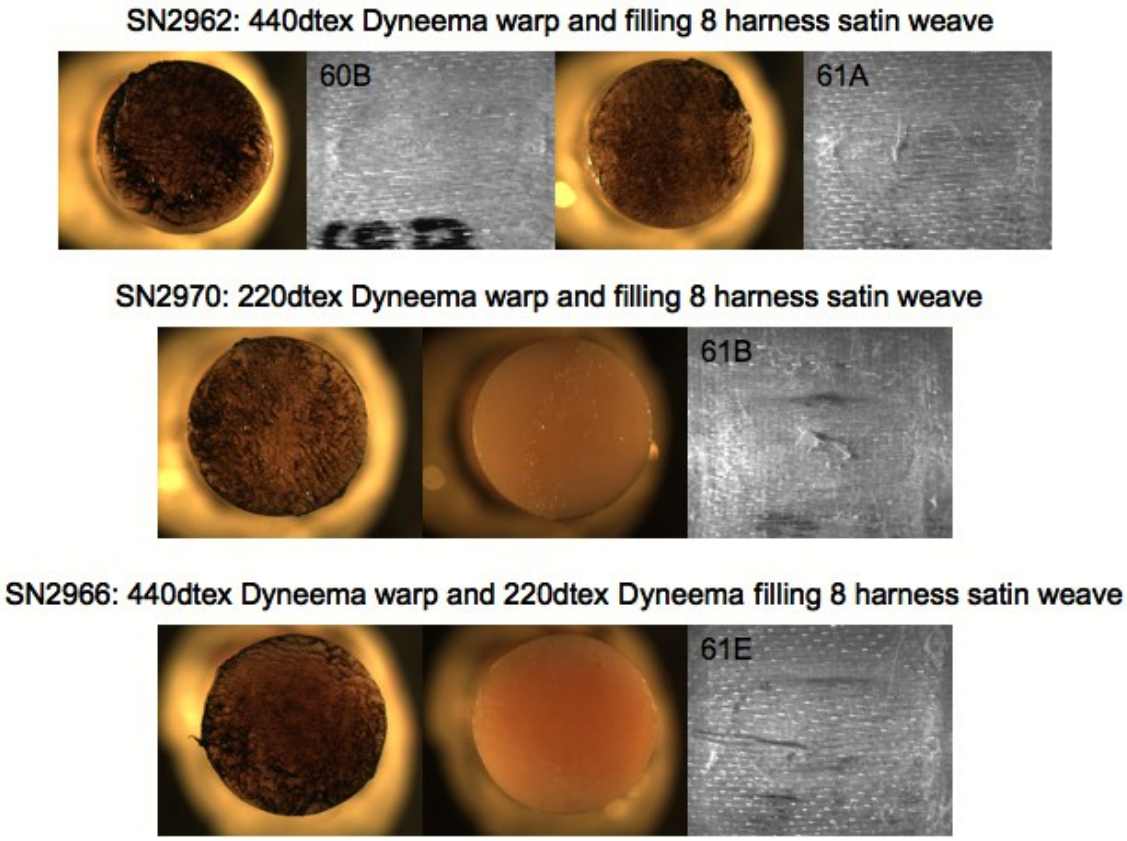

Figure 75: Cartilage specimens after wear tests on PE 8 harness satin weaves. Specimens 61B and 61E wore down to the bone, which can be seen clearly by the pink in the unstained images.

The 5 harness satin weaves suffered less damage than the plain weaves and 8 harness satins (Figure 76). The cartilage appears less worn from the SN2965 material than the SN2969 material, but both wear less than the 8 harness satins and plain weaves.

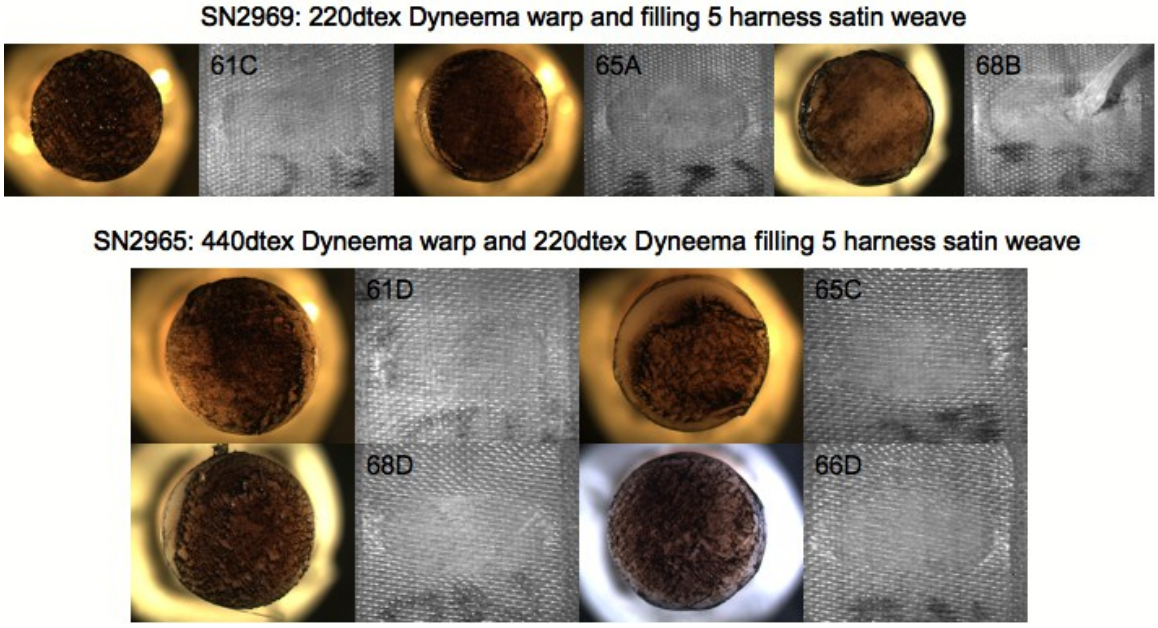

Figure 76: Cartilage specimens after wear tests on PE 5 harness satin weaves. The only damage that can be seen is the group of threads in 68B that came loose, and the flattening, or compression of the material where it was worn.

Like the 5 harness satins, the twills were not damaged as much as the plain weaves and 8 harness satins (Figure 77). None of the SN2964 wovens suffered significant damage, but the cartilage specimens were significantly worn. The specimens worn on SN2968 all wore down to the bone, but the only one of those wovens damaged was 63E.

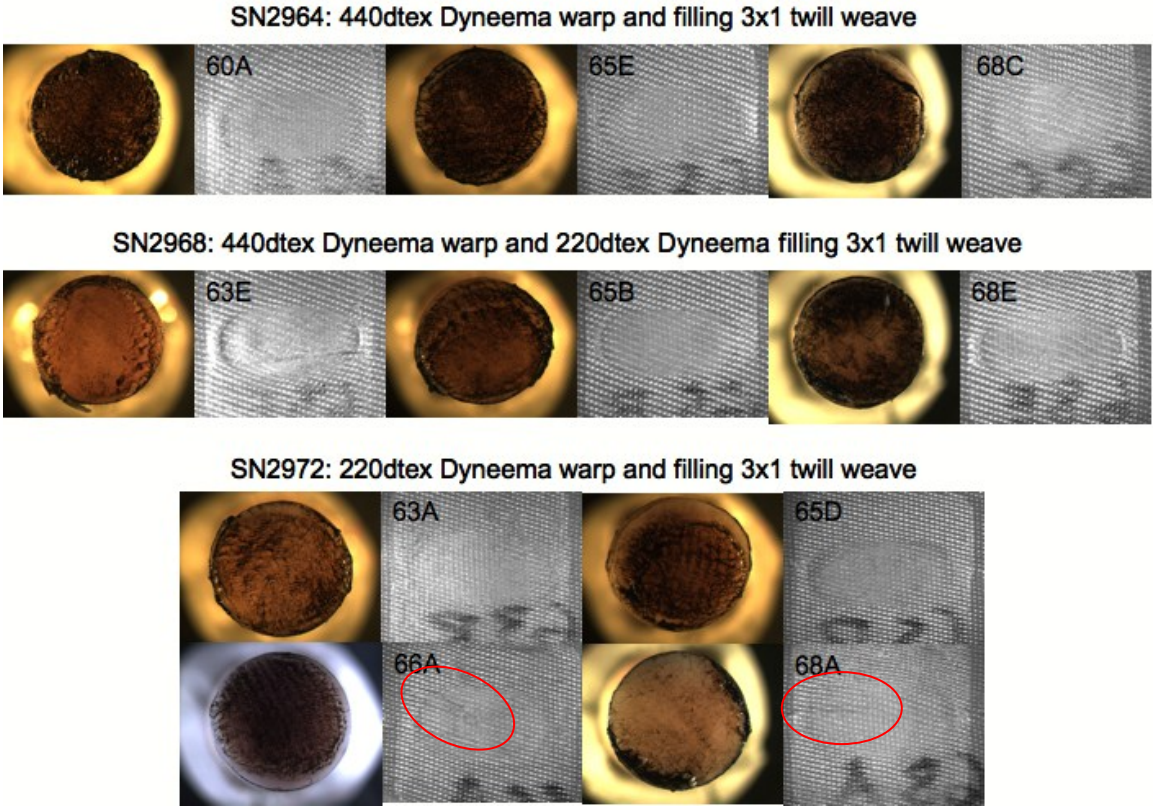

Figure 77: Cartilage specimens after wear tests on PE twill weaves. Two of the SN2972 wovens each had a single small thread come loose, circled in red. The loose thread in 68A appeared to cause significant damage, and the specimen is worn to the bone, but the other three specimens worn on this material have less severe wear.

Many of the PE woven materials were damaged during testing. The wear of the cartilage specimens was more severe when the wovens were damaged. Again, the wear from the pucks is significantly less than the wear from the wovens (Figure 78). There is no noticeable difference between the wear from the PET pucks and the wear from the PE pucks.

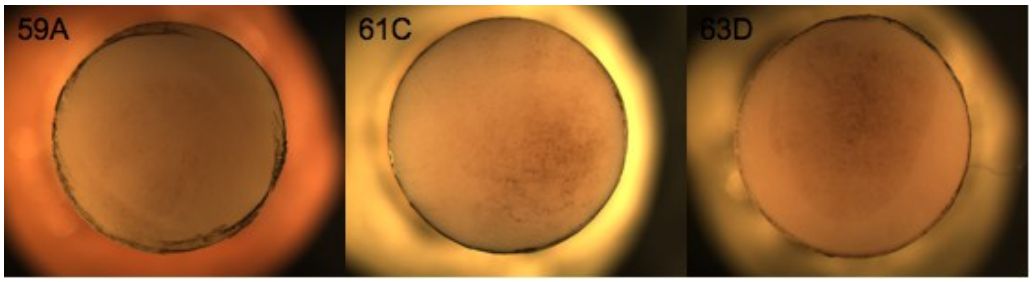

Figure 78: Cartilage specimens after wear tests on PE pucks

Chemical Analysis

To quantitatively determine cartilage wear, the amount of collagen in the hydrating solution was determined using HPLC. The analysis was performed for two samples each of different 5 harness satin and twill PE wovens, and the PET 5/5 satin woven (clamped with the strap). Three samples each were analyzed for the PE and PET pucks. While HPLC could not be used for all samples due to time, the PE wovens that appeared to perform the best were chosen for chemical analysis, and one PET woven was chosen to compare to the pucks. The HPLC results were analyzed to give the dry mass of cartilage removed during testing. Each PET sample was run through the HPLC three times, and the PE samples were each run two times. The samples tested were the PETs labeled 57A-E, and the PEs labeled 59-65. The results, with standard deviations, are shown in Figure 79, where each bar represents one sample. As expected, the pucks showed less wear than the wovens. According to the chemical analysis, the fabrics ranked from best (least wear) to worst (most wear) as:

1. SN3407: PET 5/5 twill (clamped with strap)
2. SN2969: PE 220 dtex 5 harness satin
3. SN2965: PE 440 dtex warp, 220 dtex filling 5 harness satin
4. SN2972: PE 220 dtex twill
5. SN2964: PE 440 dtex twill
6. SN2968: PE 440 dtex warp, 220 dtex filling twill

These results are consistent with the visual wear of the samples that was observed. Some of the PE woven samples have high standard deviations, which showed that the HPLC could be inconsistent. There were also inconsistencies between samples worn on the same material.

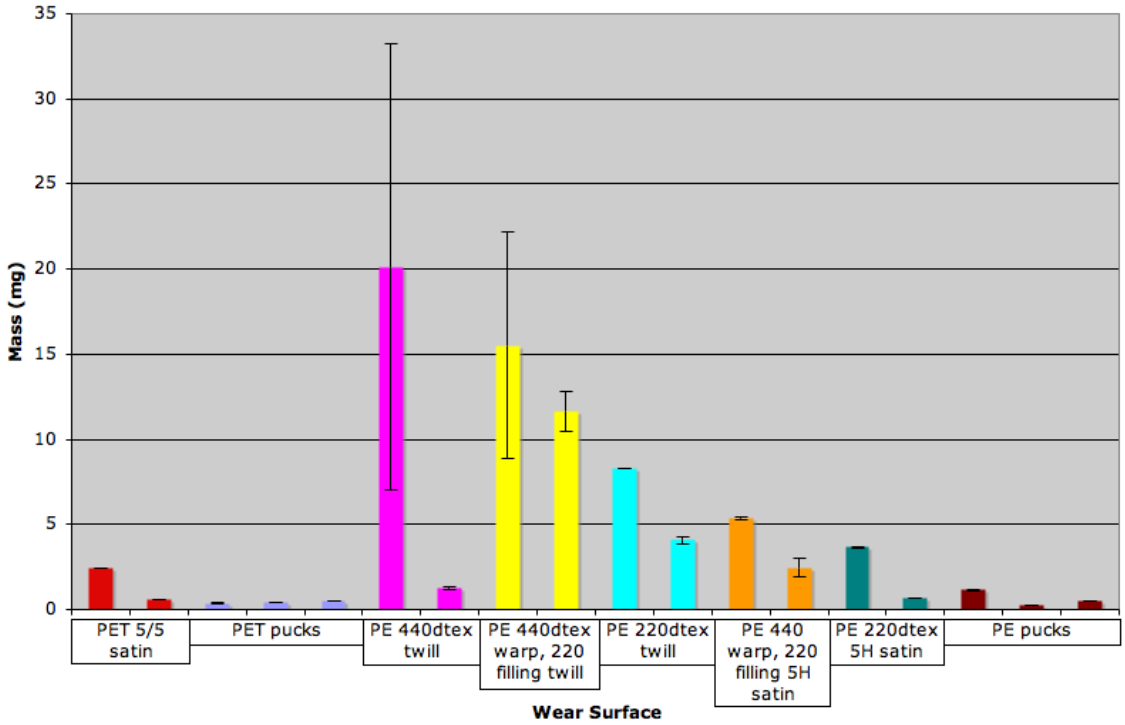

Figure 79: HPLC Results: Mass removed from cartilage. Each bar represents one cartilage sample.

The surface roughness (Ra) of each specimen was measured before and after testing. The samples worn on the pucks, with the lowest mass removed, all showed a relatively low change in surface roughness (Figure 80). For the samples with great mass removed showed greater surface roughness, but these samples ranged from about 1 to over 4 µm. The change in Ra seems to be a good way to distinguish between light wear and severe wear, but it does not accurately detect small differences in wear.

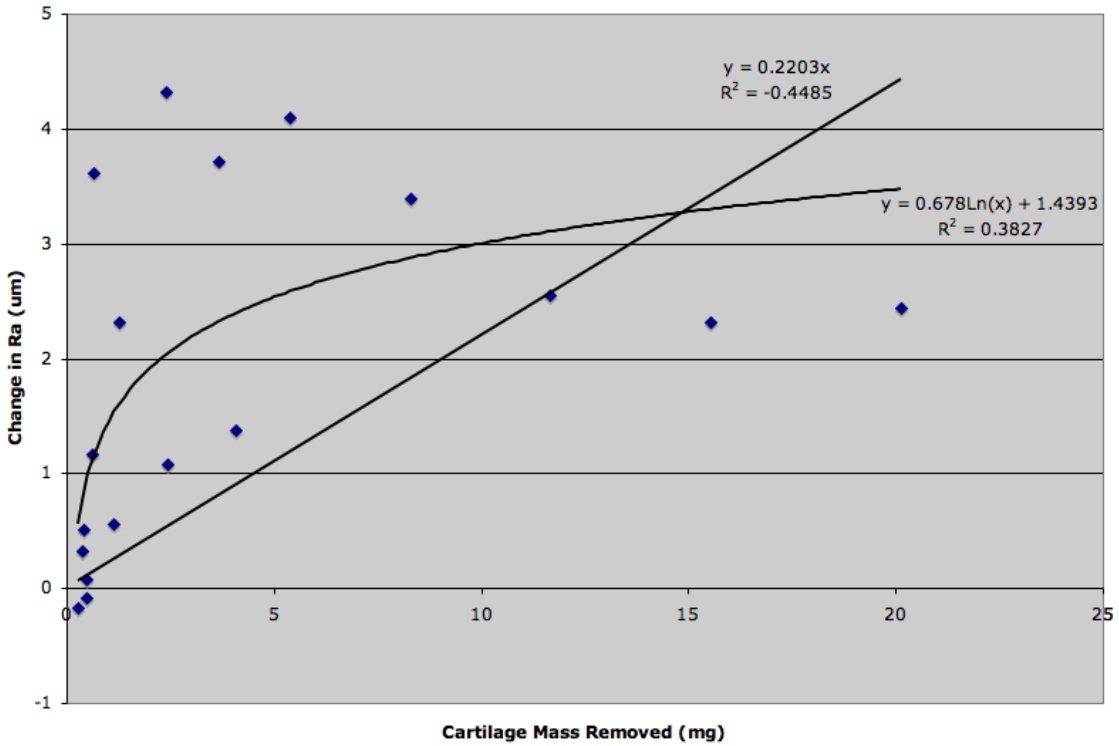

Figure 80: Change in surface roughness compared to cartilage mass removed. The best-fit linear and logarithmic curves with R^2 values of -0.4485 and 0.3827, respectfully, show that there is not a consistent trend relating the change in Ra the amount of cartilage worn off.

Discussion

Clamping

When the woven materials were clamped with the strap, the cartilage specimens experienced less wear than when the materials were clamped without the strap. The strap was meant to imitate the compliance of the 3-D wovens, and the results suggest that the compliance does help to reduce the wear. However, the contact pressure was reduced with the strap, which may have contributed to the decreased wear. Additionally, the PET woven materials were damaged when clamped with the strap, and may have eventually failed. Also, there was little difference in wear between materials clamped with the strap, but when clamped without the strap, there were differences in wear. Clamping with no strap seems to be a better way to compare cartilage wear on different woven materials.

PET vs. PE Wovens

The PE wovens had been expected to cause less wear than the PET wovens because they felt smoother to the touch, but this was not the case. However, it is difficult to make comparisons between the two materials because the clamping methods and the weaves were quite different. Also, the PE wovens were thicker. When clamped without the strap, the PET wovens had no noticeable damage, but each type a PE woven had at least one sample get damaged. This may be due to the material (polyester or polyethylene), or it may be due to the characteristics of the weave such as the size of the threads or the tightness of the weave.

PET Wovens

The PET wovens were difficult to compare visually when clamped with the strap, and samples from only one fabric were chemically analyzed. The woven materials were damaged when clamped with the strap, but they were not damaged when clamped without the strap. Based on visual observation in the one test in which PET wovens were clamped without the strap, the materials ranked best to worst as:

1. SN3500: Satin Stripes
2. SN3499: Satin Checks
3. SN3496: 4/4 Twill

PE Wovens

- The 5 harness satins (SN2969 and SN2965), and the 220 dtex twill (SN2972) worked the best.
- The 440 dtex twill (SN 2964) caused slightly more wear. The 440 warp 220 filling twill (SN2968) wore the cartilage down to the bone each time.
- The 8 harness satins were all damaged with broken threads and caused severe wear. SN2962 was better than the other weaves in this group.
- The plain weaves were all damaged with the weave separating and caused the most severe wear to the cartilage.

The PE woven materials were damaged in three ways (each way caused severe cartilage wear):

- Threads broke in the center (mainly 8 harness satins)
- Threads were pulled out of their weave (all types of weaves)
- The weave would spread apart and threads separate (plain weaves)

Overall Ranking of Woven Materials

Based on a both visual observation and chemical analysis

1. All PET wovens clamped with strap
2. PET satin stripes (without strap)
3. SN2969: PE 220 dtex 5 harness satin
4. SN2965: PE 440 dtex warp, 220 dtex filling 5 harness satin
5. SN2972: PE 220 dtex twill
6. PET satin checks (without strap)
7. SN2964: PE 440 dtex twill
8. SN2962: PE 440 dtex 8 harness satin
9. SN2968: PE 440 dtex warp, 220 dtex filling twill
10. SN2970, SN2966: PE 220 dtex and 440 warp, 220 filling 8 harness satins
11. SN: PET 4/4 twill (without strap)
12. SN2963, SN2967, SN2971: PE plain weaves

Conclusions

None of the tested woven materials can be strongly recommended for use as the articulating surface of an implant in their current configuration as 2-D weaves, though results may be different when they are the surface layer of a 3-D woven material. After wearing for only four hours, each of the woven materials caused significant cartilage wear. The cartilage wear from the woven materials was consistently more severe than the wear from flat solid pucks made from the same materials. There was no noticeable difference in the wear from the different pucks. The woven materials felt smoother in one direction (with the grain) than at a diagonal or perpendicular to the grain. In each test, the direction of wear was aligned with the grain of the woven material, so the tests were a best-case scenario. In reality, a knee joint does not move perfectly in a straight line, so a cartilage replacement would need to be able to articulate well in multiple directions. There were also problems with the woven materials themselves being damaged, which probably caused further cartilage damage.

Assess Cartilage Damage and Wear (Other): Collagen Crosslinking for Improved Cartilage Wear

With collagen being the major structural protein in the body, there is considerable interest in the relationship between the mechanical properties and structure of collagen in the cartilage matrix. However, collagen remains poorly understood due to the difficulty in studying the protein. One reason for this difficulty is the great variability in the structure of collagen molecules that occurs for two main reasons: continuous modification and a long half-life [Wilson et al., 2005]. These modifications include collagen cleavage and both enzymatic and non-enzymatic crosslinking [Eyre, Paz and Gallop 1984]. The network of type II collagen fibrils provides the tensile strength and is essential for maintaining the volume and shape of the cartilage. The tensile strength is increased by covalent, intramolecular crosslinks which form between type II collagen molecules [Kuettner 1992]. In articular cartilage, the major collagen crosslinks include the difunctional crosslink, dehydrodihydroxylysinonorleucine, and the trifunctional crosslink, hydroxylysyl pyridinoline (HP) [Fung and Chien, 2001].

Variations in collagen crosslink density have been correlated with the biomechanical properties of cartilage. It is reported that crosslinking in cartilage increases the stiffness of the collagen network [Chen et al., 2002; DeGroot et al., 1999; DeGroot et al., 2004; Verzijl et al., 2002). For example, the tensile strength and modulus are positively correlated with pyridinoline crosslink density [Williamson et al., 2003] and *in vivo*, more severe OA correlates to higher lysyl hydroxylation and pyridinoline crosslink levels [Bank et al., 2002]. One study on the effect of non-enzymatic (NEM) products on cartilage stiffness found that NEMs resulted in a stiffening of the cartilage network based on a decrease instantaneous deformation (ID), of approximately 25% [Bank et al., 1998]. In another study on full-depth OA cartilage, a close relationship was found between swelling and ID, which reflects the tensile stiffness of the collagen network [Bank et al., 2000]. The study found that swelling and ID correlated strongly with the amount of degraded collagen molecules, however no relationship was found between collagen crosslinking and swelling of the surface, middle, and deep zones [Bank et al., 2000].

The equilibrium modulus of cartilage, as measured by confined compression tests, has also been shown to decrease with age and degeneration [Armstrong and Mow, 1982]. Degeneration was based on two semi-quantitative indices of structural integrity: disorganization in histological sections and the macroscopically observable description of the specimen surface

[Armstrong and Mow, 1982]. This association, though statistically significant, is believed to explain only a small fraction of the total variation in mechanical properties with age. For that reason, examining the relationship between the mechanical properties and biochemical composition as we age should be explored. On such study found that increasing cartilage advanced glycation end-product (AGE) crosslinking *in vitro* through incubation in threose increased the stiffness of the collagen network. It has been proposed that this increased stiffness by AGE crosslinking may play a part in the reduced ability of the collagen network to resist damage as we age, however, this only looks at changes in stiffness and does not take into account the biological response AGEs are known to induce in chondrocytes. Thus, even with an increase in stiffness, the age-related accumulation of AGE crosslinks could be a means by which age is a predisposing factor for the onset of OA [Verzijl et al., 2002]. An increase in AGE crosslinks, which naturally occur in the tissue, is correlated to an increase in the dynamic modulus of 59% [Chen et al. 2002]. Additionally, inducing glycation with ribose has resulted in a 25% increase in the modulus [Bank et al., 1998]. Averaging these two values, one might expect a 42% increase in the modulus. In using the photochemical croslinking treatment proposed for this study, 3.5 fold increases in elastic modulus have been seen in collagen gels [Mozia et al., 2011]. In corneas, riboflavin treatment has resulted in increases in Young's modulus by a factor 1.8 in porcine corneas and 4.5 in human corneas [Wollensak, Spoerl and Seiler 2003]. While photochemically crosslinking collagen has produced greater increases in the elastic modulus in other parts of the body and in collagen gels, it has not yet been done on articular cartilage.

Despite the known correlations between crosslink density and the biochemical behavior of of cartilage, it is not known if an increase in crosslink density affects cartilage's resistance to damage and wear due to repeated sliding contact. There is, however, evidence that increased crosslink density results in less wear of hydrogels used as synthetic articular cartilage without altering the frictional coefficient [Freeman et al., 2000]. There is also a positive correlation between crosslink density and the tensile strength and modulus, which may reduce the susceptibility of the collagen network to damage. With composite materials, wear has been shown to decrease with increasing shear modulus [Chang, 1983]. Cartilage can be thought of as a composite material in the sense that it has several components and its structure varies with depth. Additionally, in polymers, crosslinking (as in ultra high molecular weight polyethylene) results in improved wear resistance [Chiesa et al., 2000; Galvin et al., 2006]. Considering the inverse relationship between wear and stiffness as well as the increase in modulus associated with crosslinking, it is reasonable to believe that crosslinking cartilage may increase wear resistance. Based on the above reasons and preliminary findings on crosslinked cartilage, my hypothesis is that increased collagen crosslinking in cartilage results in decreased cartilage wear.

We believe that as we improve our understanding of crosslinking in cartilage and how it relates to wear, we can develop therapies for the treatment of OA. To investigate the relationship between cartilage crosslinks and wear, we have investigated multiple crosslinking agents and how they affect the stiffness of the tissue. Preliminary studies in our lab found that fixation using a ribose treatment resulted in decrease wear after 24hr of continuous testing (Figure 81). For this experiment bovine osteochondral plugs were incubated in a 0.6M Ribose solution for 72hrs at 37C. Specimens were tested in a pin-on-disc wear tester for 24 hrs at room temperature, for a total distance traveled of 192m.

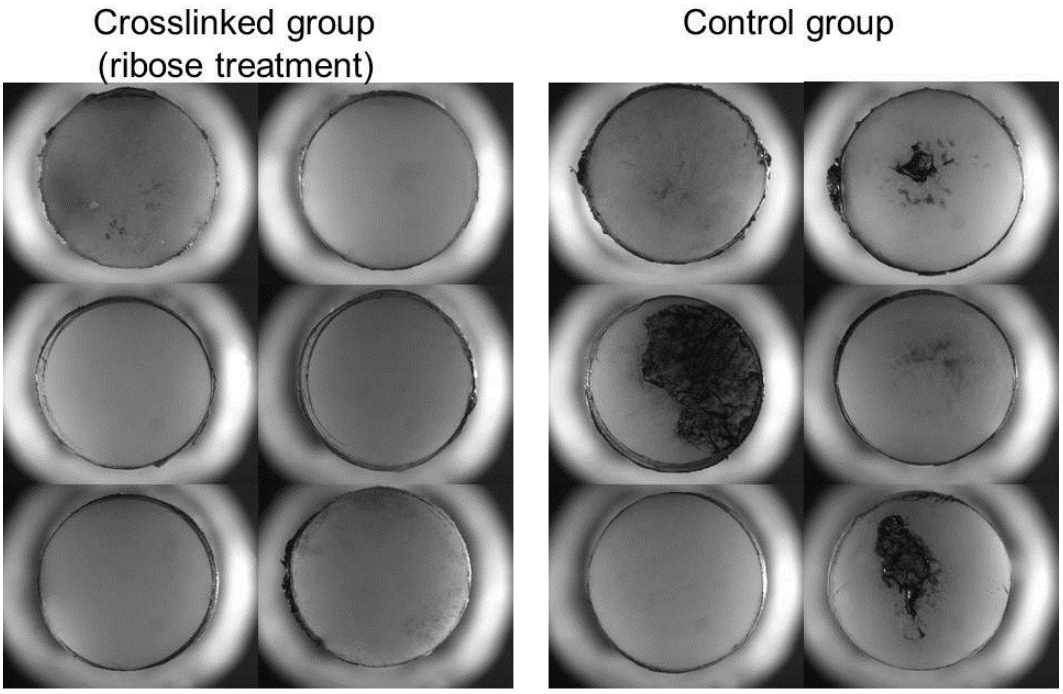

Figure 81: Comparison of visible surface damage between control and crosslinked groups.

However, ribose is not an ideal crosslinking agent due to the negative effect it has on cells within the tissue. In addition to ribose, several crosslinking agents have been used in the chemical modification of tissue. Some of these include formaldehyde [Nimni et al, 1987], glutaraldehyde [Nimni et al., 1987] and epoxy compound [Noishiki et al., 1989]. Like ribose these agents have undesirable effects on the cells, with some being highly cytotoxic [Sung et al., 1999]. In order to use a crosslinking agent *in vivo* it is necessary to find a crosslinking agent that has low cytoxicity and produces stable, biocompatible crosslink products. To achieve this goal, we are investigating the effect that modifying bovine articular cartilage with a naturally occurring crosslinking agent- genipin- has on wear rates of the tissue.

In our preliminary stages, we have investigated the effect of incubation for 0-2 hrs in genipin solutions of 0-2.5mM has on the stiffness of the tissue. As mentioned previously, stiffness increases with increasing crosslink density [Verzijl et al., 2002; Chen et al., 2002; DeGroot, 2004; DeGroot et al., 1999; Bank et al.,1998; Bank et al., 2000; Williamson et al., 2003), so an increase in stiffness after incubation in genipin was used to verify that the tissue had been crosslinked. After only a 5 minute incubation period in a relatively low concentration of genipin (0.1mM) the modulus was 20-70% higher than the control for six donors (Figure 82).

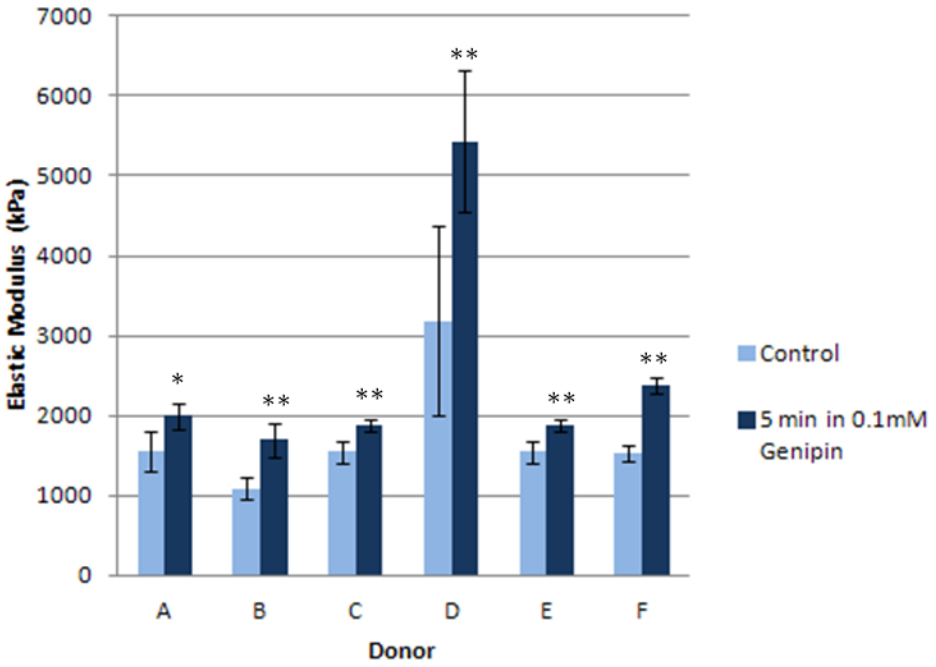

Figure 82: Change in elastic modulus between control and cartilage treated for 5 minutes in a 0.1mM genipin solution. *: $p<0.01$, **: $p<0.001$.

Future steps for this research include wear testing to compare the wear rates of untreated and crosslinked cartilage. Based on previous studies and the observed increase in stiffness with crosslinking in genipin, we expect cartilage crosslinked in genipin to have lower wear rates than the control.

Assess Cartilage Damage and Wear: Testing Involving Joint Simulators and Cartilage

Because the results of the pin-on-disc testing of cartilage against the woven materials were poor, we did not move ahead with this task.

KEY RESEARCH ACCOMPLISHMENTS

- Direct observation of wear and wear modes for fibers suitable for weaving. Wear tests have taken place at a number of length scales, including microsliding in an atomic force microscope to simulate wear that could occur during normal loading and unloading of a three-dimensional weave.
- Development of an experimental rig to simulate fiber wear at relevant length scales. This rig is especially valuable for screening materials for the structural portion of the woven materials.
- Feasibility of laser welding fibers in the woven materials has been demonstrated.
- Increased mechanical properties in confined compression and improved wear resistance of polymer woven materials with laser welding have been shown.
- Protocols for fabricating cartilage specimens, testing them against woven materials and quantifying cartilage wear were established.
- Wear testing of cartilage against a number of woven fabrics was conducted, and the woven fabrics were ranked according to their friendliness to cartilage.
- Collagen crosslinking was identified as a method to improve cartilage wear and will be studied further in the future.

REPORTABLE OUTCOMES

Manuscripts

Giordano, M., and Schmid, S.R., ``Accelerated Life Testing of Polymer Fibers for Use in Woven Cartilage Replacement," submitted to *STLE Transactions*.

McGann, M.E., Vahdati, A., and Wagner, D.R., “Methods to Assess In Vitro Wear of Articular Cartilage”, in press at *Proceedings of the Institution of Mechanical Engineers, Part H: Journal of Engineering in Medicine.*

Giordano, M., and Schmid, S.R., ``Evaluation of Individual Fiber Wear Resistance Using Accelerated Life Testing," *Tribology Transactions*, v. 55, 2012, pp. 140-148. Also honored as Editor's choice in *Tribology and Lubrication Technology*, v. 68, 2012, pp. 44-53.

Conference Presentations

McGann M.E. and Wagner D.R. Fabrication of Cartilage-Bone Specimens for Cartilage Wear Testing. Summer Bioengineering Conference, Lake Tahoe, CA 2009

Rodts, T., Schmid, S.R., Selles-Canto, M.S., ``Selective Welding Reinforcement Within Three-Dimensional Fabrics" accepted for the 40th North American Manufacturing Research Conference, University of Notre Dame, June 4-8, 2012

Giordano, M., and Schmid, S.R., ``Evaluation of Fiber Wear Resistance in an Atomic Force Microscope for Use in Cartilage Replacements," presented at the STLE Annual Meeting, Atlanta, GA, May 16, 2011.

Giordano, M., and Schmid, S.R., ``Evaluation of individual fiber wear resistance using accelerated life testing," presented at the STLE Annual Meeting, Atlanta, GA, May 17, 2011.

Giordano, M., and Schmid, S.R., ``AFM Investigation of Powder Surface Forces," Presented at PowderMET 2011, San Francisco, CA, May 20, 2011.

Giordano, M., Schmid, S.R., Parrott, R., and Lozier, A., ``Investigation of Fiber Wear in a Woven Composite Using Atomic Force Microscopy," presented at the 2010 Summer Bioengineering Conference, June 15-19, Naples, FL.

Rodts, T.W., Schmid, S.R., Parrott, R., and Lozier, A., ``Compression Testing of 3D Polymer Fabrics for Use as Cartilage Scaffolds," presented at the 2010 Summer Bioengineering Conference, June 15-19, Naples, FL.

McGann, M.E. and Wagner, D.R., "Preparation and Wear Evaluation of Cartilage in Pin-On-Disc Testing" presented at the Annual Meeting of the Orthopaedic Research Society, Long Beach, CA, 2011.

Intellectual Property
A patent is pending: Schmid, S.R., ``Woven Materials for Orthopedic Implants,", Submitted May 2006.

A provisional patent has been submitted: Wagner D.R.: "Collagen Crosslinking to Reduce Cartilage Wear".

Degrees
Kyle Jones, PhD (2010)
Michael Giordano, PhD (2011)
Timothy Rodts (PhD expected May 2012)
Megan McGann (PhD expected 2012)

Grant Proposals Submitted
Collagen Crosslinking for the Prevention of Post-traumatic Osteoarthritis (PENDING)
PI: D. Wagner; co-PI: S. Trippel at IUSM; collaborator: T. Ovaert

Source: US Army Peer Reviewed Orthopaedic Research Program (Translational Research Partnership Award)
Submitted Dec 2011

Genipin Crosslinking to Prevent Post-traumatic Osteoarthritis (PENDING)
PI: D. Wagner; co-PI: S. Trippel at IUSM; collaborator: T. Ovaert

Source: US Army Peer Reviewed Orthopaedic Research Program (Translational Research Partnership Award)
Submitted Feb 2012

Collagen Crosslinking as a Protective Measure Against Cartilage Wear (NOT FUNDED)
PI: D. Wagner; co-investigator: T. Ovaert co-investigator

Dates: 4/1/2012 – 3/31/2015
Source: NIH (R03)

Employment Opportunities
Kyle Jones was hired by BioMet
Mike Giordano was hired by Zimmer

CONCLUSIONS

Three-dimensional polymer weaves were investigated as a cartilage replacement material, perhaps for spot replacements of painful localized defects. One notable achievement is the development of a technique to laser weld the polymer fibers together within the woven material. The mechanical evaluation of the woven-welded materials shows that they have dramatically improved wear resistance and that their mechanical properties are more similar to cartilage than their unwelded counterparts. These results may have important applications in fields other than orthopaedics. Unfortunately, wear testing of cartilage against the woven materials did not give promising results, and future designs should include a smooth surface to interface with the cartilage. In response to these results, we began experiments with short-duration, non-toxic crosslinking protocols that are expected to improve the wear resistance of cartilage. If further studies are successful, they may lead to techniques that reduce cartilage wear against engineering materials, increasing the life of implants such as the one proposed here.

REFERENCES

Alves, N.M., J.F. Mano, E. Balaguer, J.M. Meseguer Deuñas and J.L. Gómez Ribelles. “Glass transition and structural relaxation in semi-crystalline poly(ethylene terephthalate): a DSC study.” Polymer. 43 (2002): 4111-4122.

Archard, J., 1953, Journal of Applied Physics, *v.* 24, p. 981.

Armstrong, C. G., and V. C. Mow. "Variations in the Intrinsic Mechanical Properties of Human Articular Cartilage with Age, Degeneration, and Water Content." The Journal of Bone and Joint Surgery 64.1 (1982): 88.

ASTM F 2025-06, 2009*, Standard Practice for Gravimetric Measurement of Polymeric Components for Wear Assessment.* ASTM International: West Conshohocken, PA.

Athanasiou, K.A., J.A. Buckwalter, T.I. Malinin and V.C. Mow, 1991, “Interspecies comparisons of in situ intrinsic mechanical properties of disal femoral cartilage” Journal of Orthopaedic Research. V. 9, pp. 330-340.

Ayyappa, E., 1997, Journal of Prosthetics and Orthotics, *v.* 9, p. 10.

Bank, R. A., et al. "Ageing and Zonal Variation in Post-Translational Modification of Collagen in Normal Human Articular Cartilage. the Age-Related Increase in Non-Enzymatic Glycation Affects Biomechanical Properties of Cartilage." Biochemical Journal 330.Pt 1 (1998): 345-351.

Bank, R. A., et al. "Putative Role of Lysyl Hydroxylation and Pyridinoline Cross-Linking during Adolescence in the Occurrence of Osteoarthritis at Old Age." Osteoarthritis and Cartilage 10.2 (2002): 127-34.

Bank, Ruud A., et al. "The Increased Swelling and Instantaneous Deformation of Osteoarthritic Cartilage is Highly Correlated with Collagen Degradation." Arthritis & Rheumatism 43.10 (2000): 2202-10.

Becker, F. and H. Potente. “A Step Towards Understanding the Heating Phase of Laser Transmission Welding in Polymers” Polymer Engineering and Science. 42 (2002): 365-374.

Bell, CJ, Ingrahm, E and Fisher, J. Influence of hylauronic acid on the time-dependent friction response of articular cartilage under different conditions. Proc Inst Mech Eng [H]. 2006, 220, pp. 23-31.

Chang, H. W. "Wear Characteristics of Composites: Effect of Fiber Orientation." Wear 85.1 (1983): 81-91.

Chen, Albert C., et al. "Induction of Advanced Glycation End Products and Alterations of the Tensile Properties of Articular Cartilage." Arthritis & Rheumatism 46.12 (2002): 3212-7.

Chiesa, R., et al. "Enhanced Wear Performance of Highly Crosslinked UHMWPE for Artificial Joints." Journal of Biomedical Materials Research Part A 50.3 (2000): 381-7.

Cottrell, JM, et al. A new technique to measure the dynamic contact pressures on the tibial plateau. J Biomechanics. 2008, 41, pp. 2324-29.

Covert, R., Ott, R., and Ku, D., 2003, Wear, v. 255, pp. 1064–1068.

DeGroot, J. "The AGE of the Matrix: Chemistry, Consequence and Cure." Current Opinion in Pharmacology 4.3 (2004): 301-5.

DeGroot, Jeroen, et al. "Age-Related Decrease in Proteoglycan Synthesis of Human Articular Chondrocytes: The Role of Nonenzymatic Glycation." Arthritis & Rheumatism 42.5 (1999a): 1003-9.

DeGroot, Jeroen, et al. "Accumulation of Advanced Glycation End Products Decreases Collagen Turnover by Bovine Chondrocytes." Experimental Cell Research 266.2 (2001): 303-10.

Duan, Y., M. Keefe, T. A. Bogetti, and B. A. Cheeseman. “Modeling the role of friction during ballistic impact of a high-strength plain-weave fabric.” Composite Structures 68 (2005): 331-37.

Eyre, D. R., M. A. Paz, and P. M. Gallop. "Cross-Linking in Collagen and Elastin." Annual Review of Biochemistry 53.1 (1984): 717-48.

Forester, H and Fisher, J. The influence of continuous sliding and subsequent surface wear on the friction of articular cartilage. Proc Inst Mech Eng [H]. 1996, 210, pp. 329-345.

Freeman, M. E., et al. "Friction, Wear, and Lubrication of Hydrogels as Synthetic Articular Cartilage." Wear 241.2 (2000): 129-35.

Fujibayashi, S., Neo, M., Kim, H., Kokubo, T., and Nakamura, T. Biomaterials 25, 443–450 (2004).

Fukubayashi, T. and Kurosawa, 1980, H. Acta Orthopaedica Scandinavica, v. 51, pp. 871– 879.

Fung, Y., and S. Chien. Introduction to Bioengineering. World Scientific, 2001.

Galvin, A., et al. "Wear of Crosslinked Polyethylene Under Different Tribological Conditions." Journal of Materials Science: Materials in Medicine 17.3 (2006): 235-43.

Giordano, M.A. *Screening Methods For Woven Materials As Artificial Cartilage.* Ph.D. Dissertation. University of Notre Dame, 2011.

Giordano, M., and Schmid, S.R., 2012, "Evaluation of Individual Fiber Wear Resistance Using Accelerated Life Testing," Tribology Transactions, v. 55, pp. 140-148. Also honored as Editor's choice in Tribology and Lubrication Technology, v. 68, 2012, pp. 44-53.

Hayes, W. C., and A. J. Bodine. "Flow-Independent Viscoelastic Properties of Articular Cartilage Matrix." Journal of Biomechanics 11.8-9 (1978): 407-19.

Howell, S., Jowell, S., and Hull, M., 2010, Journal of Bone & Joint Surgery, v. 92, pp. 98–104.

Hutson, PR, Crawford, ME and Sorkness, RL. L iquid chromatographic determination of hydroxyproline in tissue samples. *Journal of Chromotography B.* 2003, Vol. 791, pp. 427-430.

Jones, K. 2010, *Percolation Mechanism in Orthopedic Implants*. PhD thesis, University of NotreDame.

Kagan, V.A., et al., 2002, Laser Transmission Welding of Semi-crystalline Thermoplastics-Part I: Optical Characterization of Nylon Based Plastics. Journal of Reinforced Plastics and Composites, 21:1101-1122.

Kuettner, K. E. "Biochemistry of Articular Cartilage in Health and Disease." Clinical biochemistry 25.3 (1992): 155-63.

Lipshitz, H, Etheredge, R and Glimcher, M. In Vitro Wear of Articular Cartilage. I. Hydroxyproline, Hexosamine, and Amino Acid composition of bovine articular cartilage. J Bone Joint Surg Am. 1975, Vol. 57, pp. 527-534.

Litwin, W., 2011, Tribology Transactions, v. 54, pp. 351–361.

Malek, I., Moorehead, J., Abiddin, Z., and Montgomery, 2009, S. Clinical Anatomy, v. 22, pp. 517–522.

McEwen, H.M.J., P.I. Barnett, C.J. Bell, R. Farrar, D.D. Auger, M.H. Stone and J. Fisher. "The influence of design, materials and kinematics on the in vitro wear of total knee replacements." Journal of Biomechanics. 38 (2005): 357-365.

McGann, M and Wagner, DR. *Fabrication of cartilage-bone specimens for cartilage wear testing.* Lake Tahoe : Proc of ASME SBC, 2009.

McHargue, C. J., 1997, "Surface Mechanical Properties Using Nanoindentation." In: Bhushan, B., ed., Micro/Nanotribology and its Applications. pp. 467-492.

Merkher, Y., et al. "A Rational Human Joint Friction Test using a Human Cartilage-on-Cartilage Arrangement." Tribology Letters 22.1 (2006): 29-36.

Meyer, E., 1908, "Untersuchungen über Härteprüfungen und Härte". Zeitschrift des Vereines Deutscher Ingenieure 52, pp. 82-85.

Mow, V.C. and X.E. Guo, 2002, "Mechano-Electrochemical Properties of Articular Cartilage: Their Inhomogeneities and Anisotropies" Annual Review of Biomedical Engineering. v. 4, pp. 175-209.

Mow, V.C., M.H. Holmes and W.M. Lai. "Fluid Transport and Mechanical Properties of Articular Cartilage." Journal of Biomechanics. 17 (1984): 377-394.

Mow, V.C., S.C. Kuei, W.M. Lai, and C.G. Armstrong. "Biphasic Creep and Stress Relaxation of Articular Cartilage in Compression: Theory and Experiments." Journal of Biomechanical Engineering. 102 (1980): 73-82.

Mozia, R. I., et al. "Riboflavin Crosslinking of Composite Tissue Engineered Intervertebral Discs." Orthopedic Research Society. Long Beach, CA, January 13-16, 2011.

Muratoglu, O.K., C.R. Bragdon, M. Jasty, D.O. O'Connor, R.S. Von Knoch and W.H. Harris. "Knee-Simulator Testing of Conventional and Cross-Linked Polyethylene Tibial Inserts." The Journal of Arthroplasty. 19 (2004): 887-897.

Muratoglu, O.K., H.E. Rubash, C.R. Bragdon, B.R. Burroughs, A. Huang and W.H. Harris. "Simulated Normal Gait Wear Testing of a Highly Cross-Linked Polyethylene Tibial Insert." The Journal of Arthroplasty. 22 (2007): 435-444.

Nimni, M. E., et al. "Chemically Modified Collagen: A Natural Biomaterial for Tissue Replacement." Journal of Biomedical Materials Research 21.6 (1987): 741-71.

Noishiki, Y., et al. Method of preparing antithrombogenic medical materials (1989).

Pedersen, D., Brown, T., and Brand, R. Journal of Biomechanics 24(12), 1131–1142 (1991).

Radin, Eric L., et al. "Response of Joints to Impact Loading — III: Relationship between Trabecular Microfractures and Cartilage Degeneration." Journal of Biomechanics 6.1 (1973): 51,54, IN9-IN11, 55-57.

Rodriguez, F., C. Cohen, C.K. Ober and L.A. Archer. Principles of Polymer Systems: Fifth Edition. New York: Taylor & Francis Group. 2003.

Setton, L.A., W. Zhu, V.C. Mow, 1993, "The Biphasic Poroviscoelastic Behavior of Articular Cartilage: Role of the Surface Zone in Governing the Compressive Behavior." Journal of Biomechanics. V. 26, pp. 581-592.

Shekhawat, VK, et al. Surface topography of variable articular cartilage measured with scanning white light interferometry. Osteo and Cart. 2009.

Sugar, A., Kurlakose, M., and Walshaw, N. International Journal of Oral Maxillofacial Surgery 21, 140–144 (1992).

Sung, H. W., et al. "In Vitro Evaluation of Cytotoxicity of a Naturally Occurring Cross-Linking Reagent for Biological Tissue Fixation." Journal of Biomaterials Science, Polymer Edition 10.1 (1999): 63-78.

Tsukamoto, R., S. Chen, T. Asano, M. Ogino, H. Shoji, T. Nakamura and I.C. Clarke. "Improved wear performance with crosslinked UHMWPE and zirconia implants in knee simulation." Acta Orthopaedica. 77 (2006): 505-511.

Verberne, G, et al. Techniques for assessment of wear between human cartilage surfac. Wear. 2009, 266.

Verzijl, Nicole, et al. "Crosslinking by Advanced Glycation End Products Increases the Stiffness of the Collagen Network in Human Articular Cartilage: A Possible Mechanism through which Age is a Risk Factor for Osteoarthritis." Arthritis & Rheumatism 46.1 (2002): 114-23.

Wagner, DR, Reiser, KM and Lotz, JC. "Glycation increases human annulus fibrosus stiffness in both experimental measurements and theoretical predictions." J Biomechanics. (2006): 39.

Williamson, A. K., et al. "Tensile Mechanical Properties of Bovine Articular Cartilage: Variations with Growth and Relationships to Collagen Network Components." Journal of Orthopaedic Research 21.5 (2003): 872-80.

Wilson, W., et al. "A Fibril-Reinforced Poroviscoelastic Swelling Model for Articular Cartilage." Journal of Biomechanics 38.6 (2005): 1195-204.

Wollensak, G., E. Spoerl, and T. Seiler. "Stress-Strain Measurements of Human and Porcine Corneas After Riboflavin-Ultraviolet-A-Induced Cross-Linking." Journal of Cataract & Refractive Surgery 29.9 (2003): 1780-5.

APPENDICES

None